


2014

DEVELOPMENT OF AN IONIC LIQUID FERROFLUID ELECTROSPRAY SOURCE AND MODE SHAPE STUDIES OF A FERROFLUID IN A NON-UNIFORM MAGNETIC FIELD

Edmond Joseph Meyer IV
Michigan Technological University


Follow this and additional works at: <https://digitalcommons.mtu.edu/etds>

 Part of the [Aerospace Engineering Commons](#), and the [Electromagnetics and Photonics Commons](#)
Copyright 2014 Edmond Joseph Meyer IV

Recommended Citation

Meyer, Edmond Joseph IV, "DEVELOPMENT OF AN IONIC LIQUID FERROFLUID ELECTROSPRAY SOURCE AND MODE SHAPE STUDIES OF A FERROFLUID IN A NON-UNIFORM MAGNETIC FIELD", Dissertation, Michigan Technological University, 2014.
<https://digitalcommons.mtu.edu/etds/857>

Follow this and additional works at: <https://digitalcommons.mtu.edu/etds>

 Part of the [Aerospace Engineering Commons](#), and the [Electromagnetics and Photonics Commons](#)

DEVELOPMENT OF AN IONIC LIQUID FERROFLUID ELECTROSPRAY SOURCE
AND MODE SHAPE STUDIES OF A FERROFLUID IN A NON-UNIFORM
MAGNETIC FIELD

By

Edmond Joseph Meyer IV

A DISSERTATION

Submitted in partial fulfillment of the requirements for the degree of

DOCTOR OF PHILOSOPHY

In Mechanical Engineering - Engineering Mechanics

MICHIGAN TECHNOLOGICAL UNIVERSITY

2014

© 2014 Edmond Joseph Meyer IV

This dissertation has been approved in partial fulfillment of the requirements for the Degree of DOCTOR OF PHILOSOPHY in Mechanical Engineering - Engineering Mechanics.

Department of Mechanical Engineering - Engineering Mechanics

Dissertation Advisor: *Dr. Lyon B. King*

Committee Member: *Dr. Jeffery S. Allen*

Committee Member: *Dr. Chang K. Choi*

Committee Member: *Dr. Benjamin D. Prince*

Department Chair: *Dr. William W. Predebon*

It is not a simple matter to differentiate unsuccessful from successful experiments...[Most] work that is finally successful is the result of a series of unsuccessful tests in which difficulties are gradually eliminated.

-Robert Goddard

Contents

List of Figures	xiii
List of Tables	xxxi
Acknowledgements	xxxiii
Abstract	xxxvii
1 Introduction	1
1.1 Electro spray Thrusters	1
1.2 Aim and Scope	4
1.3 Structure	5
2 Background and Review of Prior Research	9
2.1 Introduction	9
2.2 Electro spray	10
2.2.1 Obtaining spray from an Electro spray Source	10
2.2.2 Background of Important Electric Propulsion Thruster Parameters	16

2.2.3	Performance of Electrospray Thrusters and Comparable Electric Propulsion Devices	19
2.2.4	Fabrication Techniques of Electrospray Thrusters	22
2.3	Background of Ferrohydrodynamics	24
2.3.1	Ferrofluids	24
2.3.2	Rosensweig Instabilities	26
2.3.3	Rosensweig Instabilities in Uniform and non-Uniform Magnetic Fields	31
2.4	Analysis of fluid Energies	35
2.4.1	Energy balances of Rosensweig Instabilities	36
2.4.2	Energy of a magnetic drop in a magnetic fields	37
2.4.3	Energy of a conductive and/or polar drop in an electric field	40
2.4.4	Energy balance of an ILFF in combined magnetic and electric fields	42
3	Proof-of-Concept Experiments	45
3.1	Introduction	45
3.2	Electrostatic formation of peaks for electrospray	46
3.3	Ionic Liquid Ferrofluids and their Synthesis	48
3.4	Collaboration with University of Sydney and the fabrication of ionic liquid ferrofluids	48

3.5	Proof-of-concept experimental results: Deformation of Rosensweig Instability in an Electric Field	52
4	Electrospray of an ionic liquid ferrofluid utilizing the Rosensweig instability	55
4.1	Introduction	55
4.2	Equipment and Testing Methodologies	56
4.2.1	Electrospray Source	57
4.2.2	Current Measurement	58
4.2.3	Power Supplies	60
4.2.4	Vacuum Facility	61
4.2.5	Camera and Lens	62
4.2.6	Experiments conducted	62
4.3	Experiment 1: Emission study of EAN based ILFF(batch # NJ397007) .	64
4.3.1	Observing emission	64
4.3.2	I-V Curves	66
4.3.3	Other Observations During Experiment 1	69
4.3.3.1	Current collector visibly coated with ILFF	69
4.3.3.2	Self-regeneration of Emitter Sites	70
4.3.3.3	Multi-Site Emission	71
4.3.4	Discussion of the Results from Experiment 1 with EAN-based ILFF (batch # NJ397007)	72

4.4	Experiment 2: Emission Study of EMIM-NTf2-based ILFF (batch # NJ397028)	73
4.4.1	Observing emission	73
4.4.2	I-V Curves	74
4.4.3	Other Observations During Experiment 2	82
4.4.3.1	Multi-Site Emission	82
4.4.3.2	Other ILFF deformations and protrusions	82
4.4.4	Discussion of the Results from Experiment 2 with EMIM-NTf2-based ILFF (batch # NJ397028)	85
4.5	Experiment 3: Onset Voltage Study of EMIM-NTf2-based ILFF (batch # NJ397028))	87
4.5.1	Comparison of measured onset voltage to predicted onset voltage	87
4.5.2	Behavior of onset of ion emission	90
4.5.3	Error Analysis of Measured Tip Radii and Tip-to-Extraction Electrode distances	101
5	Instability wavelengths of a ferrofluid in a non-uniform magnetic field	105
5.1	Introduction	105
5.2	Equipment and Testing Methodologies	107
5.2.1	Ferrofluid	108
5.2.2	Bar magnet	108
5.2.3	Halbach Array	109

5.2.4	Gauss Probe and the Mapping of the Magnetic Field	110
5.2.5	Camera and Lens	112
5.2.6	Rosensweig Instability Wavelength Setup and Measurement	112
5.3	Peak-to-peak Spacing of Rosensweig Instabilities in Non-Uniform Magnetic Field	116
5.3.1	A Body Force Approach to Analysing Peak-to-Peak Spacing of Rosensweig Instabilities in a Non-Uniform Magnetic Field	117
5.3.2	An Energy Approach to Analysing Peak-to-Peak Spacing of Rosensweig Instabilities in a Non-Uniform Magnetic Field	123
5.4	Discussion of Results	127
6	Conclusion	131
6.1	Introduction	131
6.2	Summary of Experimental Results	132
6.3	Improvements and Future Work	136
6.4	Conclusion	138
	References	139
	A Magnetic Field Mapping	153
	B Helmholtz Coil Magnetic Field Measurements	161
	C Progression of ILFF in uniform magnetic field, increasing Electric field	163

D	ILFF peak damage and repair sequence	169
E	Analysis using QuickField	177
F	Letters of Permission	181

List of Figures

2.1	Illustration of an electrospray source. Conductive or polar fluid coating needle-like structure. A voltage is applied between the needle-like structure and an extraction electrode. With sufficiently high voltage, a Taylor cone forms on the curved surface of the fluid and ions and/or droplets are emitted.	11
2.2	Stress balance across a fluid meniscus.	12
2.3	Drawing of the Taylor cone. The cone is assumed to be infinite in size and a perfect conductor. The half-angle of the cone is α and the radius at a given point is R	15
2.4	Illustration of an electrospray thruster with all of the key elements called out. Electrospray thruster shown with optional acceleration electrode to control the I_{SP} (Triode configuration).	21

2.5	Illustration of a ferrofluid. The small spheres are single-domain magnetic nanoparticles such as Fe_2O_3 . Left: With no magnetic field applied, the magnetic nanoparticles are stably dispersed throughout the fluid. Right: Upon the application of a magnetic field, the domains of the magnetic field tend to align with the applied magnetic field. The magnetic nanoparticles stay dispersed in the ferrofluid.	26
2.6	A pool of ferrofluid exposed to a sufficiently strong magnetic field normal to its surface. Surface of fluid distorts, this is known as the Rosensweig instability. Left: Top-down view of Rosensweig instabilities. Ferrofluid above a 2.5 cm diameter magnet. Right: Side/Angled view of Rosensweig instabilities. The magnetic field was provided by an electromagnet. . . .	27
2.7	A pool of ferrofluid (blue) exposed to a magnetic field. Left: A pool of ferrofluid with no perturbations to the surface. Center: A slight deformation in the fluid surface focus the magnetic field. The ferrofluid is drawn toward the gradient in the magnetic field. Right: Rosensweig instability formed. The growth in the surface was caused by magnetic energy and limited by surface and gravitational energies. The Rosensweig instability is a minimization between magnetic, surface, and gravitational energies. This instability creates multi-tip modal patterns of peaks in the ferrofluid, such as those in Figure 2.6.	28

2.8	Illustration of Rosensweig instability. The critical wavenumber (wavelength) is shown as the spacing between two neighboring peaks.	31
2.9	Force balance for a magnetic drop in a uniformly applied magnetic field.	38
2.10	Magnetic drop in an externally applied magnetic field, H_0 . Drop is magnetized, M , causing “surface poles” leading to a demagnetizing field, H_d	39
2.11	Deformation of a conductive magnetic fluid. Left: Only a magnetic field applied. Middle: Magnetic field and moderate electric field applied. The fluid grew in height. Right: Magnetic field and stronger electric field applied. Much more noticeable increase in fluid height. Demagnification/Depolarization factor changing as the fluid shape changes.	43

3.1	Left: Stainless steel fluid holder. Pocket is 15.24 mm by 15.24 mm and 2.54 mm deep (0.6 in by 0.6 in and 0.1 in deep), radius of curvature in the pocket is 3.175 mm (0.125 in). The radius of the ridge is 0.635 mm (0.025 in). Right: Illustration of the schematic used to test the deformation of Rosensweig instabilities in combined magnetic and electric fields. Two electromagnets, drawn in red, in a Helmholtz configuration provided a uniform magnetic field to the ILFF (brown peaks). A blue fluid holder and blue counter electrode provided a potential difference between the ILFF and the counter electrode. The Helmholtz coil was built at MTU with each coil containing 250 wraps of 16 AWG magnet wire. The coil centers were 57.2 mm (2.25 in) apart and the inner diameter of the electromagnet coils was 133.4 mm (5.25 in). Each electromagnet coil was 25.4 mm (1.00 in) wide.	53
3.2	EAN based ILFF (batch # NJ332106). Left: No magnetic or electric field applied ($H = 0$ kA/m, $V = 0$ V). ILFF surface is flat and has no deformations. Middle: Only magnetic field applied ($H = 23.6$ kA/m, $V = 0$ V). ILFF surface deformed, Rosensweig instabilities appear on the fluid surface. Right: Magnetic and electric fields applied ($H = 23.6$ kA/m, $V = -6,000$ V). ILFF surface further deformed by the electric stress. Rosensweig instabilities grow in height and tips have a smaller radius of curvature.	54
4.1	Illustration of the cross-section of the electrospray source setup.	59

4.2	Image of aluminum fluid holder. Left: Without ILFF. Right: Trench filled with ILFF.	59
4.3	Image of the experimental setup (Photo Credit: Sarah Bird). Letter of permission to use photo in Appendix F.	60
4.4	Progression of EAN based ILFF peaks as voltage is applied. Left: an image of a single peak in the array of 5 peaks with no voltage applied (0 V). Middle left: image of the same peak with -3000 V applied. Peak height increases and tip becomes slightly sharper. Middle right: applied voltage has been increased to -3600 V, and the peak has grown in height and is sharper. Right: applied voltage is -3700 V. At this voltage, the array began emitting ions. Also notable is the presence of bubbles at the bottom of the rightmost image, most likely due to some electrochemical reaction. . . .	65
4.5	Emitted current and applied voltage versus time of EAN based ILFF. Green line denotes voltage and blue line denotes current.	67
4.6	Emitted current versus voltage. Blue line with open circles denotes the emitted current as the magnitude of the voltage was increased while the green line with crosses denotes the emitted current as the magnitude of the applied voltage was decreased.	68
4.7	ITO glass current collector and witness plate post emission test.	69

4.8	Series of images showing a peak emitting, become damaged, and then self-repair and begin emitting again, with no operator intervention. Left: Peak emitting ions, small bubbles visible at the base of the peak. Center: A large bubble appears in the peak, and emission from this peak ceases. Right: After the bubble burst, peak begins emitting ions again.	71
4.9	A zoomed-in image three emission sites on the tip of a single peak in an EAN-based ILFF.	72
4.10	EMIM-NTf2 based ILFF in annular fluid holder. Left: ILFF exposed to magnetic field only (Rosensweig instability). Right: ILFF exposed to magnetic and electric field, applied voltage was 2700 V, and emitting ions.	74
4.11	Voltage and measured current data from Run 1, also called Positive 1.	77
4.12	Voltage and measured current data from Run 2, also called Positive 2.	78
4.13	Voltage and measured current data from Run 3, also called Negative 1. Voltage magnitude shown, actual voltage was negative.	79
4.14	Voltage and measured current data from Run 4, also called Negative 2. Voltage magnitude shown, actual voltage was negative.	80
4.15	Multiple I-V traces of EMIM-NTf2 based ILFF (batch # NJ397028). The blue and green data represent the ILFF biased positively, and the red and black data are when the ILFF was biased negatively. All data are shown on positive axes for easier comparison.	81

<p>4.16 Multiple emission sites present on the tip of an emitting peak in an EMIM-NTf₂ based ILFF (batch # NJ397028). Onset voltage was 2750 V. The applied voltage was 3150 V.</p>	83
<p>4.17 Sequence of images elapsed over the course of less than 5 seconds with a constant voltage applied. In the left image, the peak on the right was emitting. In the middle image, the peak grew a long protrusion while still appearing to be emitting. The rightmost image the protrusion “exploded” and appeared to form a cone of spray. The applied voltage was -2750 V and biased negatively (emitting anions) and the collected current was between 150 and 225 μA. In all the images there was a downward-facing cone attached to the extraction electrode. This downward-facing cone was created because part of the spray being intercepted by the extraction electrode. After enough ILFF built up on the extraction electrode, the downward-facing cone appeared. It was unknown if this downward-facing cone was spraying toward the lower pool of ILFF.</p>	84
<p>4.18 Current collector after positive emission from I-V traces Positive 1 and Positive 2. There appeared to be 2-3 sites of emission.</p>	86

4.19 Sequence of images showing an ILFF tip with increasing applied voltages.

Dashed line drawn across the images to draw attention to the change in fluid height to the reader's eye. Top Left: Rosensweig instability only, $V = 0$ V. Top Left Middle: Rosensweig instability supplemented with an electric field, $V = 500$ V. Top Right Middle: Rosensweig instability supplemented with an electric field, $V = 1000$ V. Top Right: Rosensweig instability supplemented with an electric field, $V = 1200$ V. Bottom Left: Rosensweig instability supplemented with an electric field, $V = 2000$ V. Bottom Middle: Rosensweig instability supplemented with an electric field, $V = 2200$ V. Bottom right: Rosensweig instability supplemented with an electric field, $V = 2350$ V. The peak heights grow and tip radii shrink with applied voltage.

92

4.20 Pressure balance shown on a curved surface. The four pressures were gravity and surface tension working against electric and magnetic traction energy. The height and curvature of the interface was determined by these four energies.

93

4.21 Pressure contributions from capillary, electric, magnetic and gravitational sources as the ILFF was stressed by an increasing applied voltage. Magnetic pressure, blue with open circles, was constant. Gravitational pressure, cyan with open squares, had a very small increase as the applied voltage was increased and the ILFF Rosensweig instability grew in height. Electric pressure, green with x's, increased because of the increase in applied voltage and the change in shape of the fluid. Electric field determined using Equation 2.8. The capillary pressure, red with crosses, increased as the ILFF Rosensweig instability tip radius decreased as the voltage was increased. 95

4.22 Ratio of magnetic pressure to capillary pressure and electric pressure to capillary pressure for start-up test 5 as the applied voltage was increased. Magnetic pressure to capillary pressure shown as the blue curve with open circles. Ratio of gravitational to capillary pressures is shown as, a cyan curve with open squares. The ratio of electric pressure to capillary pressure is displayed as, a green curve with x's. Electric field determined using Equation 2.8. 96

4.23 Pressure contributions from capillary, electric, magnetic and gravitational sources as the ILFF was stressed by an increasing applied voltage. Magnetic pressure, blue with open circles, was constant. Gravitational pressure, cyan with open squares, had a very small increase as the applied voltage was increased and the ILFF Rosensweig instability grew in height. Electric pressure, green with x's, increased because of the increase in applied voltage and the change in shape of the fluid. The electric field was determined by modeling the system in QuickField. The capillary pressure, red with crosses, increased as the ILFF Rosensweig instability tip radius decreased as the voltage was increased. 98

4.24 Ratio of magnetic pressure to capillary pressure and electric pressure to capillary pressure for start-up test 5 as the applied voltage was increased. Magnetic pressure to capillary pressure shown as the blue curve with open circles. Ratio of gravitational to capillary pressures is shown as, a cyan curve with open squares. The ratio of electric pressure to capillary pressure is displayed as, a green curve with x's. The electric field was determined by modeling the system in QuickField. 99

4.25	Comparison of electric field versus applied voltage for the data from Run 5. The blue curve with open circles represents the electric field calculated using Equation 2.8 and the tip radius and tip-to-electrode distance. The red curve with open squares represents the electric field calculated for the same data set using a finite element analysis tool, QuickField, and the shape of the ILFF at each respective voltage.	100
5.1	Illustration of stack of magnets, orientation of magnetization, and coordinates.	109
5.2	Illustration of a Halbach array.	110
5.3	Illustration of Rosensweig instability wavelength measurement experimental setup.	113
5.4	Left: Typical image of ferrofluid above bar magnet exhibiting Rosensweig instability. Right: Image from the left with peak locations selected (green dots).	115
5.5	Image of ferrofluid on a linear Halbach array. The length of each individual magnet was 25.4 mm.	115

- 5.6 Plot of measured peak-to-peak spacing versus MVB of FerroTec EFH-1 ferrofluid. The thick black line denotes the peak-to-peak spacing predicted by Equation 2.27. The blue ‘*’ denotes the peak-to-peak spacings measured of the ferrofluid with the magnetic field supplied by the bar magnet described in Section 5.2.2. The red ‘+’ denotes the peak-to-peak spacings of the ferrofluid above the Halbach array described in Section 5.2.3. The rightmost thin black vertical line (at $\sim 1.2 * 10^5 A - T/m^2$) is where the magnetic body force is an order of magnitude stronger than the gravity body force, and the leftmost vertical line (at $\sim 1.2 * 10^4 A - T/m^2$) indicates where the two forces are equal. 118
- 5.7 Plot of the percent difference between measured peak-to-peak values and the peak-to-peak values predicted by Equation 2.27. Similar to Figure 5.6, blue ‘*’ denotes measured values using bar magnet, and red ‘+’ denotes measured peak-to-peak spacing using Halbach array. 119
- 5.8 Illustration showing two methods of defining peak-to-peak spacing of a ferrofluid where the Rosensweig instabilities formed on a curved fluid surface. The curved black mass was a ferrofluid, and the thin brown line was the substrate the ferrofluid sits on, and the red rectangle represented the magnet below the ferrofluid. The blue lines represented the peak-to-peak measurement used in this dissertation. The green lines represented a peak-to-peak measurement at the base of the peaks. 121

5.9	Left: Connected ferrofluid peaks created by the Rosensweig instability, as described in the work presented in this dissertation. Fluid volume estimated by assuming it was a cone shape. The shaded portion of the illustration was the what was considered a peak for the analysis. Right: Ferrofluid drop as described by Timonen et al on a superhydrophobic surface. The shaded portion of the drop (the whole drop) was used to determine the drop volume.	125
5.10	Measured peak-to-peak spacing versus the fifth root of the magnetic moment over the second derivative of the magnetic field. The blue ‘*’ denotes measured values, and the black line denotes a linear fit to the data.	126
5.11	Depiction of peak-to-peak spacing for a continuous ferrofluid and discontinuous ferrofluid. Left: In a ferrofluid where all of the peaks are connected, the peak size can change, and the peak diameter and peak-to-peak distance was governed by Equation 2.27. Right: Individual ferrofluid drops in a non-uniform magnetic field. The maximum diameter of the drop was confined to be no larger than the value provided in Equation 2.27, while the peak-to-peak spacing was set by Equation 2.31	129
A.1	Illustration of stack of magnets, orientation of magnetization, and coordinates. (Same as Figure 5.1, shown here for convenience.)	153
C.1	ILFF (EAN with Sirtex magnetic nanoparticles) with a magnetic field of 0 Gauss and applied voltage of 0 V.)	164

C.2	ILFF (EAN with Sirtex magnetic nanoparticles) with a magnetic field of 297.1 Gauss and applied voltage of 0 V.)	164
C.3	ILFF (EAN with Sirtex magnetic nanoparticles) with a magnetic field of 297.1 Gauss and applied voltage of -1000 V.)	165
C.4	ILFF (EAN with Sirtex magnetic nanoparticles) with a magnetic field of 297.1 Gauss and applied voltage of -2000 V.)	165
C.5	ILFF (EAN with Sirtex magnetic nanoparticles) with a magnetic field of 297.1 Gauss and applied voltage of -3000 V.)	166
C.6	ILFF (EAN with Sirtex magnetic nanoparticles) with a magnetic field of 297.1 Gauss and applied voltage of -4000 V.)	166
C.7	ILFF (EAN with Sirtex magnetic nanoparticles) with a magnetic field of 297.1 Gauss and applied voltage of -4500 V.)	167
C.8	ILFF (EAN with Sirtex magnetic nanoparticles) with a magnetic field of 297.1 Gauss and applied voltage of -5000 V.)	167
C.9	ILFF (EAN with Sirtex magnetic nanoparticles) with a magnetic field of 297.1 Gauss and applied voltage of -5500 V.)	168
C.10	ILFF (EAN with Sirtex magnetic nanoparticles) with a magnetic field of 297.1 Gauss and applied voltage of -600 V.)	168
D.1	EAN based ILFF emitting ions at -3700 V of extraction voltage. Image was taken roughly 3 minutes before large bubble formed.	169

D.2	Large bubble forming in EAN based ILFF. Emission from this peak ceased. Voltage decreased to -3200 V by the user because they didn't want to break anything.	170
D.3	Image after the bubble popped in the ILFF popped. Two smaller peaks formed from the previously one larger peak. Voltage was -3200 V. This image was less than a minute after the bubble popped.	171
D.4	ILFF peaks continue to grow and separate. Voltage was increased to -3450 V. Image taken roughly one minute after bubble burst.	172
D.5	The two new ILFF peaks separate even further and grow in height. Voltage was increased to -3500 V. Image taken roughly 2 minutes after bubble burst.	173
D.6	The right peak continues to grow in height, and the tip of the peak appears to be getting much sharper. There also seems to be a bit of asymmetry to the peak. The applied voltage was maintained at -3500 V. This image was taken roughly 2 minutes after the bubble burst.	174
D.7	The tip of the ILFF split into 3 emission sites spaced out symmetrically around the tip. The voltage remained constant at -3500 V and this was roughly 3 minutes after the bubble burst.	175
D.8	A zoomed-in image of Figure D.7, with an additional insert focusing on the three emission sites at the tip.	175

D.9	Roughly fifteen minutes after the bubble burst in the ILFF, the peak under observation transitions from the multiple emission site mode to a single emission site mode. The applied voltage was increased to -3600 V. . . .	176
E.1	Electric field results from QuickField with an applied voltage of 1000 V applied between ILFF (lower left geometry) and extraction electrode (right boundary). Geometry from Run 5 at 0 V.	177
E.2	Electric field results from QuickField with an applied voltage of 1000 V applied between ILFF (lower left geometry) and extraction electrode (right boundary). Geometry from Run 5 at 500 V.	178
E.3	Electric field results from QuickField with an applied voltage of 1000 V applied between ILFF (lower left geometry) and extraction electrode (right boundary). Geometry from Run 5 at 1000 V.	178
E.4	Electric field results from QuickField with an applied voltage of 1000 V applied between ILFF (lower left geometry) and extraction electrode (right boundary). Geometry from Run 5 at 1200 V.	179
E.5	Electric field results from QuickField with an applied voltage of 1000 V applied between ILFF (lower left geometry) and extraction electrode (right boundary). Geometry from Run 5 at 2000 V.	179
E.6	Electric field results from QuickField with an applied voltage of 1000 V applied between ILFF (lower left geometry) and extraction electrode (right boundary). Geometry from Run 5 at 2200 V.	180

E.7	Electric field results from QuickField with an applied voltage of 1000 V applied between ILFF (lower left geometry) and extraction electrode (right boundary). Geometry from Run 5 at 2350 V.	180
F.1	Letter of permission to use Figure 4.3 in this dissertation. Signature redacted.	181

List of Tables

3.1	Comparison of ILFFs	49
4.1	FerroTec EFH-1 Fluid Properties	63
4.2	ILFF Peak information for Runs 1-4	81
4.3	Measured and predicted values comparing measured onset voltage to predicted onset voltage. Tip radius and Tip-electrode spacing were measured with no applied voltage/electric field.	88
4.4	Deformation of ILFF as voltage was applied to Run 5. The starting voltage was 2390 V.	94
5.1	FerroTec EFH-1 Fluid Properties	108
A.1	Magnetic field (Gauss) in the B_z at coordinate $x = 0.0 \text{ mm}$	154
A.2	Magnetic field (Gauss) in the B_z at coordinate $x = 25.4 \text{ mm}$	155
A.3	Magnetic field (Gauss) in the B_z at coordinate $x = 50.8 \text{ mm}$	156
A.4	Magnetic field (Gauss) in the B_y at coordinate $x = 0.0 \text{ mm}$	157
A.5	Magnetic field (Gauss) in the B_y at coordinate $x = 25.4 \text{ mm}$	158
A.6	Magnetic field (Gauss) in the B_y at coordinate $x = 50.8 \text{ mm}$	159

B.1 Axial magnetic field on center-line of the Helmholtz coil described in Section 3.5 at various driven currents.	162
---	-----

Acknowledgements

This manuscript is the result of years of late nights, hard work, and support from so many people. It has been a truly amazing experience. I apologize if I have missed anyone.

First, I would like to thank my advisor Brad King for all the help and guidance he has provided throughout the years. Brad got his hooks into me as freshman with the Aerospace Enterprise. Just when I thought I was going to leave Michigan Tech for new adventures, Brad gave me his sales pitch for sticking around to get a Ph.D. This sales pitch highlighted all of downsides of performing research and being a graduate student. To say the least, Brad is one heck of a salesman because that speech got me to stay at Michigan Tech for a number of years.

A big thank you goes out to my committee Dr. Jeff Allen, Dr. Chang Choi, and Dr. Ben Prince. Thank you for providing me with guidance and technical assistance throughout my research and my time at Michigan Tech. Dr. Prince, thank you for allowing me to work with your group out at Kirtland AFB, and for imparting some of your knowledge on mass spectrometry and electrosprays onto me.

I would like to thank those that have supported me and my research. My research has been funded by the United States Air Force Research Laboratory (AFRL) and the Michigan/Air Force Center for Excellence in Electric Propulsion (MACEEP). MACEEP allowed for

collaboration in the early stages of my work with Dr. Debbie Levin and Arnaud Borner at Penn State. It was valuable learning about molecular dynamic simulations. I also feel very honored to have been awarded the Winnekow Fellowship for the past year. I hope I have lived up to the expectations of this award.

The work contained in this manuscript would not have been possible without Dr. Brian Hawkett and Nirmesh Jain at the University of Sydney. Nirmesh and Brian have produced a number of batches of ionic liquid ferrofluid which has enabled my work to even be possible. I know that I could not do what they do. I know this as a fact, because I tried and failed.

To the master machinist Marty Toth who has helped me become a better designer. Thank you for all the components and assemblies you have spent hours fabricating. You have always had the best “stories from the shop”.

Fellow ISPers, former and present. It has been an experience working with you all. Jason and Jason it has been fun working with you both, in and out of the office/lab. Rob, I learned a lot from working with you and helping you prepare and execute a 40-hour test. Thank you for introducing me to the world of cigars! Mark, I can't thank you enough for the help you've provided over the years, between the Lab View support, the heated discussions about how to design and/or assemble just about everything, and especially for pointing me in the direction of ferrofluids. Kurt, good luck continuing on with the electrospray research. I hope it treats you well. Thank you for letting me live in your house while you play around in New Mexico. To the new guard. It has been a pleasure working with you both Amanda

and Brandon. Good luck!

I really need to thank my family, especially my parents. They have done everything they can throughout the years to provide me with a good foundation, provide me with every opportunity to succeed, and have always supported me in all my endeavours. Thank you Mom for always listening even if you have no idea what I'm talking about. Thank you Dad for all the talks we have had and all of the tidbits of knowledge you have shared over all of the years. My sister Melissa and brother-in-law Bob and niece and nephew Emmy and Bobby have always been constant supporters of me too.

Last, and certainly not least, I would thank my fiancé Angela who has stood by me and provided motivation throughout all the ups and downs of process that is grad school. Thank you for all the love and support you have provided me. I love you.

Edmond J. Meyer IV

July 2014

Abstract

An electro spray source has been developed using a novel new fluid that is both magnetic and conductive. Unlike conventional electro spray sources that required microfabricated structures to support the fluid to be electro sprayed, this new electro spray fluid utilizes the Rosensweig instability to create the structures in the magnetic fluid when an external magnetic field was applied. Application of an external electric field caused these magnetic fluid structures to spray. These fluid based structures were found to spray at a lower onset voltage than was predicted for electro spray sources with solid structures of similar geometry. These fluid based structures were also found to be resilient to damage, unlike the solid structures found in traditional electro spray sources. Further, experimental studies of magnetic fluids in non-uniform magnetic fields were conducted. The modes of Rosensweig instabilities have been studied in-depth when created by uniform magnetic fields, but little to no studies have been performed on Rosensweig instabilities formed due to non-uniform magnetic fields. The measured spacing of the cone-like structures of ferrofluid, in a non-uniform magnetic field, were found to agree with a proposed theoretical model.

Chapter 1

Introduction

1.1 Electrospray Thrusters

An electrospray thruster is a type of micro-electric propulsion device for spacecraft. An electric field extracts ions and/or charged droplets out of the propellant, and accelerates them to create thrust. Traditional electrospray thrusters use a fluid coated on or contained in some sort of solid structure, such as a needle, or capillary. The liquid propellant, either a liquid metal or ionic liquid, is conductive and/or polar and can be stressed by an electric field. Applying a voltage between the fluid and the extraction electrode stresses the fluid, drawing it towards the tip of the needle. If sufficient voltage is applied, the fluid forms a Taylor cone, and will begin to emit ions or charged droplets out of the propellant. The

ions or charged particles are then accelerated in the electric field between the needle or capillary and extraction grid. These accelerated particles are then ejected from the vehicle into space. The momentum exchange of ejecting ions or charged droplets at a high velocity is what provides the thrust for a spacecraft.

A single emission site can provide thrust in the range of $10^{-5} - 10^1 \mu\text{N}$ [1]. The thrust from a single emission site is too low to meet the thrust requirements of almost all missions. Thrust for an electrospray thruster is increased by utilizing multiple emission sites in parallel. Because of this, electrospray thrusters are typically fabricated by creating a large array of needle or capillary-like structures that retain propellant and promote multiple emission sites.

To fabricate these arrays, micromanufacturing techniques are typically applied, such as photolithography and wet etching of materials such as silicon and silicon dioxide. Other materials such as porous nickel and porous tungsten have been used to create arrays of needle-like structures. Fabrication of these arrays is time intensive and does not always yield uniform tips, and the resulting arrays are very fragile to damage during handling, assembly, and operation. Some manufacturing techniques can create non-uniform arrays of needle-like structures, which reduces the effective packing density because not every tip will emit. Another issue with electrospray thrusters is longevity. During the lifetime of the array, propellant can accumulate on the extraction electrode and can lead to shorting out the array, making the array inoperable. Another issue concerning longevity is the

underlying structure that supports the fluid. It has been shown to blunt over time due to heavy ion bombardment, and electrochemistry eroding away the needle or capillary. The electrochemistry issue has recently been alleviated by some techniques developed by Lozano's group at MIT [2].

The research presented here uses a new propellant called an ionic liquid ferrofluid (ILFF) that does not require a support structure, yet still forms regularly spaced needle-like structures, or peaks. These peaks, made of the propellant, have shown that they can be damaged and then self-repair *in-situ* and continue to work. Using this new propellant, the tips can be created in a matter of seconds by applying a magnetic field compared to weeks to fabricate a substrate.

These peaks made of propellant are formed by the application of a magnetic field, and are called Rosensweig instabilities. When these magnetically manufactured peaks are further stressed by an electric field, they begin to emit ions and/or charged droplets. Additionally, when the ILFF is exposed to a non-uniform magnetic field, the packing density of the peaks could be greatly increased.

1.2 Aim and Scope

The goal of this work was to (1) demonstrate that an ionic liquid ferrofluid could be stressed by both magnetic and electric fields, (2) electro spray an ionic liquid ferrofluid without the need of a support structure, (3) determine how the wavelength of the Rosensweig instability scales in a non-uniform magnetic field, and (4) predict the smallest reasonable Rosensweig instability wavelength obtainable in a non-uniform magnetic field.

The scope of this work was to first build and demonstrate an electro spray source created by peaks formed in an ILFF using an applied magnetic field, and to excite ion and/or droplet emission from these peaks with an externally applied electric field. Second, some performance characteristics of this electro spray source were to be measured, namely the I-V characteristics. Third, the scope included measuring and understanding the onset voltage to obtain emission. The final item that was in the scope of this work was to measure the peak-to-peak spacing of Rosensweig instabilities in a non-uniform magnetic field, and then compare these measured values to two models.

There are a number of items of interest to this research, but were considered outside the scope of this work. This is not an all-inclusive list of items out of scope. First, the mass-to-charge of the spray is important to know because it is a key piece of information relating to the thruster performance, such as thrust and I_{SP} . Another factor that is important

is characterizing the beam, namely the spray pattern. It is also possible that the applied magnetic field modifies the spray angular distribution compared to other electrospray sources. Understanding the angular distribution of the spray sets bounds on the design of the extraction electrode geometry. Another item out of scope is measuring the mass flow rate of the spray. Knowing the mass flow rate across all the operating parameters will allow for a feed system to maintain a constant level of ILFF in the peaks, allowing for consistent performance. The design of the fluid holder, and the spacing of the electrode and the size of the opening in the extraction electrode contribute to the performance of an electrospray device. These items are outside of the scope of this work, in part because they rely on measuring parameters that are also outside the scope of this work. A coupled set of ferrohydrodynamic and electrohydrodynamic equations would provide insight into how the electric and magnetic instabilities scale, and may be used to describe the ILFF shape deformations in a combined electric and magnetic field. Developing these equations, along with the other items called out in the paragraph are considered items of interest regarding the research presented in this dissertation, however, they are out of the scope of this work.

1.3 Structure

Chapter 2 of this work provides a brief background on electrosprays, followed by important relations for propulsion devices in space, the benefits of electrospray thrusters, and what type of role they can provide the space propulsion community. Next is a brief overview

of some of the current state-of-the-art fabrication techniques used to build electro spray devices, this is followed by some alternative fabrication techniques attempted at Michigan Technological university and how they led to the research presented in this dissertation. Chapter 2 then provides a background on ferrohydrodynamics and Rosensweig instabilities, followed by two techniques used to describe the behavior of a ferrofluid in a non-uniform magnetic field. Chapter 2 finishes with energy analysis of the Rosensweig instability, and then explores the energies of a magnetic drop and a conductive drop. These sections are then combined and presented as the energy balance of an ILFF in a combined electric and magnetic field.

Chapter 3 details the work to build and test an electro spray source. This electro spray source was operated with two different ILFFs. Each of these ILFFs had their I-V performance measured. A study measuring the onset voltage of the ILFF based electro spray source was also conducted and compared to theory. This chapter also reports on other phenomenon that were observed during testing.

Studies on the peak-to-peak spacing of a ferrofluid in a non-uniform magnetic field are reported and analysed in Chapter 4. By determining how the peak-to-peak spacing was dependent upon the non-uniformity of the magnetic field, one can determine what packing density could be obtained from a given magnetic field.

Finally, Chapter 5 wraps up the dissertation with a conclusion on all of the work presented. It also details where improvements can be made on this work, and details a few questions

that were outside the scope of this work.

Chapter 2

Background and Review of Prior Research

2.1 Introduction

This chapter begins with a background and review of electrosprays, the benefits and capabilities of electrospray thrusters, and the typical fabrication techniques used in the creation of electrospray thrusters. Following this background, the history of the development of the work presented here is given. This is followed by background on the Rosensweig instability formation in a uniform magnetic field and the representative equations. Next is a look at a hypothesized modification of the dispersion relation when a

ferrofluid is exposed to a non-uniform magnetic field. The energy balance of Rosensweig instabilities is provided, followed by a look at the energy of a magnetic drop in an applied magnetic field. A the energy of a polar fluid drop in an electric field is then discussed, as well as a discussion, and modification to these equations for a conductive fluid drop in an electric field. The observations of the magnetic and conductive drops in their respective fields are then applied to Rosensweig instabilities and it is hypothesized that both the magnetic and electric energies both increase with a growth in Rosensweig instability peak height, which could have implications on the required voltage to obtain electrospray.

2.2 Electrospray

2.2.1 Obtaining spray from an Electrospray Source

Electrospray is a process where ions or clusters of ions are extracted from a conductive or polar liquid. Ions or charged droplets are extracted from the liquid when the local electric field is sufficiently high. An illustration of an electrospray source is provided in Figure 2.1. Electrospray of ions occurs when there is an imbalance of stresses at the fluid interface. Surface tension tends to keep a fluid together, while an applied electric field can stress a fluid interface. This stress balance is shown in Figure 2.2.

Both a polar and conductive fluid can be electrosprayed. The electrical stress tensor in a

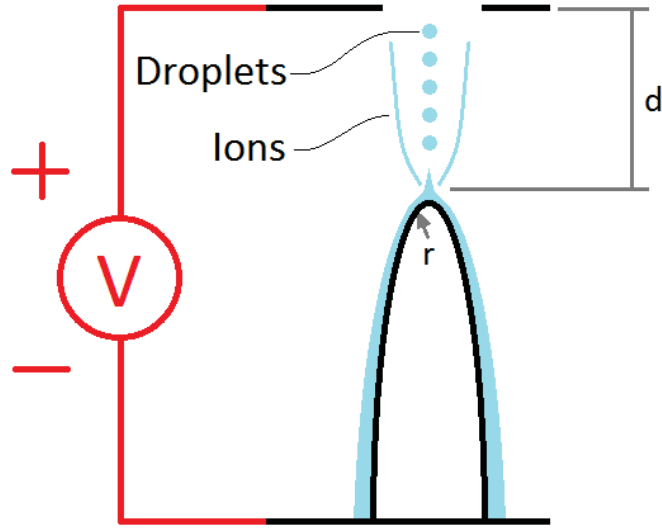


Figure 2.1: Illustration of an electrospray source. Conductive or polar fluid coating needle-like structure. A voltage is applied between the needle-like structure and an extraction electrode. With sufficiently high voltage, a Taylor cone forms on the curved surface of the fluid and ions and/or droplets are emitted.

medium, is

$$[T] = \epsilon \vec{E} \vec{E} - \frac{1}{2} \epsilon_0 E^2 [I] \quad (2.1)$$

where E is the electric field in that medium, ϵ is the permeability, ϵ_0 is the permeability of free space, and $[I]$ is the identity matrix. The normal component of the electric displacement field across a boundary does not change, and expressed as an electric field

$$\epsilon_0 E_n = \epsilon_0 \epsilon_r E_{n1} \quad (2.2)$$

where E_n is the normal component of the vacuum electric field, ϵ_r is the relative

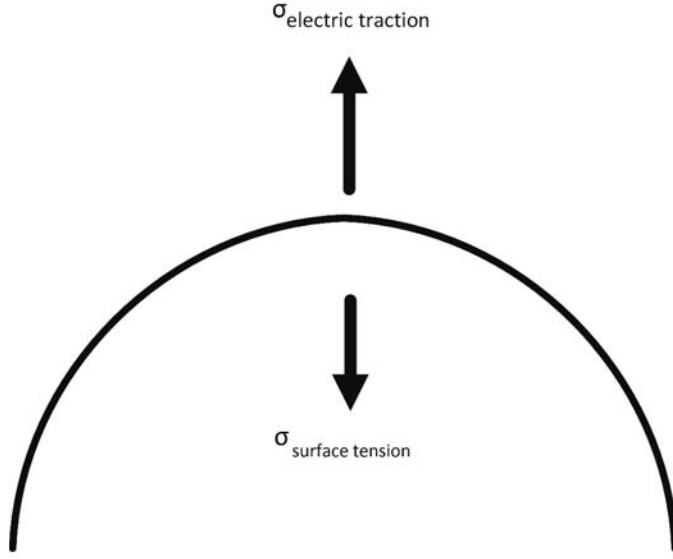


Figure 2.2: Stress balance across a fluid meniscus.

permittivity of the fluid, and E_{n1} is the normal component of the electric field internal to the fluid. The electric stress across the interface is written as

$$\sigma_E = [[T_{11}]] = \left(\epsilon_0 E_n^2 - \frac{1}{2} \epsilon_0 E_n^2 \right) - \left(\epsilon_0 \epsilon_r E_{n1}^2 - \frac{1}{2} \epsilon_0 E_{n1}^2 \right) \quad (2.3)$$

where the double brackets indicate the jump across an interface. Inserting Equation 2.2 into Equation 2.3 to replace the E_{n1} terms, and assuming the electric field is normal to the surface yields an electric stress of

$$\sigma_E = [[T_{11}]] = \frac{1}{2} \epsilon_0 E^2 \left(1 - \frac{2}{\epsilon_r} + \frac{1}{\epsilon_r^2} \right). \quad (2.4)$$

Equation 2.4 is the electrical stress at a material-fluid interface in a general sense, as in it applied to insulators, polar materials, and conductors. For a perfect conductor, the

relative permittivity can be assumed to approach infinity, resulting in the commonly used expression

$$\sigma_E = \frac{1}{2} \epsilon_0 E^2. \quad (2.5)$$

For a polar fluid with a relatively high permittivity, say above 20, Equation 2.5 can be used to approximate the surface stress. With a relative permittivity of 20, Equation 2.4 is 90% the value of Equation 2.5. Water, for instance, has a relative permittivity around 80. Therefore for conductors and many if not most polar materials Equation 2.5 accurately describes the stress across a vacuum-material interface.

Electrospray occurs when the electrical stress, Equation 2.5, is greater than the surface tension stress

$$\sigma_{surface} = \frac{2\sigma}{r} \quad (2.6)$$

where σ is the surface tension of the fluid and r is the radius of the fluid. First the effects of the electric field will be examined, followed by the way in which the geometries influence the stress balance.

Taylor [3] studied the phenomenon of surface deformation of a liquid leading to electrospray which was first observed and reported by Zeleny [4]. Taylor determined the conditions where a conical liquid shape could exist in equilibrium between surface stresses

and electric stresses. Taylor assumed at equilibrium the fluid shape would be that of a cone, see Figure 2.3. For his analysis he assumed the cone was infinite in size and a perfect conductor. Taylor developed

$$V = V_0 + AR^{\frac{1}{2}}P_{\frac{1}{2}}(\cos \theta) \quad (2.7)$$

where V was the potential of the surface, V_0 was the applied voltage, A was an arbitrary constant, R was the radius of the cone, and $P_{\frac{1}{2}}$ is the Legendre function of order $\frac{1}{2}$, and θ is the angle outside of the cone. Using the assumption that the cone was a perfect conductor led to $V = V_0$. For the case of a perfect conductor, the only solution for all R was $P_{\frac{1}{2}} = 0$. This led to a cone half-angle of $\alpha = 49.3^\circ$.

The Taylor cone forms when the electrostatic stress and the surfaces stresses are in equilibrium. The typical configuration of the state of the are electro spray sources are for the fluid to be supported by some sort of needle-like or capillary-like structure. This structure, namely the radius of this structure, is what provides the fluid with its initial radius of curvature. The paraboloidal structure, shown in Figure 2.1, enhances the electric field near the tip to be

$$E = \frac{2V}{r \ln \frac{2d}{r}} \quad (2.8)$$

as described by Prewett and Mair. [5]

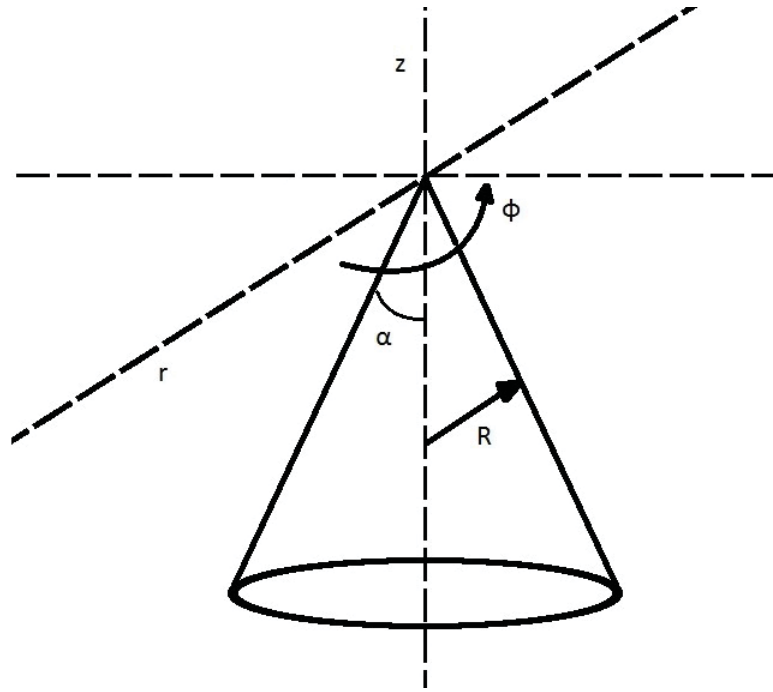


Figure 2.3: Drawing of the Taylor cone. The cone is assumed to be infinite in size and a perfect conductor. The half-angle of the cone is α and the radius at a given point is R .

An expression for the required voltage for electro spray to occur (or onset voltage)

$$V = \ln\left(\frac{2d}{r}\right) \sqrt{\frac{\sigma r}{\epsilon_0}} \quad (2.9)$$

was developed by combining the surface tension stress, Equation 2.6, and electrical stress, Equation 2.5, with the local electrical field, Equation 2.8 and solving for voltage. [5]

At or above this voltage, the electrical stress overcomes that of the surface tension and electro spray occurs. A typical fluid wants to minimize its energy so it either tries to form a sphere in free space, or have a flat surface for an pool of infinite size under gravity conditions. To have the fluid in a paraboloidal shape, the fluid is wetted onto a support

structure of the desired shape, such as a needle or hollow capillary. This base structure provides the electric field enhancement and allows for the emission to occur in predictable locations (i.e. from the tips of the paraboloids).

With electrosprays, it has been commonly stated that electrospray occurs when the local electric field exceeds 10^9 V/m. Krpoun and Shea developed a model to correlate fluid tip radius (for a given emitter geometry) against voltage required to sustain the shape. [6] What Krpoun and Shea found was when the Taylor angle was used as the underlying geometry, the required voltage plateaued at a given point as the tip radius was decreased (even by orders of magnitude). The electric field where the critical radius occurred was well below the 10^9 V/m benchmark. However, it is believed that because of this plateau, as soon as the critical radius/voltage point was reached, the tips radius sharply decreased and onset of emission began as local electric field increased above the 10^9 V/m benchmark.

2.2.2 Background of Important Electric Propulsion Thruster Parameters

Electrospray sources can be used as thrusters for spacecraft. This section outlines a number of the background parameters that are important when determining the performance of thruster technology. The first parameter presented is thrust. Thrust, T , in a rocket in space is provided by expelling a propellant at a set mass flow rate, \dot{m} , at a given velocity, v_e .

Thrust is written as

$$T = v_e \dot{m} = I_{SP} g \dot{m}. \quad (2.10)$$

Specific impulse is the total impulse divided by the mass of the propellant to create the impulse. Mathematically, specific impulse, I_{SP} , is written as $I_{SP} = \frac{v_e}{g}$ where g is the acceleration due to gravity on Earth. I_{SP} has units of seconds, and is convenient because it has the same value in both English and Metric unit systems. Thrust can be increased by either increasing the mass flow rate or by increasing the specific impulse (exit velocity). The required power to operate a thruster is the ratio of kinetic jet power to electrically supplied power, η , times the time rate of change of the kinetic energy of the exhausted fuel. This relation for required power is

$$P = \frac{1}{2} \eta \dot{m} v_e^2 = \frac{1}{2} \eta \dot{m} g^2 I_{SP}^2. \quad (2.11)$$

Similarly to the thrust, the required power increases with both mass flow rate and/or the specific impulse of the rocket engine. A common quantity to relate is the thrust to power, or how much propulsion a rocket engine can provide for a given amount of input power. This is of particular importance for electric propulsion because generally the limiting factor for electric propulsion is the available power. This is because many to most of the satellite missions rely on solar panels to provide electrical power, and thus the available power is a function of the area of the solar cells and the solar flux. The thrust-to-power relation is

$$\frac{T}{P} = \frac{2\eta}{v_e} = \frac{2\eta}{gI_{SP}}. \quad (2.12)$$

The thrust to power is proportional to the efficiency, but inversely proportional to the specific impulse, and invariant to the mass flow rate. Assuming the rocket efficiency is constant across all operating conditions and a spacecraft's propulsion is power limited (because the amount of power collected by solar cells is finite), then there is a trade-off between thrust and specific impulse. Increasing the specific impulse means that the spacecraft produces less thrust for the same amount of input power. Specific impulse plays another important role in mission planning. The rocket equation [7] is

$$\Delta v = gI_{SP} \ln \frac{m_0}{m_f}, \quad (2.13)$$

and relates mission cost in the required change in velocity, Δv , to the specific impulse, initial spacecraft mass (including fuel), m_0 and final spacecraft mass (mass required to perform science mission), m_f . A given mission, whether it is a phasing maneuver, a change in inclination, or traveling to another celestial body, has a cost in Δv . When a spacecraft gets to its final destination, it requires a set amount of mass to perform its mission, which could be to collect a sample from an asteroid, relay telecommunication data, or travel to another planet. A launch vehicle can only supply a limited amount of mass into space, setting a maximum mass for the initial mass of the spacecraft (including the fuel required to perform the mission). These three parameters set the minimum required specific impulse for the mission. Another way to think of it is that the specific impulse is a rating of the fuel

economy of the spacecraft.

2.2.3 Performance of Electrospray Thrusters and Comparable Electric Propulsion Devices

Electrospray sources have been used as propulsion devices on spacecraft. [8] Electrospray thrusters have a needle-like or capillary protrusion which supports the propellant, typically an ionic liquid, and an extraction with a hole orientated above the needle, see Figure 2.4. A voltage is applied between the needle (or the propellant [2]) and the extraction electrode. The strong electric field acting on the fluid at the tip of the needle or capillary extractions ions and/or charged droplets out of the fluid and accelerates them through the hole in the extraction grid. Some electrospray thrusters are operated in a triode configuration so that the spray velocity can be controlled after extraction. The exit velocity, v_e of the ion or charged droplet extracted is proportional to the square root of the total charge, q of the ion or droplet, the acceleration voltage, V , and is expressed as

$$gI_{SP} = v_e = \sqrt{\frac{2qV}{m}}. \quad (2.14)$$

Electrosprays can extract and accelerate pure ions (pure-ion regime), and large charged droplets (droplet regime), and everything in between (mixed regime), depending on the operational mode employed. [9–11] The charges of the emitted particles can be positive

or negative, depending on the biasing of the fluid. Because of this range of charges and masses, electrospray thrusters can be operated in a large array of specific impulses, ranging from 100-10000 s with a thrust per emitter tip in the range of $10^{-8} - 10^{-6}$ N with thrust efficiencies greater than 80%. [10,12,13] The two biggest advantages of electrospray thrusters are the range of the specific impulse allows it to perform a wide range of missions and electrospray thrusters scale down easily, and they can be scaled up as well. Increasing the thrust of an electrospray system (for a given performance parameter) is fundamentally as easy as adding additional needles or capillaries. However, in practice, scaling from a single emitter tip to thousands of emitter tips has met with challenges. This is an active field of research for electrospray thrusters.

To date, electrospray thrusters have found a niche market in spacecraft systems that require low, controlled thrust levels, with low thrust noise, such as the LISA Pathfinder mission. [8] Electrospray thrusters are being investigated as propulsion devices to enable small spacecraft to have a means to change orbit and/or maintain orbit. [14] One of the hold-ups on the existing electrospray technology is that in order to meet the mission thrust requirements, the electrospray thrusters need multiple emission sites operating in parallel. There has not yet been a flight-ready design that packages hundreds to thousands of electrospray emitters in a single thruster head.

Other electric propulsion devices exist and have been used on satellite mission such as gridded ion thrusters and Hall-effect thrusters. These devices produce thrust by colliding

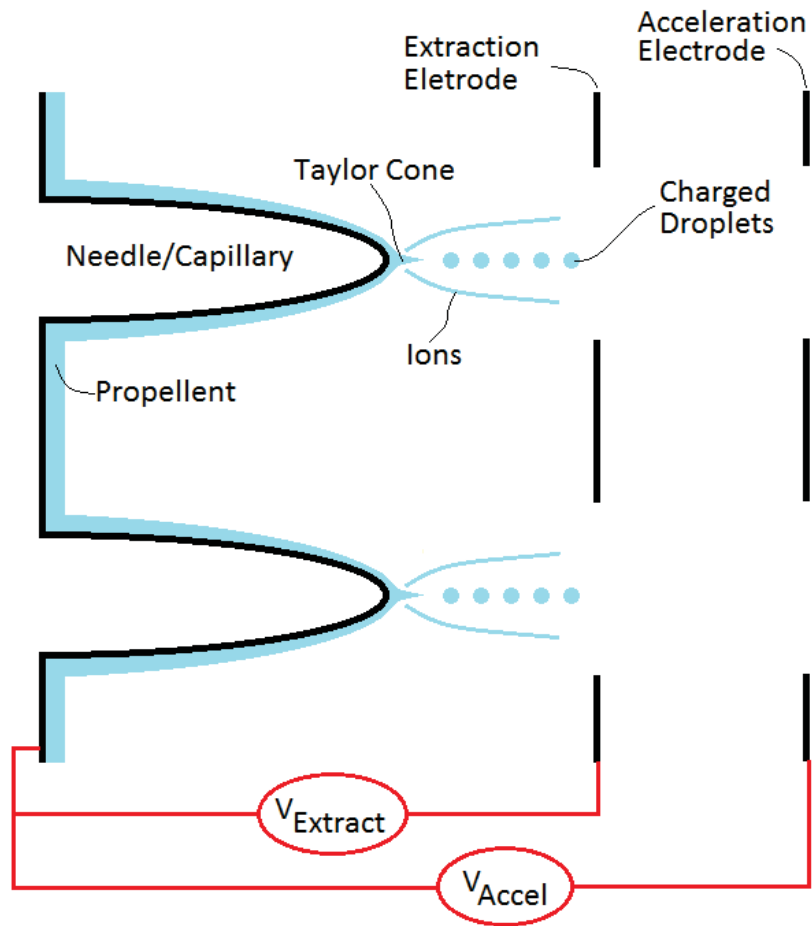


Figure 2.4: Illustration of an electro spray thruster with all of the key elements called out. Electro spray thruster shown with optional acceleration electrode to control the I_{SP} (Triode configuration).

high speed electrons into neutral gas particles to ionize the gas particles and then accelerate the ionized gas particles away from the spacecraft. These devices scale well to large sizes, but they cannot easily be scaled down. Hall-effect thrusters for instance require higher plasma densities and stronger magnetic fields as they scale down, both become technically challenging and can decrease thruster performance. The electron source also has challenges at smaller scales. Because of the limitations on the ability to downscale the

existing technology, electro spray devices inherently are micro-scale devices and thus have the unique ability to enable propulsion on small spacecraft, enabling new missions.

2.2.4 Fabrication Techniques of Electro spray Thrusters

A suitable application for electro spray thrusters would be enabling CubeSats to have a propulsion system. A CubeSat is a small satellite with common dimensions of 100 mm by 100 mm by 300 mm, and a mass in the 3-4 kg range. The thrust ranges for a CubeSat would be in the range of $10^{-5} - 10^{-4}$ N. [14] Based on the performance of existing electro spray sources, arrays of 10 to 10^4 emitters would be required to fulfil this role. The thruster, propellant, and thruster power supply would also ideally fit within half of a “U”, or fit within a volume of 50 mm by 50 mm by 100 mm. Realistically this would limit the size of the thruster head to be less than 80 mm per side. If 1000 emitters were required to meet the thrust requirement, the packing density of the emitter tips would be tighter than 6.4 mm^2 per tip. Multiple research groups have dedicated resources to determining how to pack a large number of emission sites in a small footprint.

The first type of emitter fabrication is where each emitter is fabricated individually, typically by hand. For NASA’s Active Spacecraft Potential Control (ASPOC) instrument of their Magnetospheric Multiscale Mission, they have a number of liquid metal ion sources (LMIS) [8]. Each of these LMIS is a capillary attached to a heater and propellant reservoir.

Every one of these emitters is assembled by hand into a thruster head. One of the main disadvantages of this type of electrospray array fabrication is that it is tedious and time consuming and not practical for building an array with high emitter counts.

One of the common methods currently employed is to use photolithography and wet etching of silicon wafers or porous metals. In this technique, a photo resist is applied to the surface of a porous metal or silicon wafer. A pattern is then hardened into the photo resist using a mask. The unhardened photo resist and the underlying material (porous metal or silicon) are then chemically etched away, leaving a desired structure. The remaining photo resist is then removed. This process is repeated until the final component geometries are created. This process has been used to create 1-D arrays of porous metal emitters [15,16]. It has also been used to create 2-D arrays of porous metal emitters [17,18] and silicon-based emitters [1,19]. The 2-D arrays have both the emitters and the extraction grids fabricated using photolithography and etching methods. In the case of the arrays fabricated by Gassend et al [1] they created a fixture that would accept and lock into place the silicon wafer with the emitter sites, and then accept and position the extraction grid above the emitter sites. Other techniques of securing and positioning the extraction grid to the emitter sites have been used, such as ruby spheres by Krpoun and Shea [19]. A big advantage of this type of array fabrication is that tens to thousands of emission sites can be fabricated concurrently. These emitter arrays, however, are timely to manufacture, some of the techniques do not always yield usable arrays, and the arrays are delicate and can be easily damaged.

A newer technique to manufacture arrays of electrospray sources used photolithography in an additive process instead of a subtractive process [20]. This technique created capillaries by building up a photo resist on a substrate. An additional layer of photo resist was added as an electrical spacer, and then on the upper surface of the photo resist, a conductive layer was added as the extraction electrode.

Finally, the last technique for creating emitters is powder injection moulding. Vasiljevich et al created a circular array porous metal emitter tips, which look similar to a crown [21,22]. This manufacturing technique allowed for numerous emitter tips to be made at once, as well as controlling the material porosity during manufacture. One of the benefits of this type of manufacturing was to allow greater thermal stability of the emitters during operation.

2.3 Background of Ferrohydrodynamics

2.3.1 Ferrofluids

A ferrofluid is a superparamagnetic fluid. Superparamagnetism occurs when a ferromagnetic substance such as iron oxide (Fe_2O_3) is in a form of solid nanoparticles where each nanoparticle consists of a single magnetic domain. The thermal energy of these particles is high enough that in an environment where no magnetic field is applied, there is no net magnetization of the particles, but the temperature is below the Curie temperature.

The particles do not interact with each other. The susceptibility and magnetization of a superparamagnetic substance depends on the concentration of superparamagnetic particles.

Paramagnetism, however, occurs when a material, such as a ferromagnetic material like iron oxide, is heated above its Curie temperature. Above the Curie temperature, the thermal energy of the atoms is high enough to cause the magnetic domains to become random, and like the superparamagnetic case, there is no net magnetization when there is no applied magnetic field. However, a paramagnetic material has a lower susceptibility than a ferromagnetic material below its Curie temperature. Because there is no known element with a Curie temperature above its melting temperature, ferrofluids are created using superparamagnetism.

To create ferrofluids small, solid magnetic particles are stably dispersed in a carrier fluid. A ferrofluid is formed when the size of the magnetic particles are in the nanometer range (10^{-7} to 10^{-9} m) and form a stable colloid in the fluid. An illustration of a ferrofluid is provided in Figure 2.5. If the magnetic nanoparticles are small enough, Brownian motion keeps them well dispersed throughout the ferrofluid. As the particles become larger, the nanoparticles can begin to flocculate. To prevent this the magnetic nanoparticles are stabilized either electrostatically or sterically.

When a pool of ferrofluid is subjected to a sufficiently strong magnetic field normal to its surface, the surface deforms into a number of peaks, which is known as the Rosensweig instability, and an example of this is in Figure 2.6.

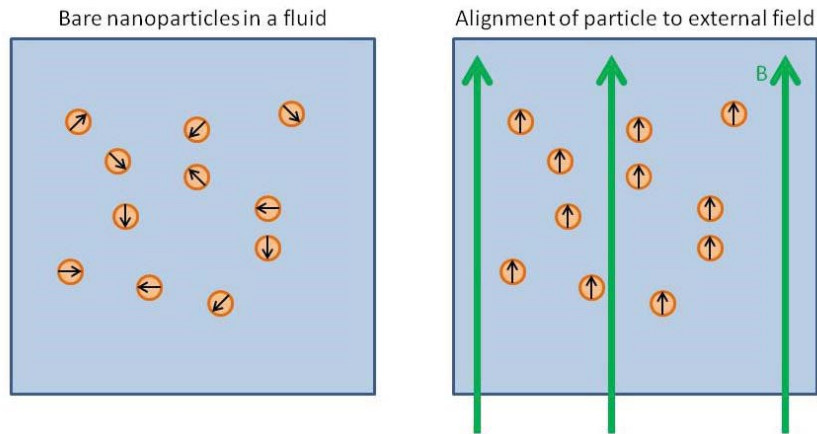


Figure 2.5: Illustration of a ferrofluid. The small spheres are single-domain magnetic nanoparticles such as Fe_2O_3 . Left: With no magnetic field applied, the magnetic nanoparticles are stably dispersed throughout the fluid. Right: Upon the application of a magnetic field, the domains of the magnetic field tend to align with the applied magnetic field. The magnetic nanoparticles stay dispersed in the ferrofluid.

2.3.2 Rosensweig Instabilities

The Rosensweig instability is a ferrohydrodynamic perturbation of a ferrofluid free surface caused by a magnetic field applied normal to the fluid surface in a gravity environment. The Rosensweig instability is the magnetic version of the Taylor instability. Figure 2.7 provides an illustration of the growth of the Rosensweig instability. When a sufficiently strong magnetic field is applied normal to a pool of ferrofluid, any sort of non-uniformity will cause a slight deformation in the fluid surface. This slight deformation focuses the applied magnetic field causing a greater deformation in the fluid surface. This instability would continue to grow, but the surface energy and gravitational energy of the ferrofluid

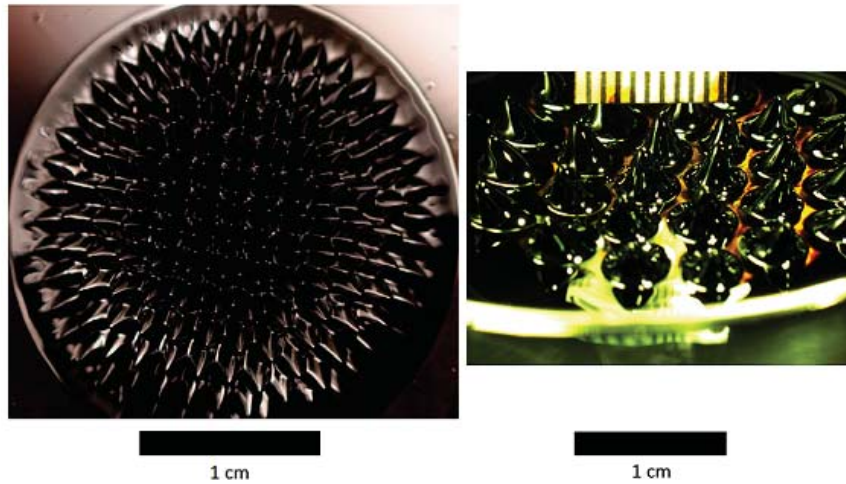


Figure 2.6: A pool of ferrofluid exposed to a sufficiently strong magnetic field normal to its surface. Surface of fluid distorts, this is known as the Rosensweig instability. Left: Top-down view of Rosensweig instabilities. Ferrofluid above a 2.5 cm diameter magnet. Right: Side/Angled view of Rosensweig instabilities. The magnetic field was provided by an electromagnet.

combats this growth. Minimizing the magnetic, surface and gravitational energies yields stable multiple cones, or peaks, of ferrofluid, called Rosensweig instabilities.

A brief overview of the equations that can be used to model the Rosensweig instability is given in Equations 2.15 - 2.19. A full derivation of this work can be found in Ferrohydrodynamics by Rosensweig [23]. First, the fluid is considered incompressible, yielding the conservation of mass

$$\nabla \cdot \vec{v} = 0. \tag{2.15}$$

Navier-Stokes for a magnetic fluid describes the fluid motion

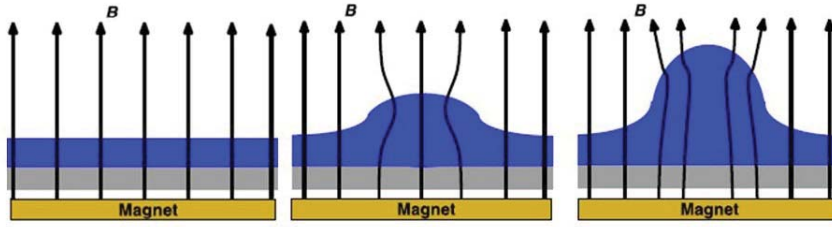


Figure 2.7: A pool of ferrofluid (blue) exposed to a magnetic field. Left: A pool of ferrofluid with no perturbations to the surface. Center: A slight deformation in the fluid surface focus the magnetic field. The ferrofluid is drawn toward the gradient in the magnetic field. Right: Rosensweig instability formed. The growth in the surface was caused by magnetic energy and limited by surface and gravitational energies. The Rosensweig instability is a minimization between magnetic, surface, and gravitational energies. This instability creates multi-tip modal patterns of peaks in the ferrofluid, such as those in Figure 2.6.

$$\rho \left(\frac{\partial \vec{v}}{\partial t} + \vec{v} \cdot \nabla \vec{v} \right) = -\nabla (p + \rho g z). \quad (2.16)$$

The left-hand side of Equation 2.16 is the convective terms, and the right hand side contains the pressure and body forces. The fluid is assumed to inviscid. Gauss's Law

$$\nabla \cdot \vec{B} = 0 \quad (2.17)$$

and Ampere's Law

$$\nabla \times \vec{H} = 0 \quad (2.18)$$

were included, assuming no currents were present. The pressure balance across the fluid-vacuum boundary is

$$p + \frac{1}{2}\mu_0 M_n^2 + \mu_0 \int_0^H M dH - 2\sigma \mathcal{H} = 0. \quad (2.19)$$

The pressure outside of the fluid was assumed to be zero, or a vacuum. In these equations v is the fluid velocity, p is the fluid pressure, ρ is the fluid density, g is the acceleration due to gravity, z is the fluid height, B is the applied magnetic field, H is the auxiliary field, M_n is the component of the magnetization normal to the surface of the fluid, σ is the surface tension of the fluid, \mathcal{H} is the mean curvature of the fluid, and M is the fluid magnetization of the fluid, μ_0 is the permeability of free space, and μ_r is the relative permeability of the fluid.

The applied magnetic field is assumed to be uniform and is applied perpendicular to the unperturbed fluid surface. The shape of the surface is assumed to be of the form of a periodic wave, or

$$z \propto e^{-i(\omega t - k\vec{r})} \quad (2.20)$$

where z is the fluid height, ω is the wave frequency, t is time, q is the wavenumber, and \vec{r} a spatial position. Perturbation theory is then applied to the Equations 2.15 - 2.19, with solutions found for the zeroth order, and the first order equations are then developed. These new terms are then linearized to remove any terms greater than the first order and solved, resulting the dispersion relation

$$\rho \omega^2 = \rho g k + \sigma k^2 - \frac{k^2 \mu_0 M^2}{1 + \frac{1}{\mu_r}}, \quad (2.21)$$

relating wave frequency, ω , wavenumber, k , fluid density, acceleration due to gravity, g , relative permeability, μ_r , and fluid magnetization, M . The critical point, when the Rosensweig instability forms, was found by setting $\omega^2 = 0$ and $\frac{\partial \omega}{\partial k} = 0$. When ω^2 is less than zero, it implies that ω is imaginary. An imaginary ω in Equation 2.20 means the surface amplitude would grow in height. Therefore $\omega^2 = 0$ indicates the verge of when Rosensweig instabilities can form. The criteria of $\frac{\partial \omega}{\partial k} = 0$ indicates the fastest dominant mode, or the fastest growing wavenumber. The wavenumber at this point was found to be the capillary wavenumber

$$k_c = \sqrt{\frac{\rho g}{\sigma}} \quad (2.22)$$

and an example of this spacing is shown in Figure 2.8. The minimum magnetization required to obtain the Rosensweig instability was found to be

$$M_c^2 = \frac{2}{\mu_0} \left(1 + \frac{1}{\mu_r}\right) \sqrt{\rho g \sigma}. \quad (2.23)$$

Any fluid magnetization above this critical value will yield the Rosensweig instability. This value also sets the minimum saturation magnetization of a ferrofluid to exhibit the Rosensweig instability.

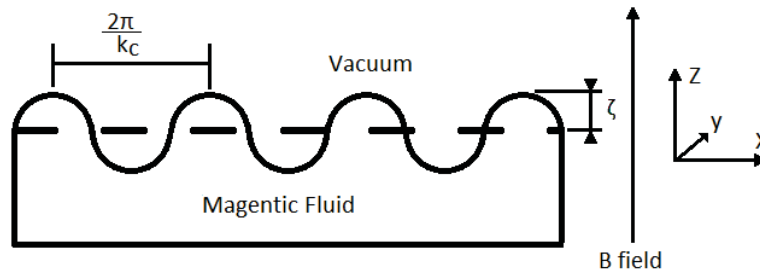


Figure 2.8: Illustration of Rosensweig instability. The critical wavenumber (wavelength) is shown as the spacing between two neighboring peaks.

2.3.3 Rosensweig Instabilities in Uniform and non-Uniform Magnetic Fields

Rosensweig instabilities in uniform applied magnetic fields have been studied in depth, in both experimental [24–40] and theoretical [23,41–52] contexts. However, there have been very few studies that have explored or hypothesized about what results when a ferrofluid is exposed to a “normal” non-uniform magnetic field. It has been observed that ferrofluids in a non-uniform magnetic field do not behave as predicted by all the theory for ferrofluids in uniform magnetic fluids. For example, above in Figure 2.6, theory predicts that the wavelength of the Rosensweig instability should be equal to or greater than the capillary length of the fluid. For the ferrofluid used in that image (FerroTech EFH-1, fluid properties given in Section 2.3.1, Table 5.1), the capillary length is 9.8 mm, however, the measured wavelength was roughly 1.8 mm. To date, the only hypothesized method for accounting for a non-uniform magnetic field was in a dissertation by Rupp [53]. Rupp hypothesized

that the gravity force density term

$$F_{grav} = \rho g \quad (2.24)$$

in the dispersion relation (Equation 2.21), could be replaced by a magnetic force density term, $M\nabla H$. Fixing the units and adjusting nomenclature yields

$$F_{gradient} = \frac{\vec{M} \cdot \nabla \vec{B}_0}{\mu_r}. \quad (2.25)$$

Making this substitution in the dispersion relation, Equation 2.21, goes against the assumption in the derivation that the applied magnetic field is uniform. The derivation of the dispersion relation in Equation 2.21 assumed that the applied magnetic field was uniform. Rupp's substitution can be thought of as applying a much stronger gravity force than is available at the surface of the earth, however this force is due to the Kelvin force, or $M\nabla H$. The gradient of the magnetic field is dominant when the force density due to the gradient is at least an order of magnitude large than the force density due to gravity, or when

$$\frac{F_{gradient}}{F_{grav}} = \frac{\vec{M} \cdot \nabla \vec{B}_0}{\rho g} \quad (2.26)$$

is greater than or equal to 10. This has been observed in the laboratory because small volumes of ferrofluid near a magnet have been turned "upside down," and the instability shape does not change, nor does the ferrofluid fall to the floor. Using Rupp's hypothesized substitution, the peak-to-peak spacing of the Rosensweig instability should be set by

$$\lambda = 2\pi\sqrt{\frac{\sigma}{M\nabla B_0}}. \quad (2.27)$$

More recently a paper by Timonen et al has been published that determined the array spacing of ferrofluid drops on a superhydrophobic surface for various non-uniform magnetic fields [54]. The work by Timonen et al studied a different phenomenon than the work by Rupp. Rupp's work proposed the basis regarding how an interconnected ferrofluid would behave in a non-uniform magnetic field. Timonen et al studied the effect a non-uniform magnetic field had on the structure of individual magnetic entities. The array spacing of ferrofluid drops developed by Timomen et al is presented in this work because it is unknown if interconnected Rosensweig instabilities behave the same way as individual Rosensweig instabilities in a non-uniform magnetic field regarding the spacing to their nearest neighbors.

The analysis by Timonen et al minimized the dipole-dipole energy between individual fluid drops and the magnetic dipole energy of each fluid drop in a non-uniform magnetic field. The first part of the analysis by Timonen et al claimed and observed that if a discrete droplet was wider than the critical wavelength

$$\lambda_c = 2\pi\sqrt{\frac{\sigma}{\frac{d}{dz}(\mu_0MH)}} \quad (2.28)$$

it would break into two discrete droplets. Interestingly this was the same equation proposed by Rupp believing it to be the spacing of Rosensweig instability peaks in a non-uniform

magnetic field. The work by Timonen et al then went on to analyse the droplet-to-droplet spacing. They did this by starting with a single droplet on the superhydrophobic surface in a non-uniform magnetic field. As they increased the applied non-uniform magnetic strength, the number of discrete droplets increased. In their tests, they had a maximum of 19-21 droplets formed. They would then decrease the strength of the applied non-uniform magnetic field. Because the drops of ferrofluid were not connected, the number of drops remained constant, while the drop-to-drop spacing increased. To analyse this, they compared the dipole-dipole energy per volume against the magnetic moment energy per volume for each drop where the total energy is

$$u = \frac{\mu_0}{4\pi} \sum_{i=1}^N \sum_{j=i+1}^N \frac{m_i m_j}{|\vec{r}_i - \vec{r}_j|^3} - \mu_0 \sum_{i=1}^N m_i \left(H + \frac{1}{2} \frac{d^2 H}{dr^2} |\vec{r}_i|^2 \right), \quad (2.29)$$

The energy per volume is u , m is the magnetic moment of a drop, and \vec{r} is the position of the droplet. This analysis assumed that each droplet of ferrofluid acted as a large-scale magnetic moment that would repel another droplet. The magnetic moment energy is defined as $u = \mu_0 m H$. Timonen et al took a Taylor expansion of the magnetic field in the radial direction about the center of a magnet. This Taylor expansion about the magnet centerline is

$$H = H + \frac{dH}{dr} r + \frac{1}{2} \frac{d^2 H}{dr^2} r^2 + H.O.T. \quad (2.30)$$

At the centerline of the magnet there is symmetry in the strength of the axillary magnetic field, therefore the first order term disappears. The terms higher than the second order

are ignored, and Timonen et al were left with a zeroth and a second order term. Timonen et al call the second derivative of the auxiliary field the magnetic curvature and define $c = -\frac{d^2H}{dr^2}$. Solving for the minimum energy, and ignoring the coefficients from the summations yields

$$a \propto \left(\frac{m}{c}\right)^{\frac{1}{5}}, \quad (2.31)$$

or an expression relating the lattice spacing, a to the magnetic moment and curvature of the magnetic field.

With Rupp's hypothesized force method, the knowledge required to predict peak-to-peak spacing is the fluid properties (surface tension, magnetic saturation, and relative permeability) and the applied magnetic field. With the method used by Timonen et al, the above knowledge is required, along with the volume of the fluid peaks, because the magnetic moment is related to the magnetization by the fluid volume, $m = MV$, where V is the volume of each droplet or peak.

2.4 Analysis of fluid Energies

In magnetic materials, the auxiliary field in a medium is dependent upon the externally applied field, but also the geometry of the medium. This geometry based term is called a demagnetization factor. Polar and conductive materials have a similar term called

the depolarization factor. These two ideas are combined with the energy equations for Rosensweig instabilities with an applied electric field, assuming the fluid used was both conductive and a ferrofluid.

2.4.1 Energy balances of Rosensweig Instabilities

Rosensweig instabilities have three competing energy sources, gravitational energy, U_g , surface energy, U_s , and magnetic energy, U_m . Gravitational energy

$$U_g = \frac{1}{2} \rho g \int \int z^2(x,y) dx dy \quad (2.32)$$

and surface energy

$$U_s = \sigma \int \int \left[1 + \left(\frac{\partial z}{\partial x} \right)^2 + \left(\frac{\partial z}{\partial y} \right)^2 \right]^{1/2} dx dy \quad (2.33)$$

energy both increase as the surface deforms from a flat pool, assuming a constant volume of fluid. In the most general form, the magnetic energy is written as

$$U_m = \int \int \int \int H dB dx dy dz. \quad (2.34)$$

Assuming the relationship between B and H is linear, it can be transformed in a more informative form

$$U_m = -\frac{1}{2} \int \int \int \mu_0 M H_0 dx dy dz + \frac{1}{2} \int \int \int \mu_0 H_0^2 dx dy dz, \quad (2.35)$$

where H_0 is the undisturbed applied auxiliary field. The rightmost triple integral of Equation 2.35 does not vary with the deformation of the ferrofluid; it is the energy added by the background magnetic field. The left triple integral of Equation 2.35 is the reduction of energy due to the presence of a magnetic fluid.

2.4.2 Energy of a magnetic drop in a magnetic fields

If a free drop of magnetic fluid is exposed to a uniform magnetic field, the drop of fluid will elongate into a prolate shape [55–59]. The two competing forces in this scenario are the magnetic traction pressure and the force due to the surface tension; a sketch of the system and force balance is given in Figure 2.9. The applied magnetic field magnetizes the fluid drop. The fluid magnetization creates an outward stress on the fluid in the direction of the applied magnetic field, and in the direction opposing the applied magnetic field. The fluid surface tension counteracts the magnetic stress. In order to maintain stress equilibrium at the fluid interface, the fluid deforms into a prolate spheroid. This prolate spheroid increases the surface stress by decreasing the local radius so that the surface tension stress matches the magnetic stress.

Re-writing Gauss's law for magnetism by substituting $\mu_0 (H + M)$ for B , results in

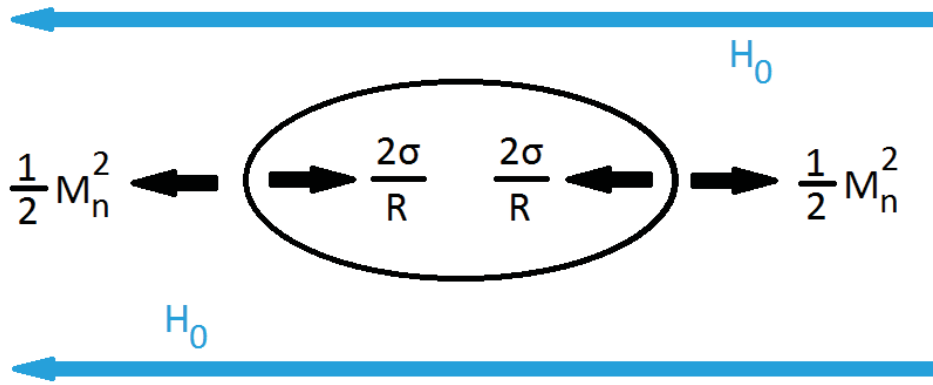


Figure 2.9: Force balance for a magnetic drop in a uniformly applied magnetic field.

$$\nabla \cdot \vec{H} = -\nabla \cdot \vec{M}. \quad (2.36)$$

This means that when there is a distinct change in magnetization, such as the interface between a magnetized ferrofluid and vacuum, an auxiliary field is generated in the opposite direction of the applied auxiliary field. This concept is sketched in Figure 2.10. The strength of the opposing auxiliary field, also known as demagnetizing field, H_d , is dependant upon the magnetization and a geometric factor, N , called the demagnetization factor, which can range between 0 and 1 [60]. The auxiliary magnetic field inside a magnetic material, H , is orientation/geometry dependent and is expressed by

$$H = H_0 + H_d = H_0 - NM. \quad (2.37)$$

Equation 2.37 can be re-written to relate the applied auxiliary magnetic field to the magnetization using the constitutive relation $M = (\mu_r - 1)H$, resulting in

$$M = \frac{(\mu_r - 1)}{1 + N(\mu_r - 1)} H_0. \quad (2.38)$$

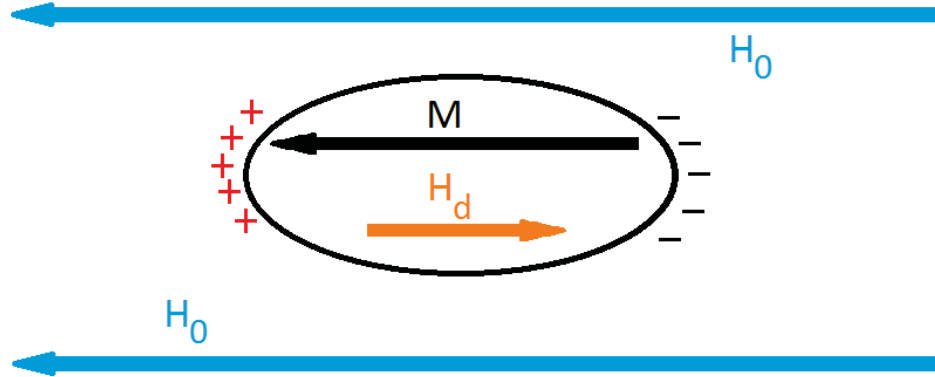


Figure 2.10: Magnetic drop in an externally applied magnetic field, H_0 . Drop is magnetized, M , causing “surface poles” leading to a demagnetizing field, H_d .

A thin slab of magnetic material, magnetized through the thickness has a demagnetization factor of 1 while a thin long rod has a demagnetization factor of 0 when magnetized through the length of the rod, and 1/2 when magnetized normal to the axis of the rod. A perfect sphere has a demagnetization factor of 1/3 from all orientations. From this, the demagnetization of a sphere deforming into a prolate ellipsoid trends from 1/3 to 0 as the drop elongates.

This all means that the magnetic energy stressing a fluid surface depends on the applied auxiliary magnetic field, relative permeability of the fluid, and the shape of the fluid. If the applied auxiliary magnetic field stayed constant at 1 A/m, and the fluid relative permeability was 4. A sphere ($N = 1/3$) would have a volumetric magnetic energy of $-1.5 \text{ A}^2/\text{m}^2$,

according to the first term in Equation 2.35. However, if the shape were changed to be a long thin rod orientated along the magnetic field lines ($N = 0$) the volumetric magnetic energy would be $-3.0 A^2/m^2$, using the first term of Equation 2.35. By only adjusting the shape of the fluid, the magnetic energy was able to greatly increase.

2.4.3 Energy of a conductive and/or polar drop in an electric field

A free drop of polar fluid exposed to a uniform electric field is analogous to a drop of magnetic fluid in a uniform magnetic field. The polar fluid drop in a uniform electric field will elongate into a prolate spheroid shape. The shape is determined by the electrical stress, $\frac{1}{2}\epsilon_0 E^2$, and the surface tension stress, $\frac{2\sigma}{R}$, into equilibrium. As the applied electric field increases, the radius of the spheroid along the electric field must reduce to equate the two stresses.

In a polar drop, the ‘N’ term is called depolarization instead of demagnetization, but the quantity is the same in both cases, a geometric factor describing how much of a depolarizing (demagnetizing) field is generated internal to the fluid drop. The electric field internal to the fluid, E , is a function of the applied electric field, E_0 , and the depolarization field, E_d ,

$$\epsilon_0 E = \epsilon_0 E_0 + \epsilon_0 E_d = \epsilon_0 E_0 - NP. \quad (2.39)$$

The depolarization field is defined as $\epsilon_0 E_d = -NP$ where P is the polarization of the fluid. Equation 2.39 can be rewritten using the constitutive relation $P = \epsilon_0 (\epsilon_r - 1) E$, resulting in

$$P = \epsilon_0 \frac{(\epsilon_r - 1)}{1 + N(\epsilon_r - 1)} E_0. \quad (2.40)$$

If we are to extend this analysis to a conductive fluid, such as an ionic liquid, the analysis needs a modification. In a perfectly conductive fluid, there is no internal electric field,

$$0 = \epsilon_0 E_0 + \epsilon_0 E_d = \epsilon_0 E_0 - NP. \quad (2.41)$$

Re-arranging Equation 2.41, results in

$$P = \frac{\epsilon_0}{N} E_0. \quad (2.42)$$

This is an interesting result because it appears that as a conductive drop in an electric field elongates the depolarization factor, N trends toward 0, resulting in the polarization tending toward infinity.

A similar conclusion can be reached with a conductive droplet of fluid in an electric field as above in Section 2.4.1 with a magnetic fluid. The energy of a droplet of conductive fluid could be stressed by a means other than an electric field, a change in the fluid drop shape causes a change in the fluid drop's electrical energy, for the same applied electric field and fluid properties.

2.4.4 Energy balance of an ILFF in combined magnetic and electric fields

For an applied magnetic field that is strong enough to form Rosensweig instabilities, the energy balance of an ILFF exposed to combined magnetic and electric fields summation of the energies from the Rosensweig instability and the energy from the electric field which is

$$U_e = -\frac{1}{2} \int \int \int P E_0 dx dy dz + \frac{1}{2} \int \int \int \epsilon_0 E_0^2 dx dy dz. \quad (2.43)$$

The pertinent part of the energy terms is change in energy of the fluid, and not the vacuum energy. This means the last terms in the magnetic energy (Equation 2.35) and electrical energy (Equation 2.43) can be ignored. Combining these energy terms with that of the gravitational energy (Equation 2.32) and surface energy (Equation 2.33) yield

$$U = U_g + U_s - \frac{1}{2} \int \int \int \mu_0 M H_0 dx dy dz - \frac{1}{2} \int \int \int P E_0 dx dy dz. \quad (2.44)$$

The peaks formed by the Rosensweig instability behave similarly to that of a suspended drop of fluid described in the sections above (Sections 2.4.2 & 2.4.3). In a uniformly applied magnetic field, as the strength of the magnetic field is increased, the Rosensweig instabilities grow in height, reducing the demagnetization factor. The fluid shape deformation can be viewed in Figure 2.11. We can replace the magnetization and polarization in Equation 2.44 with the values determined above in Equations 2.38 & 2.42,

respectively, yielding

$$U = U_g + U_s - \frac{1}{2} \int \int \int \mu_0 \frac{(\mu_r - 1)}{1 + N(\mu_r - 1)} H_0^2 dx dy dz - \frac{1}{2} \int \int \int \frac{\epsilon_0}{N} E_0^2 dx dy dz. \quad (2.45)$$

What is important about Equation 2.45 is that the peaks that are already formed will grow in height when there is an increase in the applied magnetic or electric field. If, for instance, the electric field is increased, the peak grows in height. Because the geometry of the peak has changed (grown taller), the demagnetization/depolarization factor, N , has decreased. Because N has decreased, the same applied magnetic field is more effective and helps contribute to the growth in peak height.

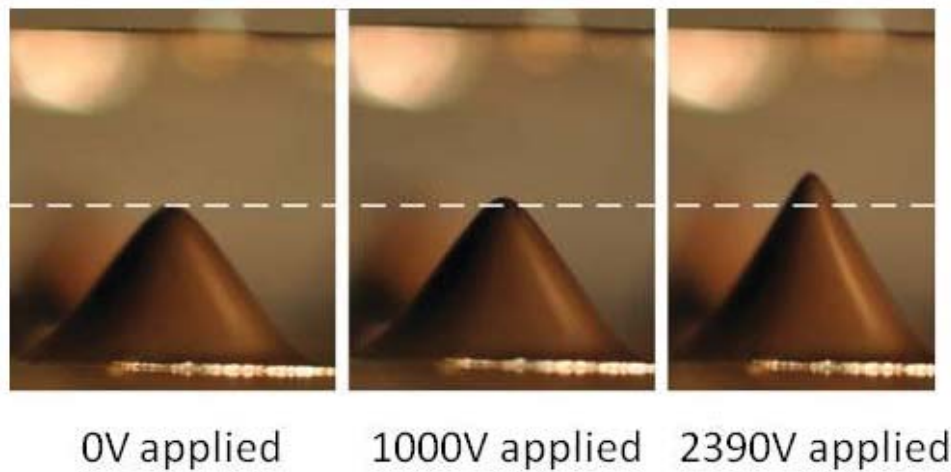


Figure 2.11: Deformation of a conductive magnetic fluid. Left: Only a magnetic field applied. Middle: Magnetic field and moderate electric field applied. The fluid grew in height. Right: Magnetic field and stronger electric field applied. Much more noticeable increase in fluid height. Demagnification/Depolarization factor changing as the fluid shape changes.

An example of this would be if a magnetic field, but no electric field was applied to

the ILFF and Rosensweig instabilities formed. At this point let the demagnetization factor/depolarization factor, based on geometry, be equal to $N = 0.30$. From this value of N and the applied auxiliary field, the magnetic energy term yields -100 energy units. At this point, energy contributions from the gravity term and surface tension term add up to +100 energy unit and there is 0 energy from the electric energy. Say that an electric field was then applied, which changed the demagnetization/depolarization factor to $N = 0.25$. The resulting energy from the applied electric field, with this new N was -50 energy units. Even though the applied auxiliary field remain constant, the magnetic energy contribution changed due to the change in N . The magnetic energy may now be -115 energy units. This would mean the gravitational and surface energies would have to increase by 65 energy units instead of only the 50 energy units added by the addition of the electric field.

This could have a practical benefit for electro spraying. When an electric field is applied to an ILFF with Rosensweig instabilities, the ILFF peaks deform more than they would from just the energy due to the applied electric field. This may yield lower onset voltage for electro spray sources compared to those predicted by Equation 2.9.

Chapter 3

Proof-of-Concept Experiments

3.1 Introduction

The motivation of this work was to create an alternate fabrication technique which could create a regular array of electrospray emission sources without the drawbacks of conventional fabrication. This chapter details the efforts that were made to first develop an electrospray source where the emission sites were created using electrohydrodynamic instabilities. After failing to obtain stable electrospray using electrohydrodynamic instabilities, this early attempts to create electrostatic arrays of cones gave way to studies with ferrofluids.¹ After numerous failed attempts to create an ionic liquid ferrofluid in I_{SP} laboratory, we began contacting the University of Sydney replicating their work. This

later led to a collaboration with the University of Sydney. After obtaining an ILFF, it was studied to determine if electric fields could distort Rosensweig instabilities, thus having the potential to be used as the basis for an electrospray source.

3.2 Electrostatic formation of peaks for electrospray

The first investigation perused to develop a self-assembling electrospray source was utilizing electrohydrodynamic instabilities in a pool of conductive fluid. These types of electrohydrodynamic (EHD) instabilities have been observed and reported [61–75] as well as numerous EHD models [76–80].

Electrohydrodynamic instabilities occur when a uniform electric field greater than a critical value is applied to a conductive fluid. This instability causes fluid peaks to grow in the fluid. The electrostatic hydrodynamic instability was analogous to the Rosensweig instability presented in Section 2.3.2.

Electrohydrodynamic instabilities have been investigated to create liquid metal ion sources for space propulsion, nuclear fusion work, and metallic film deposition. [72,77,81–86] The nuclear fusion segment of this work would have been used over a large surface area and

¹During a discussion in early 2012 after a failed attempt to obtain a stable electrospray source using electrohydrodynamic instabilities, a fellow lab-mate, Mark Hopkins proposed we try using ferrofluids to create arrays of peaks in a fluid. That piece of advice paved the way for the rest of the work presented in this dissertation.

been transitory. They would not have had to worry about shorting out between their ion sources and an extraction electrode. The liquid metal ion source for thrusters used linear arrays instabilities, confining the growth location of cones to help prevent shorting out of the liquid metal to the extraction electrode. These sources lost research interest because they were not thought feasible to use because they required high temperatures to operate, hazardous propellants and high voltages to operate. Electrospary utilizing EHD instabilities was investigated at MTU because the advent of ionic liquids solved many of these issues. Ionic liquids were liquid at room temperature, and most are not very harmful. Ionic liquid surface tension is about an order of magnitude lower than a liquid metal, meaning it would require a lower operating voltage to cause electrospary.

These benefits of ionic liquids led to the investigation of utilizing EHD instabilities to create self-assembling arrays of electrospary sources was attempted in the I_{SP} at MTU. The experiments always ended with temporary peaks being formed in a pool of fluid and either arcing through vacuum, or the peak would grow unstably and bridge the gap between the upper and lower electrodes. Numerous fluids, such as the ionic liquid 1-ethyl-3-methylimidazolium tetrafluoroborate (EMIM-BF₄), eutectic indium-gallium, and mercury were used in an attempt to create stable EHD instabilities in the fluid, but all trials ended with arcing and no stable peaks formed. It was later discovered in a publication by Néron de Surgy, Chabrierie, and Wesfreid that they too were not able to get stable peaks to form, but only transient peaks that would arc between their two electrodes [74].

3.3 Ionic Liquid Ferrofluids and their Synthesis

The next task was to prepare a ferrofluid with suitable properties for electrospray. There are two properties that are desirable for an electrospray source to operate in a vacuum. The first is no measurable vapor pressure. The second is a fluid that is conductive or strongly polar. The majority of all ferrofluids available prior to this work used a base fluid of water, oil, or kerosene. None of the existing ferrofluids had qualities of being conductive little to no vapor pressure. The goal was to then create an ionic liquid ferrofluid. Many ionic liquids, such as EMIM-BF₄, have little to no measurable vapor pressure and are conductive. The *ISP* began attempting to make an ionic liquid ferrofluid (ILFF) but with no success. The lab then found two publications by Jain et al that had recently been published on how they had created the first true ILFFs [87, 88].

3.4 Collaboration with University of Sydney and the fabrication of ionic liquid ferrofluids

Hawlett's group at the University of Sydney provided numerous samples of ionic liquid ferrofluids (ILFF). The three batches of ILFF and the ILFF properties that were used in the testing presented in this dissertation are provided in Table 3.1.

Table 3.1
Comparison of ILFFs

Base Ionic Liquid	EAN	EAN	EMIM-NTf2
Surfactant	Yes	Yes	Yes
Magnetic nanoparticles	Fe_2O_3	Sirtex	Sirtex
Protic/Aprotic	Protic	Protic	Aprotic
Hydrophobic/Hydrophilic	Hydrophilic	Hydrophilic	Hydrophobic
Viscosity (Pa-s)	very viscous	very viscous	~ 0.030
Creates peaks at room temperature	No	Yes	Yes
Thermal Stability	$\sim 200^\circ\text{C}$	$\sim 200^\circ\text{C}$	$\sim 350^\circ\text{C}$
Fraction Magnetic nanoparticles (w/w)	41%	35%	22%
Fraction Surfactant (w/w)	unk	unk	3%
Magnetic Saturation ($\frac{kA}{m}$)	unk	unk	23.9
Relative Permeability	unk	unk	11
Density ($\frac{kg}{m^3}$)	unk	unk	1840
Surface Tension ($\frac{N}{m}$)	unk	unk	0.0363
Conductivity ($\frac{S}{m}$)	unk	unk	0.6
Batch Number	NJ332106	NJ397007	NJ397028

Jain, a member of Hawkett's group created three batches of ILFF that were used in testing reported in this dissertation. The first two ILFFs were Ethylammonium Nitrate (EAN)-based, batch number NJ332106 and NJ397007. EAN is a hydrophilic ionic liquid and has an affinity to absorb water. To help combat this, the vials of ILFF were kept in a desiccator, however, the humidity in the desiccator would commonly be over 25% relative humidity in the summer, so the ILFF would have to be degassed in a vacuum chamber before it could be used in electro spray emission testing. Batch NJ332106 was the first batch of ILFF used for testing at Michigan Tech. At room temperature this ILFF behaved as a gel and needed to be heated before it would flow and show the Rosensweig spikes in a magnetic field. Batch # NJ332106 was only used for initial testing described in Section 3.5. Batch NJ397007 was also EAN-based, and was modified based of off ILFFs they had

previously manufactured. It was prepared with 71 nm Sirtex magnetic nanoparticles and contains 22% polymer by weight. It was reported to be free flowing above 45°C. This ILFF was very viscous at room temperature and behaved much like molasses. This batch of ILFF was used in some initial electrospray testing as well as used during quadrupole mass spectrometer testing at Kirtland AFB, as well as Experiment 1 in Chapter 4, Section 4.3.

A third ILFF was developed for the purpose of obtaining electrospray in a vacuum environment. This ILFF had a base fluid of 1-Ethyl-3-methylimidazolium bis(trifluoromethylsulfonyl)imide (EMIM-NTf₂), batch number NJ397028. EMIM-NTf₂ is a hydrophobic ionic liquid. It was prepared using Sirtex magnetic nanoparticles comprised of Fe₂O₃. By weight, the ILFF contains 3% polymer and 22% Fe₂O₃. The electrical conductivity of the EMIM-NTf₂-based ILFF was measured using a LAQUA Twin EC Meter by Spectrum Technologies. The conductivity at 22.4°C (295.55K) was measured to be 0.63 S·m⁻¹. This conductivity was found to be roughly 25% lower than that of EMIM-NTf₂, as reported by Widegren et al [89]. The viscosity of a new batch of EMIM-NTf₂ based ILFF (batch number NJ397047) with an identical fabrication procedure to NJ397028 was found to match the viscosity values for pure EMIM-NTf₂ in literature of roughly 0.030 Pa·s at room temperature [90]. A synopsis of the ILFFs used and their distinctive properties is given in Table 3.1. The surface tension of batch number NJ397028 was measured by Ebatco using a Kyowna Contact Angle Meter Model DM-701 and found to be 0.0363N/m at room temperature (22°C).

Ionic liquid ferrofluid development has unknowns, such as what are desired ranges of fluid properties? Some of the known desired properties are low to no vapor pressure, and low surface tension. A reduction in surface tension lowers the onset voltage to obtain electrospray, Equation 2.9, and increases the packing density of the ILFF, Equations 2.22 & 2.27. The optimal ranges of conductivity and viscosity are currently unknown, and would require further investigation to determine. One quantity that can be bounded is the concentration of magnetic nanoparticles. Equation 2.23 provided the minimum required magnetization required to obtain the Rosensweig instability. Using the minimum magnetization as the saturation magnetization, the minimum concentration of magnetic nanoparticles can be determined. The saturation magnetization of the fluid is given by

$$M_{sat,fluid} = nM_{sat,Fe_2O_3} \quad (3.1)$$

where n is the magnetic nanoparticle concentration (v/v) in the fluid and M_{sat,Fe_2O_3} is the saturation magnetization of the Fe_2O_3 magnetic nanoparticles. Combining Equations 2.23 & 3.1 and solving for the concentration yields

$$n = \frac{1}{M_{sat,Fe_2O_3}} \sqrt{\frac{2}{\mu_0} \left(1 + \frac{1}{\mu_r}\right) \sqrt{\rho g \sigma}}. \quad (3.2)$$

This equation provides the lower bound on concentration of magnetic nanoparticles in an ILFF to create the Rosensweig instability.

3.5 Proof-of-concept experimental results: Deformation of Rosensweig Instability in an Electric Field

Ionic liquid ferrofluids were first created about a year before researchers in the *ISP* lab began to use the ILFF in combined magnetic and electric fields. Because this material with magnetic and electric properties had not previously existed, there did not exist any literature detailing combined electric and magnetic stresses on a conductive magnetic fluid. This led to proof-of-concept experiments to determine if Rosensweig instabilities in a ILFF could be deformed when an electric field was applied with a magnetic field.

The ILFF used for this work was the first batch of EAN created (batch # NJ332106). The ILFF was placed in a stainless steel fluid holder (see left of Figure 3.1) with a pocket 15.24 mm by 15.24 mm and 2.54 mm deep (0.6 in by 0.6 in and 0.1 in deep). A counter electrode was placed above the pool of fluid. This apparatus was placed into the Helmholtz coil. An illustration of this setup can be seen in the right of Figure 3.1. The leftmost image of Figure 3.2 shows the initial state of the fluid with no magnetic or electric fields applied. Increasing the current applied to the Helmholtz coil increased the applied magnetic field to the fluid. At 7 A of applied current (an auxiliary field of 23.6 kA/m), the Rosensweig instabilities on the fluid surface were as shown in the middle image of Figure 3.2. Maintaining a constant magnetic field, the ILFF pool was biased negatively

versus the grounded counter electrode. As the magnitude of the applied voltage increased, the height of the peaks increased, and the radius of curvature of the tips decreased. This sequence can be viewed in Appendix C. The highest applied voltage to the system was -6,000 V (with an auxiliary field of 23.6 kA/m), and this can be viewed in the rightmost image of Figure 3.2. This initial test showed that Rosensweig instabilities in an ILFF can in fact be deformed with an applied electric field. The next step was to show that using this technique and ILFF can emit ions and/or droplets, and this work is presented in Chapter 4.

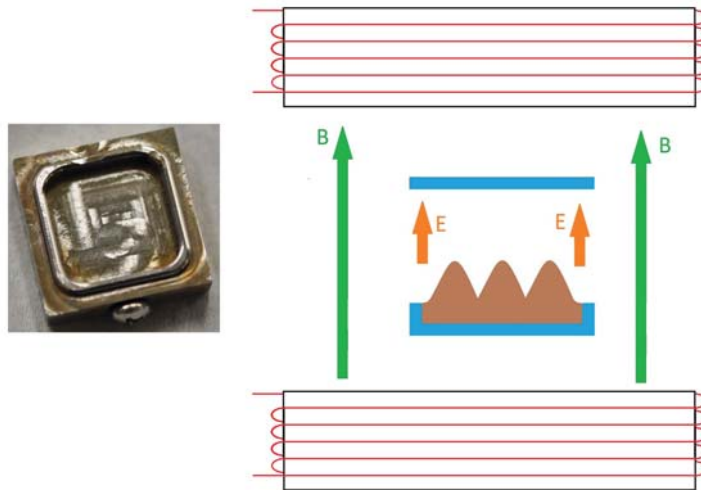


Figure 3.1: Left: Stainless steel fluid holder. Pocket is 15.24 mm by 15.24 mm and 2.54 mm deep (0.6 in by 0.6 in and 0.1 in deep), radius of curvature in the pocket is 3.175 mm (0.125 in). The radius of the ridge is 0.635 mm (0.025 in). Right: Illustration of the schematic used to test the deformation of Rosensweig instabilities in combined magnetic and electric fields. Two electromagnets, drawn in red, in a Helmholtz configuration provided a uniform magnetic field to the ILFF (brown peaks). A blue fluid holder and blue counter electrode provided a potential difference between the ILFF and the counter electrode. The Helmholtz coil was built at MTU with each coil containing 250 wraps of 16 AWG magnet wire. The coil centers were 57.2 mm (2.25 in) apart and the inner diameter of the electromagnet coils was 133.4 mm (5.25 in). Each electromagnet coil was 25.4 mm (1.00 in) wide.

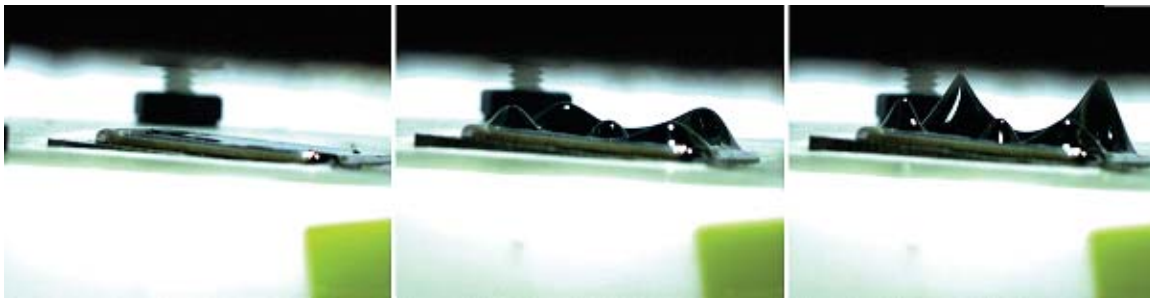


Figure 3.2: EAN based ILFF (batch # NJ332106). Left: No magnetic or electric field applied ($H = 0$ kA/m, $V = 0$ V). ILFF surface is flat and has no deformations. Middle: Only magnetic field applied ($H = 23.6$ kA/m, $V = 0$ V). ILFF surface deformed, Rosensweig instabilities appear on the fluid surface. Right: Magnetic and electric fields applied ($H = 23.6$ kA/m, $V = -6,000$ V). ILFF surface further deformed by the electric stress. Rosensweig instabilities grow in height and tips have a smaller radius of curvature.

Chapter 4

Electrospray of an ionic liquid ferrofluid utilizing the Rosensweig instability

4.1 Introduction

A magnetic fluid exposed to a magnetic field applied normal to the fluid surface exhibits a stationary instability of arrays of peaks. In proof-of-concept experiments leading up to the work presented in this chapter, it was found that Rosensweig instabilities formed in a conductive ferrofluid could be deformed by an electric field, as described in Section 3.5. The goals of this chapter are to 1) demonstrate that an electric field can cause ion and/or droplet emission from the Rosensweig instability peaks in an ionic liquid ferrofluid (ILFF),

2) measure the current-voltage (I-V) characteristics of an array of peaks of ILFF emitting ions/droplets, and 3) measure voltage required to obtain emission (onset voltage) and compare to the traditional theory for electrospray devices. This chapter starts by presenting the equipment and techniques used to collect data. Next is a chronological reporting on the various experiments performed and the results and any significant observations made during testing. This chapter ends with a discussion on the results obtained in this chapter.

4.2 Equipment and Testing Methodologies

An electrospray source was created and a description of this source is given in Section 4.2.1. The equipment used to detect the current of the emitted spray is described in Section 4.2.2. This is followed by a description of the power supply used to bias the ILFF and cause ion/droplet emission in Section 4.2.3. The ILFF with the electrospray source were placed into a vacuum chamber to simulate a space environment. The vacuum chamber is described in Section 4.2.4. The third goal of the work presented in this chapter was to compare the measured onset voltage to the theoretical onset voltage. In order to make this comparison, three pieces of information were required 1) surface tension of the fluid, 2) the radius of curvature of the tip of the ILFF peak, and 3) the distance between the tip of the ILFF peak and the extraction electrode. The surface tension of the ILFF used in this experiment was given in Table 3.1. The tip radius and the tip-to-extraction electrode distance needed to be measured in situ. These parameters were measured by imaging the

ILFF peaks in the electrospray setup in the vacuum chamber. The camera equipment used for this task is described in Section 4.2.5. To achieve the goals set forth at the beginning of this chapter, three discreet experiments were conducted. The details of these experiment can be read in Section 4.2.6.

4.2.1 Electrospray Source

A fixture was designed to contain an ILFF, apply magnetic and electric fields to the ILFF, detect when emission was occurring, and allow visual access to the ILFF. This fixture is shown in Figure 4.1. The base of the fixture was a 12.7 mm thick teflon block used for mounting and electrical isolation. This teflon block supported the fluid holder, an aluminum block with dimensions of 21.6 mm by 21.6 mm by 6.4 mm. A 4-40 hole was drilled and tapped into the side of the fluid holder to allow the power supply to be connected to it. To hold the ILFF, an annular trench was milled into the aluminum fluid holder. This trench had a radius (to the center of the trench) of 8 mm, the trench was 2 mm wide and 2 mm deep. An image of the fluid holder can be seen in left of Figure 4.2. An extraction electrode was fabricated out of 1.1 mm thick aluminum sheet. The extraction electrode also had an annular pattern broken by three support spokes milled into it. This annular pattern was positioned above the trench in the aluminum fluid holder, and allowed emitted spray of ILLF to pass through the extraction electrode to a downstream current collector. The spacing between the aluminum fluid holder and the extraction electrode was 4.7 mm and

was supported by three nylon threaded rods. The current collector was spaced 1.1 mm above the extraction electrode using a teflon sheet as a spacer between it and the extraction electrode to provide electrical isolation. The current collector is described in more detail in Section 4.2.2. Ionic liquid ferrofluid was added into the trench of the aluminum fluid holder until the trench was full, as can be seen in the right image of Figure 4.2. The ILFF is described in detail in Section 3.4. To create the array of 5 peaks in the ILFF a series of three 25.4-mm-diameter by 3.2-mm-thick grade N52 Neodymium magnets were placed 10.6 mm below the teflon block. The magnets were aligned to be coaxial with the annular trench of ILFF. The measured magnetic field at the location where the surface of the ILFF would be located was 300 G. An image of the entire test fixture can be viewed in Figure 4.3. Electrically, the extraction electrode was grounded to the vacuum chamber and acted as the reference ground for the system. The power supply, described in Section 4.2.3, was grounded to the extraction electrode and biased the aluminum fluid holder either above or below ground to achieve positive or negative ion/droplet emission. To measure the current, the ammeter was referenced to the extraction electrode, and measured the current collected on the current collector, described in Section 4.2.2.

4.2.2 Current Measurement

The current collector was 25 mm by 25 mm by 1.1 mm thick glass sheet coated with indium-tin-oxide (ITO). The ITO coating was conductive with 4-8 ohms of resistance

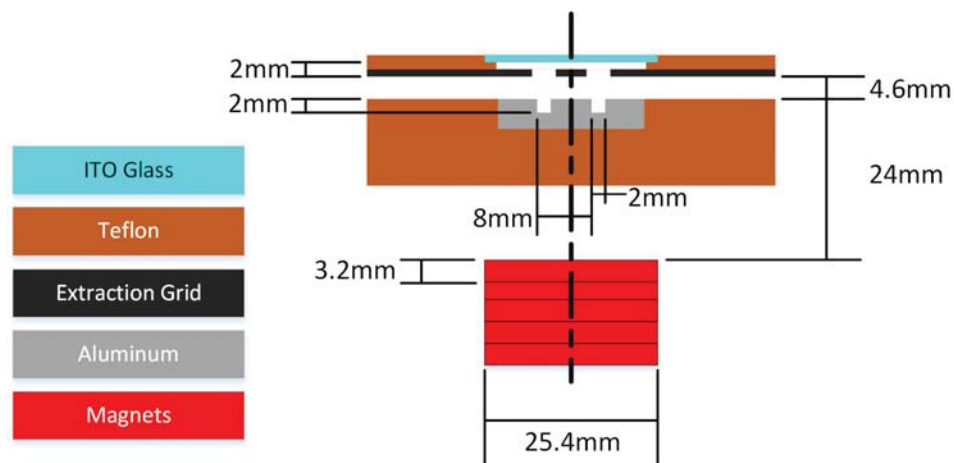


Figure 4.1: Illustration of the cross-section of the electrospray source setup.



Figure 4.2: Image of aluminum fluid holder. Left: Without ILFF. Right: Trench filled with ILFF.

across the ITO surface. The ITO coating was transparent, along with the float glass substrate. The ITO coated glass was purchased from Delta Technologies (part number CG-40IN-0115). The current was measured using a Keithley 2410 sourcemeter. The sourcemeter was referenced to the extraction electrode, and the current collector was allowed to float. The sourcemeter was controlled over GPIB by a LabView program which would record the measured current at a rate of 2 Hz.

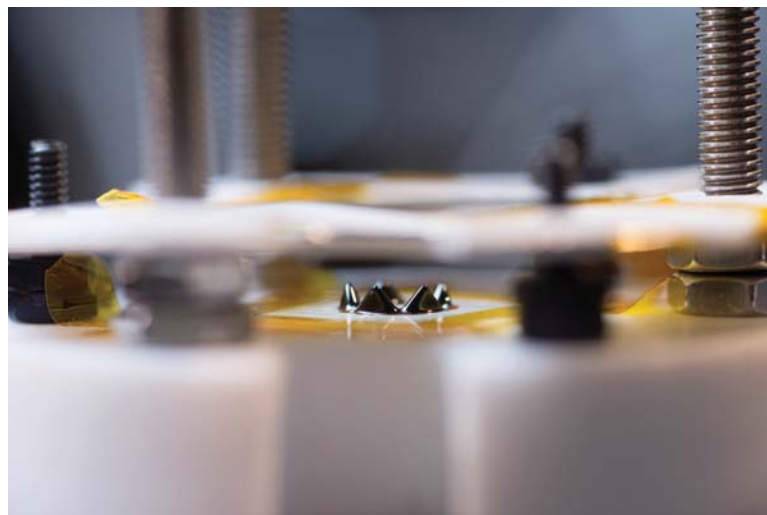


Figure 4.3: Image of the experimental setup (Photo Credit: Sarah Bird).
Letter of permission to use photo in Appendix F.

4.2.3 Power Supplies

Two different power supplies were used to apply voltage to the aluminum fluid holder, and thus the ILFF. A Glassman FX +25 kV power supply was electrically connected to the aluminum fluid holder to allow the emission of positive spray from the ILFF. To cause negative spray to be emitted from the ILFF, a Glassman FC -10 kV power supply was connected to the aluminum fluid holder. Both power supplies were grounded to the extraction electrode. Each of these power supplies had a remote voltage monitor that was used by a LabView program to record the applied voltage.

The 25 kV version of the Glassman power supply has a stated ripple less than 0.02% of the rated voltage, or less than 5 Vrms. The static voltage regulation was specified to be 0.005%

+ 0.5 mV/mA. The maximum currents recorded were 250 μ A. The maximum variation in regulated voltage should have been less than 1.25 V. The accuracy of the voltage was stated to be 0.5% of the setting plus 0.2% of the rated voltage. Assuming a maximum set point voltage of 3000 V, the recorded voltage accuracy was less than or equal to 65 V. The repeatability was stated to be less than 0.1% of the range, or less than 25 V. For data processing, the actual recorded voltages could be skewed by up to 65 V, but for two voltage measurements at a given voltage, the maximum difference actual applied voltage was 25 V or less. When current was collected for a duration of time at a set voltage, the supplied voltage should have not varied by more that 6.25 Vrms.

4.2.4 Vacuum Facility

The electrospray source was placed in a vacuum chamber to simulate a space environment. The vacuum chamber used was the Ultra High Vacuum (UHV) chamber at Michigan Technological University in the Ion Space Propulsion Laboratory. The dimensions of the tank were roughly 0.5-meter-diameter by 0.5-meter-deep. The facility was roughed down using a 110-liter/min dry scroll pump and a 280-liter/sec turbomolecular pump. The vacuum facility could be isolated from the turbomolecular pump and dry scroll pump using a gate valve. To reach higher vacuum, a 300-liter/sec ion pump was used. The base pressure of this facility was 10^{-9} Torr. During testing the pressure was observed to vary between 10^{-8} to 10^{-5} Torr. Power and signals were passed into and out of the tank using a 4-pin

high voltage Conflat feedthrough.

4.2.5 Camera and Lens

Images of the electrospray source and the ILFF were taken by a Nikon D5000 camera with an AF-S Micro Nikkor 60-mm f/2.8 ED lens. This camera/lens setup was located outside of the vacuum chamber, rigidly affixed to a tripod. The vacuum chamber had a glass porthole to allow the camera to image the electrospray setup. Lighting was provided by a 150W Schott Ace Fiber Optic Light source with a dual goose neck fiber optic light guide. One of the fiber optic light guides was aimed through the window towards the rear of the vacuum chamber to provide ambient and background lighting, while the other was aimed at the ILFF.

4.2.6 Experiments conducted

Three discrete experiments were performed and are reported on in this chapter, and these experiments are briefly detailed in Table 4.1. The first experiment used an EAN-based ILFF (batch # NJ397007). The purpose of this test was to first determine if the ILFF could be placed in a vacuum chamber and spray from distorted Rosensweig instabilities when a sufficient electric field was supplied. If batch NJ397007 of ILFF could emit, the

current-voltage characteristics were to be measured. This experiment was performed a second time after receiving a new batch of ILFF. This batch (batch # NJ397028) was based off the hydrophobic ionic liquid EMIM-NTf₂. Once again, a test was performed to determine if this batch of ILFF could spray ILFF, and what the current-voltage characteristics were. The final experiment was to measure the onset voltage of the EMIM-NTf₂ based ILFF (batch # NJ397028), and the radius of curvature of the tip of the ILFF peaks, and the ILFF tip-to-extraction electrode distance.

Table 4.1
FerroTec EFH-1 Fluid Properties

Experiment #	Batch #	Base Ionic Liquid	Goal of test
1	NJ397007	EAN	Observe emission Measure I-V characteristics
2	NJ397028	EMIM-NTf ₂	Observe emission Measure I-V characteristics
3	NJ397028	EMIM-NTf ₂	Measure onset voltage and the geometry of the peaks to compare to theory

4.3 Experiment 1: Emission study of EAN based ILFF(batch # NJ397007)

4.3.1 Observing emission

The first ILFF emission tests were conducted using the electrospray setup described in Section 4.2.1 (Figure 4.1 and the left of Figure 4.2), and the second developed EAN-based ILFF (batch number NJ397007). When the ILFF was placed in the fluid holder (as pictured in the left image of Figure 4.2) and then placed in the apparatus with the magnets, five (5) Rosensweig peaks formed on the fluid (Figure 4.3). This was then assembled and placed in the UHV vacuum facility.

The first part of the experiment was to observe ion and/or droplet emission from the ILFF. The first observation of ion and/or droplet emission was when the batch # NJ397007 of the ILFF was biased to -3700 V. At this voltage, a current of $6.75 \mu A$ was recorded. Emission of positive spray was also observed in testing. A progression of an ILFF peak as the voltage was increased from 0 V to -3700 V can be viewed in Figure 4.4. In Figure 4.4, the progression of the ILFF deformation is shown as the potential difference between the extraction electrode and the fluid is increased in magnitude. The higher the magnitude of the applied voltage, the taller and sharper the peaks become. The change in tip shape is

very evident in the two rightmost images from Figure 4.4, when it goes from not emitting at -3600 V, the tip is rounded, to ion emitting at -3700 V with a very sharp tip. This transition between a rounded tip and a sharp tip emitting ions appeared to be instantaneous. In the rightmost image of Figure 4.4, there are bubbles at the base of the peak that only appeared once the ILFF began emitting ions. It is believed that these bubbles indicate that there is some sort of electrochemistry happening in the ILFF at boundary of the ILFF and fluid holder. This sort of electrochemistry has been observed in other electrospray experiments and is one of the primary reasons most electrospray researchers alternate the biasing of their ionic liquids between positive and negative [2, 91, 92]. The polarity of the voltages in these experiments were not alternated because of a lack of available bi-polar power supply at the time, and because the tests with EAN-based ILFF (batch # NJ397007) were conducted as a proof of concept.

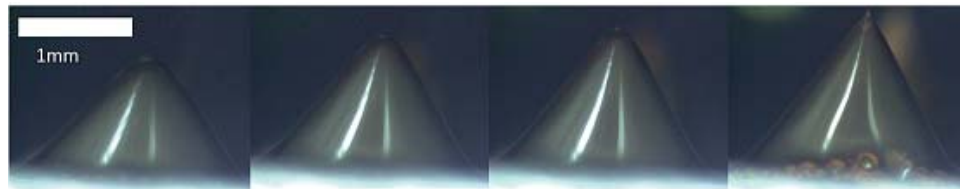


Figure 4.4: Progression of EAN based ILFF peaks as voltage is applied. Left: an image of a single peak in the array of 5 peaks with no voltage applied (0 V). Middle left: image of the same peak with -3000 V applied. Peak height increases and tip becomes slightly sharper. Middle right: applied voltage has been increased to -3600 V, and the peak has grown in height and is sharper. Right: applied voltage is -3700 V. At this voltage, the array began emitting ions. Also notable is the presence of bubbles at the bottom of the rightmost image, most likely due to some electrochemical reaction.

4.3.2 I-V Curves

A graph of the applied voltage and collected current versus time for the EAN-based ILFF (batch # NJ397007) is shown in Figure 4.5. This figure was a snippet of a longer test. In Figure 4.5, the voltage was changed in roughly 50 V increments every 10 to 15 seconds. The voltage ranged from -3200 V to -3650 V. The onset voltage was approximately -3200 V with an extraction-electrode-to-fluid-holder spacing of 4.6 mm. The tip-to-extraction electrode spacing was less than this gap and was not measured in these experiments. The collected current increased when the magnitude of the voltage increased, and decreased when the applied voltage decreased. At onset of emission, the current was 2 μA , and rose to an average of 14.5 μA at -3650 V. When decreasing the magnitude of the voltage back to zero, emission stopped at -2950 V, or 250 V less than the onset, and was due to hysteresis. At 71 seconds, the current jumped from 8.8 μA (applied voltage was -3525 V) to 13.1 μA (with an applied voltage of -3575 V). While measuring the I-V characteristics of the array, it was noticed that not all 5 of the ILFF peaks were emitting. Therefore it was likely that when the current jumped in value, that peak that was not previously emitting, began emitting. The sharp decrease in current at 83 seconds was also likely caused by a decrease in the number of peaks emitting.

To determine if there was hysteresis in the emitted current between the magnitude of the voltage being increased versus decreased, the emitted current data from Figure 4.5 was

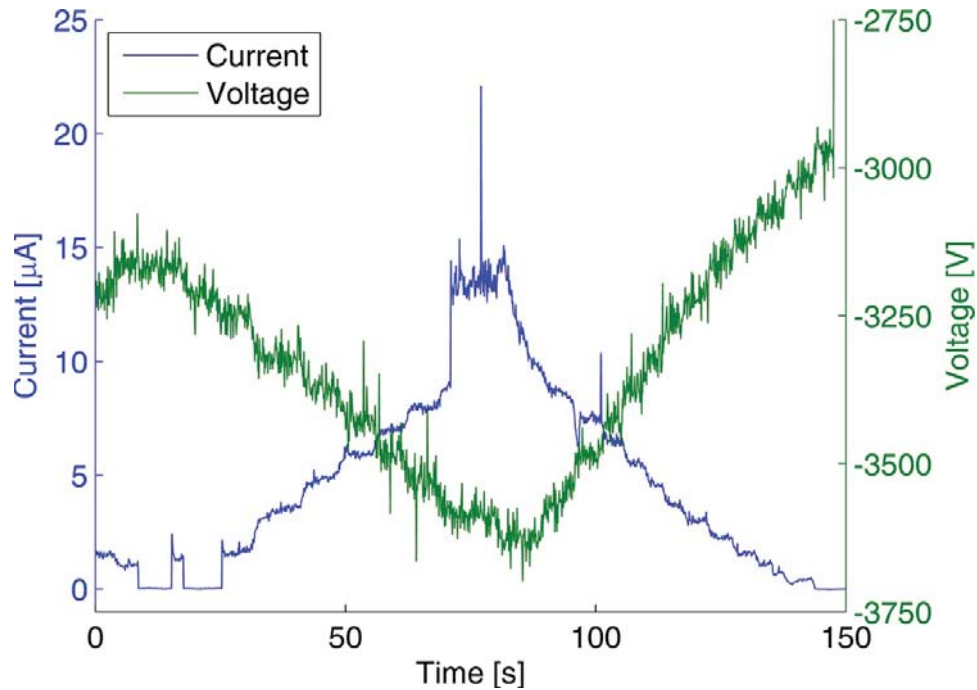


Figure 4.5: Emitted current and applied voltage versus time of EAN based ILFF. Green line denotes voltage and blue line denotes current.

averaged over each span where the voltage was held constant. These data are shown in Figure 4.6. The blue lines with open circles represent the data where the magnitude of the applied voltage was increased. The green lines with crosses represent the data corresponding to the magnitude of the voltage decreasing point-to-point. The onset of emission and the ceasing of emission are marked with text leaders. The emission ceased at a lower voltage magnitude than was required for the onset of emission. This occurred because a critical electric field was required to deform the ILFF peak, and create the Taylor cone. These deformations caused a higher local electric field, meaning the required voltage to maintain these deformations was lower than that required to form them, as can be viewed in Figure 4.6 where emission ceased 300 V lower in magnitude than onset of emission

occurred. The measured current at a given voltage was the same for both increasing and decreasing voltage magnitudes until the decreasing voltage magnitude was within 100 V of the emission onset voltage. At this point until the cease of emission, the measured current for the decreasing voltage magnitude case ranged from equal to 2.4 μA higher than the current for the same voltage as the increasing voltage magnitude case.

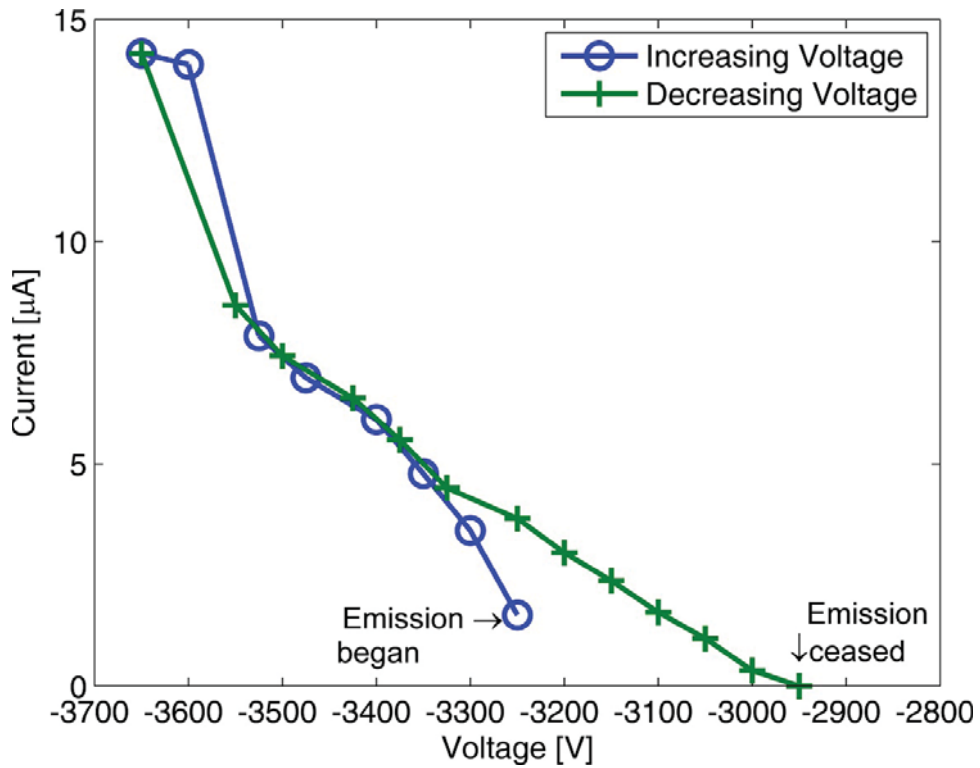


Figure 4.6: Emitted current versus voltage. Blue line with open circles denotes the emitted current as the magnitude of the voltage was increased while the green line with crosses denotes the emitted current as the magnitude of the applied voltage was decreased.

4.3.3 Other Observations During Experiment 1

4.3.3.1 Current collector visibly coated with ILFF

The ITO glass used as the current collector also served as a witness plate. A picture of the ITO glass post test is shown in Figure 4.7. There were 4 rather dark areas on the glass. This showed that during the experiment, four, possibly five, of the five peaks were emitting ions. The remains collected on this witness plate were dark and light brown. Pure EAN was a clear liquid, the magnetic nanoparticles added to the liquid were what gave it a dark brown color, as can be seen in any of the images of the ILFF. This implied that what was sprayed was the ionic liquid and the magnetic nanoparticles. Investigations into what was sprayed, and how it may or may not effect the beam characteristics were out of the scope of work, and being performed by others.

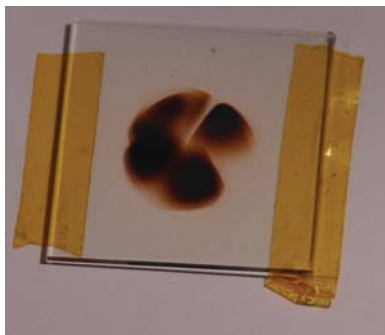


Figure 4.7: ITO glass current collector and witness plate post emission test.

4.3.3.2 Self-regeneration of Emitter Sites

One of the issues facing electrospray in general is the damage of the support structure. The support structure was the micromanufactured capillary or needle-like structure that supported the fluid and provided electric field enhancement. This support structure damage could be from arcing, heavy ion bombardment, electrochemical deterioration, or mechanical deformation. On terrestrial devices such as a Focused Ion Beam (FIB), the source is user serviceable and replaceable. On a spacecraft this is not the case. Each and every emitter must be designed to work for many hundreds of hours of operation.

The ILFF-based electrospray source has demonstrated the ability to self-repair from what would typically be considered a catastrophic event. During many experiments, the author increased the fluid-to-extraction-electrode voltage too high and created many arcs between the ILFF and the extraction electrode. In every case, the array would follow the same trend: 1) emit ions and/or drops 2) arcing event occurred 3) power supply recovered from arcing event (voltage dropped) and the distorted peaks became “Rosenzweig instabilities” 4) voltage returned, peaks became enhanced and begin re-emitting ions and/or drops. This showed that the array could recover from arcing events.

Another unexpected observation while conducting experiments was watching a peak essentially explode during operation, and then return to normal operation. A series of images depicting this entire sequence can be found in Appendix D. While the array was

emitting, bubbles were noticed at the base of the peaks of the ILFF (see rightmost of Figure 4.4, and leftmost of Figure 4.8). After continued operation (roughly 15 minutes), one of the peaks formed a very large bubble (center of Figure 4.8) and that peak stopped emitting ions. A few seconds later, the very large bubble exploded, and formed two (2) small peaks. Over the course of roughly two minutes, one of the two newly formed peaks slowly grew and began emitting ions again, see the right image of Figure 4.8. This slow time scale was because the ILFF was viscous. The ILFF was typically heated with a heat gun to allow lower the viscosity enough to transfer between containers. An interesting note about the newly emitting peak was the asymmetry observed.



Figure 4.8: Series of images showing a peak emitting, become damaged, and then self-repair and begin emitting again, with no operator intervention. Left: Peak emitting ions, small bubbles visible at the base of the peak. Center: A large bubble appears in the peak, and emission from this peak ceases. Right: After the bubble burst, peak begins emitting ions again.

4.3.3.3 Multi-Site Emission

An interesting phenomenon was noticed while testing with the EAN-based ILFF. It was observed that a single ILFF peak could have multiple macro-scale emission sites located

on the tip of the peak. These multiple emission sites were located on the same peak that had previously exploded and reformed, as discussed in the previous section, Section 4.3.3. Each additional peak was observed to form, each taking roughly 10-15 seconds to finalize their position. A detailed sequence of images is located in Appendix D.

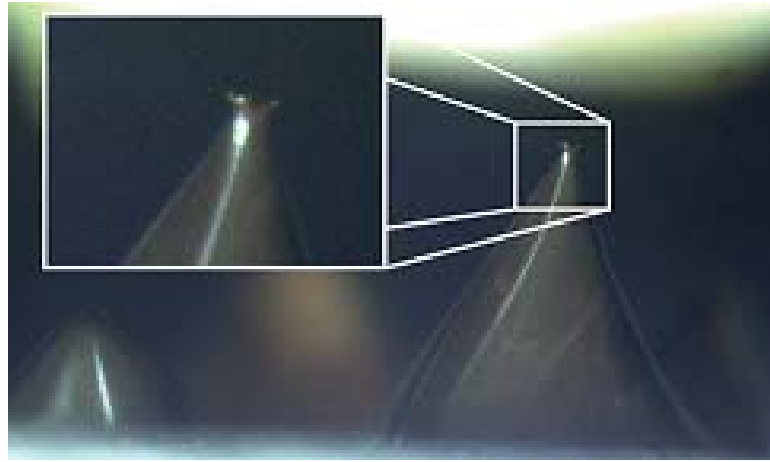


Figure 4.9: A zoomed-in image three emission sites on the tip of a single peak in an EAN-based ILFF.

4.3.4 Discussion of the Results from Experiment 1 with EAN-based ILFF (batch # NJ397007)

Experiments showed that the EAN-based ILFF (batch # NJ397007) was able to form 5 stable Rosensweig instabilities from permanent magnets placed below the ILFF, and when a sufficiently strong electric field was applied, emission occurred from the ILFF peaks. This emission was confirmed by both current measurements during the experiment and post-test

with a witness plate. The current-voltage characteristics of the array were measured, and the current was found to increase as the magnitude of the applied voltage increased.

Two interesting phenomenon were also observed during the experiment. First, bubbles formed in the ILFF, likely electrochemistry from the ILFF emitting in a single polarity for too long at a given current. These bubbles destroyed one of the ILFF peaks, but the peak later re-formed and began ion and/or droplet emission once again. The peaks were also found to be resilient to electrical arcing events, such as when the applied voltage was increased too high. Finally, multiple emission sites were observed to form and emit from one of the peaks. The cause of this was unknown.

4.4 Experiment 2: Emission Study of EMIM-NTf₂-based ILFF (batch # NJ397028)

4.4.1 Observing emission

Experiment 2 was conducted in a different manner than Experiment 1. First, the entirety of the EMIM-NTf₂-based ILFF (batch # NJ397028) was imaged instead of a single peak. Because the depth of view of the macro lens was shallower than the depth between individual peaks, typically only a single peak was in focus at a time. Second, the ILFF

was regularly operated in either the positive ion/charged droplet mode or the negative ion/charged droplet mode. The first goal of Experiment 2 was to obtain emission from the ILFF. Emission was first observed with the ILFF biased with a positive voltage. Current was measured when the applied voltage was +2390 V. Soon after, the applied voltage was returned to zero, and then the negative power supply was connected to the ILFF pool. Emission of negative spray was measured at -2600 V. Figure 4.10 shows the EMIM-NTf2-based ILFF in the experimental setup for ion emission. The left image of Figure 4.10 shows the peaks formed solely due to the magnetic field (Rosensweig instabilities), and the right image shows the same peaks emitting ions with 2700 V applied between the fluid and the extraction electrode.



Figure 4.10: EMIM-NTf2 based ILFF in annular fluid holder. Left: ILFF exposed to magnetic field only (Rosensweig instability). Right: ILFF exposed to magnetic and electric field, applied voltage was 2700 V, and emitting ions.

4.4.2 I-V Curves

The next set of tests performed on the EMIM-NTf2-based ILFF (batch # NJ397028) was to measure the I-V curves. A total of four I-V traces were collected, two biasing the fluid

to a positive potential, and two with a negative potential. The I-V data collection was conducted after fresh ILFF was put into the electrospray source. The two positive I-V traces were conducted back-to-back, using the same ILFF. The electrospray source was then removed and cleaned, and fresh EMIM-NTf₂-based ILFF (batch # NJ397028) placed in the electrospray source. The next two I-V traces were conducted back-to-back to each other, and in both runs the ILFF was biased negatively.

The first voltage and measured current data set had the EMIM-NTf₂-based ILFF biased positively. The recorded voltage and measured current versus time can be seen in Figure 4.11. The recorded voltage signal varies around ± 25 V from the voltage set point. The actual voltage output ripple, according to the manufacturer's specifications, should not be varying by this amount, but less than a 6.25 Vrms. The large scale 'ripple' of ± 25 V about the set point voltage was found in all the data that used the Glassman FX +25 kV power supply. This ripple in the recorded data was even noticed when the set point voltage was set to zero. The power supply voltage was monitored with a digital multimeter at low voltage (< 300 V) and the output was found to be within 10 V of the set point.

In Figure 4.11, the measured current was varying constantly. The largest difference between the minimum and maximum measured current at a single voltage set point was 22 μ A. At many of the voltage set points, the current had a tendency to decay over time. For instance from 177 seconds until 262 seconds, the voltage was set to 2500 V. The current initially spiked to 10.4 μ A and then dropped to 3.4 μ A after 10 seconds. The current

slowly decayed to $1.6 \mu\text{A}$ after 34 seconds. The current then jumped up to $8.2 \mu\text{A}$ and steadily decayed down to $1.3 \mu\text{A}$ over 35 seconds. This similar trend occurred again from 262 seconds until 313 seconds after the voltage was set to 2550 V. The voltage initial spiked up to $11.5 \mu\text{A}$ and fluctuated in that region before going down to $5.6 \mu\text{A}$ 8 seconds later. The current trended down to $1.7 \mu\text{A}$ at 312 seconds, but not after a few times the current increased up to $7.4 \mu\text{A}$ and $23.3 \mu\text{A}$. At higher extraction voltages, this decaying current trend was not readily observed. At 2750 V between 574 seconds and 631 seconds, the current even appeared to increase over time before the voltage was turned off. The ILFF peak were imaged during emission. When the voltage was set to 2750 V, multi-site emission was observed, similar to what is shown in Figure 4.16.

Between Runs 2 and 3, the vacuum chamber was vented, the fresh ILFF was put into the test apparatus and the current collector was replaced with a new one. After reaching vacuum, Run 3 measured the emitted current for various voltage set points where the fluid was biased negatively. The collected current and voltage data versus time are shown in Figure 4.13. Onset of emission began at 2200 V. The initial measured current was $4.2 \mu\text{A}$ at 43 seconds and decayed to $2.0 \mu\text{A}$ 60 seconds later. Between 157 seconds and 215 seconds, 2475 V, the current rose from an initial value of $67 \mu\text{A}$ to a maximum of $100 \mu\text{A}$ over 14 seconds and then fell to $43 \mu\text{A}$ after another 42 seconds. Compared to Runs 1 and 2, the maximum current was 2.5 times higher and this occurred at lower voltages.

A second set of current-voltage data versus time was collected with the ILFF fluid biased

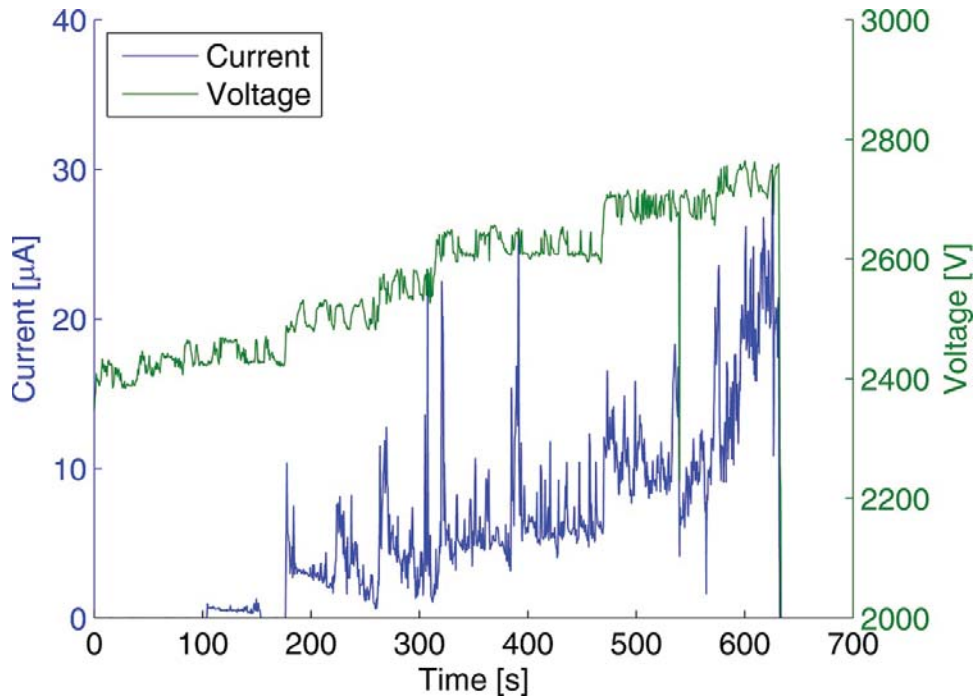


Figure 4.11: Voltage and measured current data from Run 1, also called Positive 1.

Minutes after Run 1 was completed, Run 2, Figure 4.12, conducted to measure the current-voltage characteristics of the array with the fluid biased positively. This second run, measuring the current and voltage of the array did not have the decaying current over time trend that was observed at the lower extraction voltages from Run 1. At each voltage set point, the measured current of Run 2 was slightly higher than that of Run 1.

negatively, and is displayed in Figure 4.14. This run, Run 4, did not display the same current-decay-over-time that was observed with both Runs 1 and 3. There was a step down in measured current at 229 seconds from $164 \mu\text{A}$ down to $146 \mu\text{A}$. The current also spiked off the figure to $3338 \mu\text{A}$ at 211 seconds.

Each of the current and voltage traces from Runs 1-4 had their currents and voltages averaged over each of the voltage set points, each lasting between 30 and 120 seconds. The average currents and voltages along with the standard deviation of the current (used

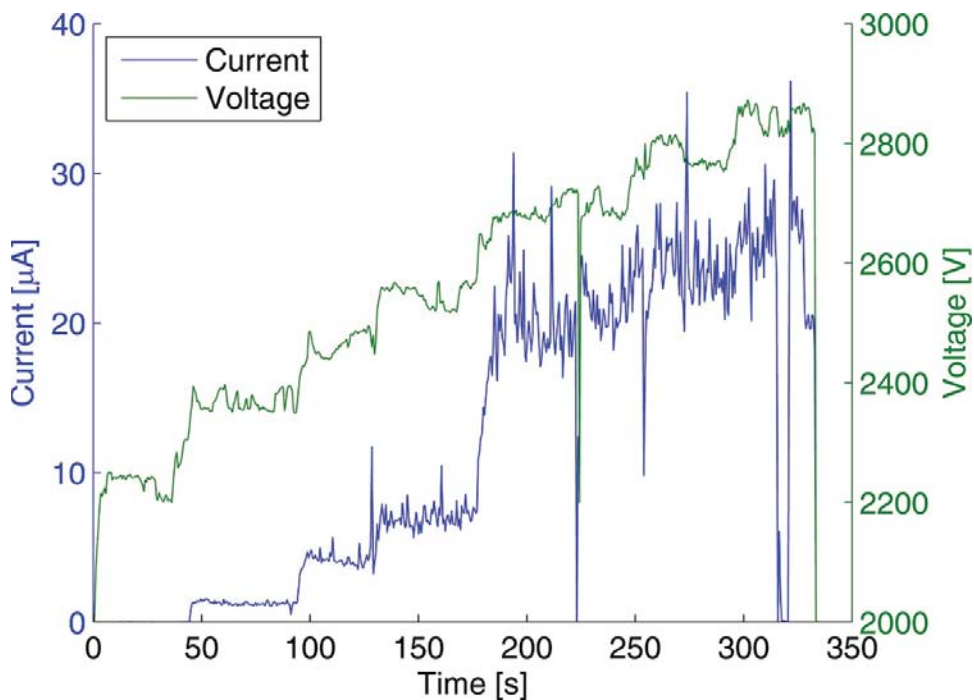


Figure 4.12: Voltage and measured current data from Run 2, also called Positive 2.

as the error bars) were plotted in Figure 4.15. In Figure 4.15, the measured current from biasing the ILFF negative were much higher than when the ILFF was biased positively. In literature, the measured current when an ionic liquid electrospray source was operated tended to obtain roughly the same current when biased positively versus negatively [93,94].

In conventional needle or capillary electrospray sources, the solid substrate does not change from test-to-test, unless a catastrophic event occurs to the substrate. This allows for a consistent spacing between substrate and the extraction electrode for each test. Therefore the starting voltage from test to test should remain fairly constant. Unlike conventional needle or capillary electrospray sources, controlling the tip-to-electrode spacing and tip

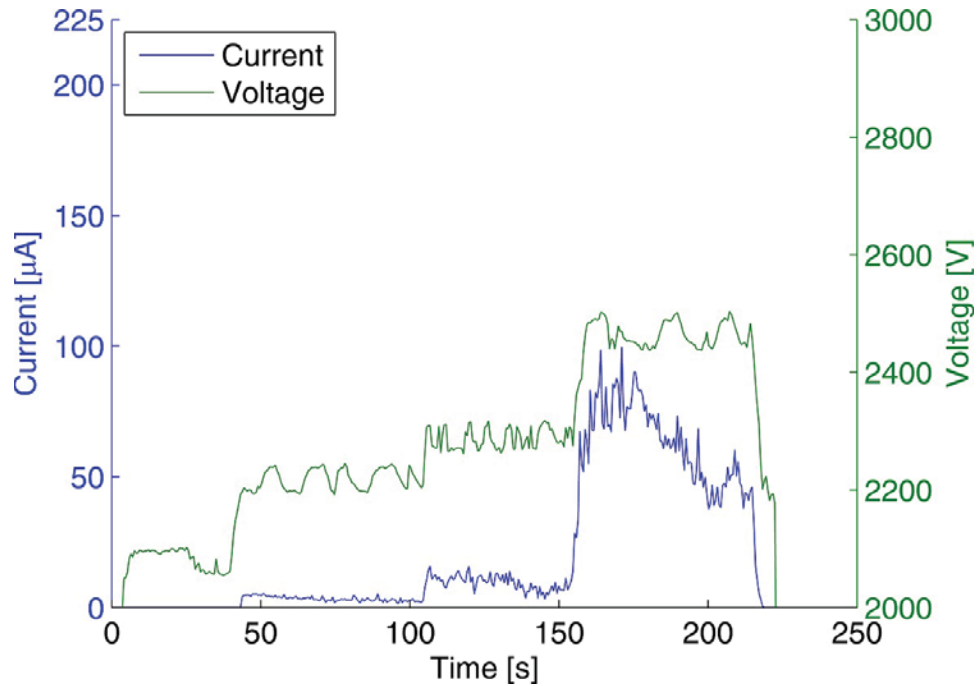


Figure 4.13: Voltage and measured current data from Run 3, also called Negative 1. Voltage magnitude shown, actual voltage was negative.

radius of curvature was not as easy between tests. The volume of fluid placed into the aluminum fluid holder was not closely metered. ILFF was added until the fluid filled the annular trench, but the surface of the fluid would sometimes be convex or concave, while pinned at the corners of the trench. This allowed for the peak heights to vary test-to-test. Also, as a measurement took place, the volume of fluid in the aluminum fluid holder decreased. For instance, this meant that the I-V trace for Positive 2 had shorter peaks than Positive 1. Because of this, it was not easy to make direct comparisons between any of the four I-V traces displayed in Figure 4.15. To supplement this, Table 4.2 was included that provided the tip-to-electrode spacings along with the radius of curvatures for each of the I-V traces. The tip radius and tip-electrode spacing were both measured with no voltage applied

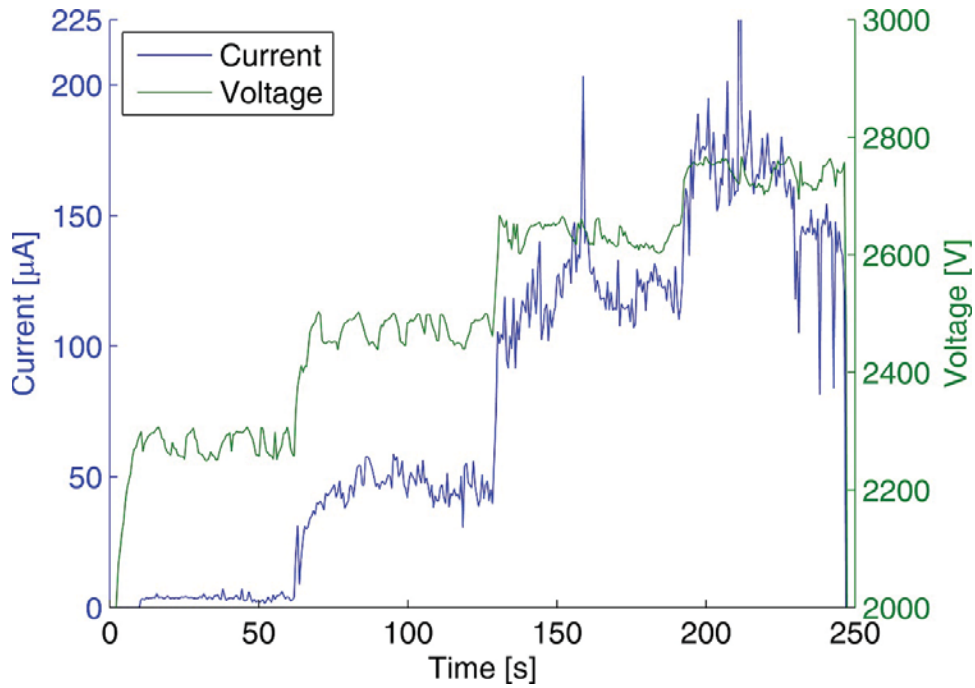


Figure 4.14: Voltage and measured current data from Run 4, also called Negative 2. Voltage magnitude shown, actual voltage was negative.

to the ILFF, so they are the tip radius and tip-electrode spacing due to the Rosensweig instability. Both the positive I-V traces had a peak average current of approximately $20 \mu A$ (blue and green curves in Figure 4.15). The negative I-V traces, however, had peak average currents of $64 \mu A$ (red curve) and $162 \mu A$ (black curve), respectively. The reason for the differences in collected currents between the two polarities was not evident.

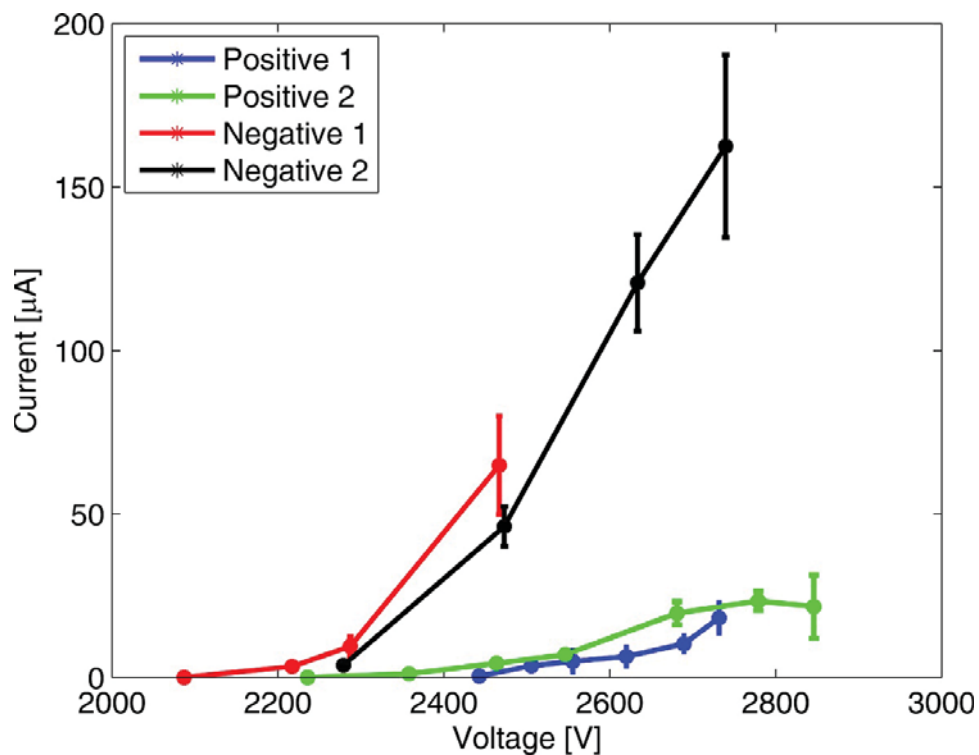


Figure 4.15: Multiple I-V traces of EMIM-NTf₂ based ILFF (batch # NJ397028). The blue and green data represent the ILFF biased positively, and the red and black data are when the ILFF was biased negatively. All data are shown on positive axes for easier comparison.

Table 4.2
ILFF Peak information for Runs 1-4

I-V trace Name	Positive 1	Positive 2	Negative 1	Negative 2
ILFF Bias Polarity	Positive	Positive	Negative	Negative
Tip-Electrode Spacing at V = 0 (mm)	2.33	2.43	2.21	2.37
Tip radius at V = 0 (mm)	0.529	0.233	0.233	0.331
Measured Starting Voltage (V)	2425	2350	2200	2475

4.4.3 Other Observations During Experiment 2

4.4.3.1 Multi-Site Emission

Similar to the EAN-based ILFF, the EMIM-NTf₂-based ILFF also exhibited a multi-emission site mode of operation from a single peak. There were two emission sites visible on a single peak in Figure 4.16, and there have been up to four emission sites observed in other testing. The cause of this phenomenon is unknown at this point, however, it has occurred regularly with high collected currents such as where the current collected from the array was $> 50 \mu A$. It could be that the high emitted currents could be due to the formation of these multiple tips on a peak, or it could be that higher emission currents can lead to some sort of instability, which caused multiple emission sites to form. They also tend to form at higher applied voltages. For instance, the twin tips emitting in Figure 4.16 occurred when the applied voltage was much higher than the onset. The high electrical stress could cause multiple emission sites to form per peak.

4.4.3.2 Other ILFF deformations and protrusions

During high current emission of the I-V trace Negative 2, a long protrusion was noticed forming on one of the tips. In Figure 4.17, a protrusion can be seen growing between the

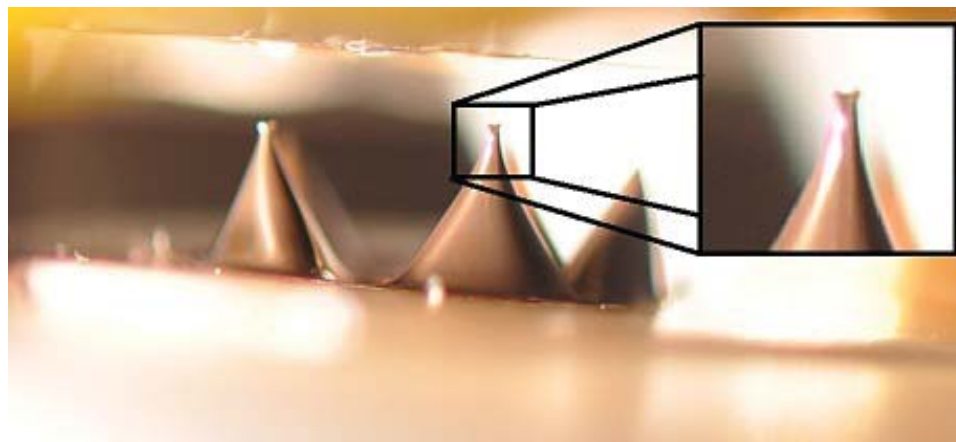


Figure 4.16: Multiple emission sites present on the tip of an emitting peak in an EMIM-NTf₂ based ILFF (batch # NJ397028). Onset voltage was 2750 V. The applied voltage was 3150 V.

left and middle images. This occurred over the course of 4 seconds. Less than a second later this protrusion “exploded,” and it appeared that a cone of spray formed in its place. This was only observed to occur once during testing. These series of images occurred at a constant applied voltage of -2750 V, and the collected current was between 150 and 225 μA .

A feature present in all three of the images in Figure 4.17 was a downward-facing cone attached to the extraction electrode. This downward-facing cone developed because a portion of the spray was intercepted by the extraction electrode. After enough of fluid built up on the extraction electrode, the downward-facing cone appeared, and even appears to have formed a Rosensweig instability. It is possible that this downward-facing cone could have created reverse spray, and deposited some of built-up fluid from the extraction electrode back into the bulk fluid below. This may be a useful feature of this type of



Figure 4.17: Sequence of images elapsed over the course of less than 5 seconds with a constant voltage applied. In the left image, the peak on the right was emitting. In the middle image, the peak grew a long protrusion while still appearing to be emitting. The rightmost image the protrusion “exploded” and appeared to form a cone of spray. The applied voltage was -2750 V and biased negatively (emitting anions) and the collected current was between 150 and $225\ \mu\text{A}$. In all the images there was a downward-facing cone attached to the extraction electrode. This downward-facing cone was created because part of the spray being intercepted by the extraction electrode. After enough ILFF built up on the extraction electrode, the downward-facing cone appeared. It was unknown if this downward-facing cone was spraying toward the lower pool of ILFF.

electrospray source, be able to self-clean ILFF that was intercepted by the extraction electrode. Another result of some of the spray being intercepted by the extraction electrode was that any fluid intercepted by the extraction electrode was emitted current that was not measured. This means the actual emitted currents may have been higher than the measured collected currents in the I-V curves from Section 4.4.2.

4.4.4 Discussion of the Results from Experiment 2 with EMIM-NTf2-based ILFF (batch # NJ397028)

Experiment 2 showed that the EMIM-NTf2-based ILFF (batch # NJ397028) was able to spray ILFF from deformed Rosensweig instabilities when the applied voltage was high enough. This was also confirmed with the current collector/witness plate post I-V traces Positive 1 and Positive 2, as can be viewed in Figure 4.18. Based on the stains found on the current collector, it appeared that only two or three of the five ILFF peaks were emitting. Four I-V traces were recorded, two for positive emission, and two for negative emission. The emitted current increased for both positive and negative emission as the magnitude of the voltage was increased. If all of the peaks were emitting in I-V trace Negative 2, the peak average current per emitter would be $32.4 \mu\text{A}$, while typical emission currents for needle emitters were in the range of $0.1\text{-}1 \mu\text{A}$ [11, 19, 94]. If less than all 5 of the peaks were emitting, then the average current per active emitter would have been higher. Electrospray sources utilizing Rosensweig instabilities in an ILFF could increase the current density of the electrospray source by being able to emit at higher currents per peak than has been available.

During Experiment 2, there were a number of transient effects of the ILFF observed. First, the multiple emission sites on a single tip were observed numerous times during Experiment 2, all observed to occur at higher emission currents (collected current from

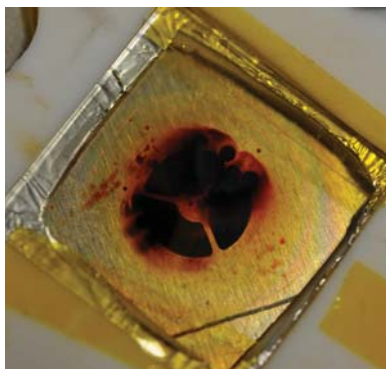


Figure 4.18: Current collector after positive emission from I-V traces Positive 1 and Positive 2. There appeared to be 2-3 sites of emission.

the array was $> 50 \mu\text{A}$). This phenomenon was also observed occurring in Experiment 1. Second, a long jet was observed to grow from one of the ILFF peaks and eventually disperse in what appeared to be a large spray of ILFF. This occurrence also happened at high emission current, in this case ranging from $150 \mu\text{A}$ to $225 \mu\text{A}$ for the array. During the high emission current time periods, a downward-facing cone was observed to form on the extraction electrode, Figure 4.17. It is possible that at this high current mode, the beam width increased, causing a large amount of mass to be intercepted by the extraction electrode. The presence of the downward-facing cone also means that a portion of the emitted current was intercepted by the extraction electrode, which would mean that the emitted current was higher than the collected/measured current. From these observations, there appears to be some sort of instabilities that were able to develop at higher current emission.

4.5 Experiment 3: Onset Voltage Study of EMIM-NTf2-based ILFF (batch # NJ397028))

4.5.1 Comparison of measured onset voltage to predicted onset voltage

This final experiment, Experiment 3, was conducted with the purpose of determining the applied voltage required to cause ion and/or droplet emission from an ILFF with peaks formed by a magnetic field. Traditionally, the starting voltage of an electrospray source is governed by the balance of surface tension forces and electric traction forces, as discussed in Section 2.2. This analysis yielded a prediction of the required voltage for a needle or capillary to begin ion and/or droplet emission, and this expression was given in Equation 2.9. However, in the case of the ILFF, both magnetic and electric traction forces work against the surface tension force. Because of this, it was thought that the onset voltage may not match the predicted onset voltage from Equation 2.9.

In Experiment 3, EMIM-NTf2-based ILFF (batch # NJ397028) was put into the annular ring of the aluminum fluid holder in the electrospray source. Onset voltage was defined to be the voltage (positive or negative) where current above the noise floor was detected. To predict the onset voltage, three pieces of information were needed. First was the surface

tension of the ILFF, and this was known. The next two pieces needed were the tip radius, r , and tip-to-electrode distance, d . The tip radius and tip-to-electrode distance were measured by imaging the ILFF with no voltage applied (only the Rosensweig instability) and then scaling the image with a known distance in the image.

A total of seven start-up tests were performed, a listing of all the tests and their results are in Table 4.3. The first four start-up tests were conducted in parallel with Experiment 2 from Section 4.4. The next three tests were performed exclusively for measuring the onset voltage. The ILFF was replaced between some of the start-up tests. Unused ILFF was put into the electrospray source before Tests 1, 3, and 5. All seven of the start-up tests were found to have an onset voltage 16 to 24% below the theoretical onset voltage predicted by Equation 2.9. An error analysis was performed on the measurements used to predict the onset voltage, and is discussed below in Section 4.5.3. Defining the error as a single standard deviation of the tip radii and tip-to-electrode distance measurements, the theoretical onset voltage was found to vary less than 2% of the value listed Table 4.3.

Table 4.3

Measured and predicted values comparing measured onset voltage to predicted onset voltage. Tip radius and Tip-electrode spacing were measured with no applied voltage/electric field.

Start-up Test	1	2	3	4	5	6	7
ILFF Voltage Polarity	Pos	Pos	Neg	Neg	Pos	Neg	Pos
Tip-Electrode Spacing (mm)	2.33	2.43	2.20	2.36	2.43	2.62	3.21
Tip radius (mm)	0.529	0.233	0.233	0.331	0.274	0.277	0.270
Predicted Onset Voltage (V)	3202	2969	2873	3098	3045	3132	3333
Measured Onset Voltage (V)	2425	2350	2200	2475	2390	2600	2800
Percent Difference	-24%	-21%	-23%	-20%	-22%	-17%	-16%

Start-up tests 1 and 2 were run within minutes of each other, and the entire test apparatus remained at vacuum. The ILFF was biased with a positive voltage. The tip radius between the two tests decreased from 0.529 mm to 0.233 mm, and the tip-to-electrode spacing increased from 2.33 mm to 2.43 mm. The decrease in tip radius could have been caused by hysteresis where the ILFF did not relax as far as before emission. The increase in tip-to-electrode distance was due to mass loss from ion and/or droplet emission. There was only a slight change in the percentage difference between start-up tests 1 and 2.

Start-up tests 3 and 4 were then run back-to-back with the ILFF biased with a negative voltage. From start-up test 3 to 4, the tip radius and the tip-to-electrode spacing both increased. The tip-to-electrode spacing increased because mass was ejected by the electrospray process. The increase of the tip radius could have been caused by the loss of ILFF. The width of the base of the ILFF peaks remained constant, while the peaks became shorter. This change in geometry could have led to the increase in tip radius. With an increase in both the tip radius and tip-to-electrode spacing, the measured onset voltage in start-up test 4 increased compared to start-up test 3, as would be expected. Between the two tests, there was a slight to negligible change in the percent difference between the measured starting voltages and the predicted starting voltages.

Start-up tests 5, 6, and 7 were also run back-to-back, but the biasing voltage alternated between tests from positive to negative to positive. Over the course of the three tests, the tip-to-electrode spacing increased from 2.43 mm up to 3.21 mm for the last test. This,

as described before, was due to the loss of mass in the ILFF due to electro spraying away some of the ILFF. Interestingly, the tip radii between the tests remained fairly constant at 2.74 ± 0.04 mm. The measured, and predicted, onset voltages in each progressive test increased, as would be expected due to a decrease in electric field with a larger gap between the ILFF tip and the extraction electrode. Between start-up tests 5 and 6, there was an increase (became more positive) in the percent differences of the measured onset voltage to the predicted onset voltage. It was possible that this could have been caused by the change in polarity of the spray, however when the biasing polarity was returned back to positive in start-up test 7, there was no significant change in percent difference between the tests. It may have been that between start-up tests 5 and 6 that there was hysteresis where the ILFF peak did not fully relax, similar to what was suggested to occur between start-up tests 1 and 2, and the hysteresis was still present going into start-up test 7.

4.5.2 Behavior of onset of ion emission

In the previous section, Section 4.5.1, the theoretical onset voltages and measured onset voltages for ILFF based electro spray differed, with the measured onset voltages about 20% lower than the theoretical onset voltages. It has been observed during testing that the ILFF peaks grow in height, and the radius of the tip decrease as an electric field was applied, as can be viewed in Figure 4.19. Contrast the case of the ILFF where the tip radius and the tip-to-electrode distance can vary significantly, with an electro spray source with a needle or

capillary where the curvature of the fluid and spacing between the fluid and the extraction electrode do not significantly vary before the Taylor cone forms. [95] In electrospray using needles or capillaries, the measured starting voltages were typically found to be within 15% of value predicted by Equation 2.9. [1, 96, 97]

With an electrospray source utilizing Rosensweig instabilities deformed by an electric field, there are four competing pressures: 1) Gravity

$$P_{gravity} = \rho gh, \quad (4.1)$$

2) Surface Tension

$$P_{surface\ tension} = \frac{2\sigma}{r}, \quad (4.2)$$

3) Magnetic Traction

$$P_{magnetic\ traction} = \frac{1}{2}\mu_0 M_n^2, \quad (4.3)$$

and 4) Electric Traction

$$P_{electric\ traction} = \frac{1}{2}\epsilon_0 E_n^2. \quad (4.4)$$

The pure Rosensweig instability was a balance between the magnetic traction pressure acting against gravity and surface tension. The magnetic traction pressure set the initial

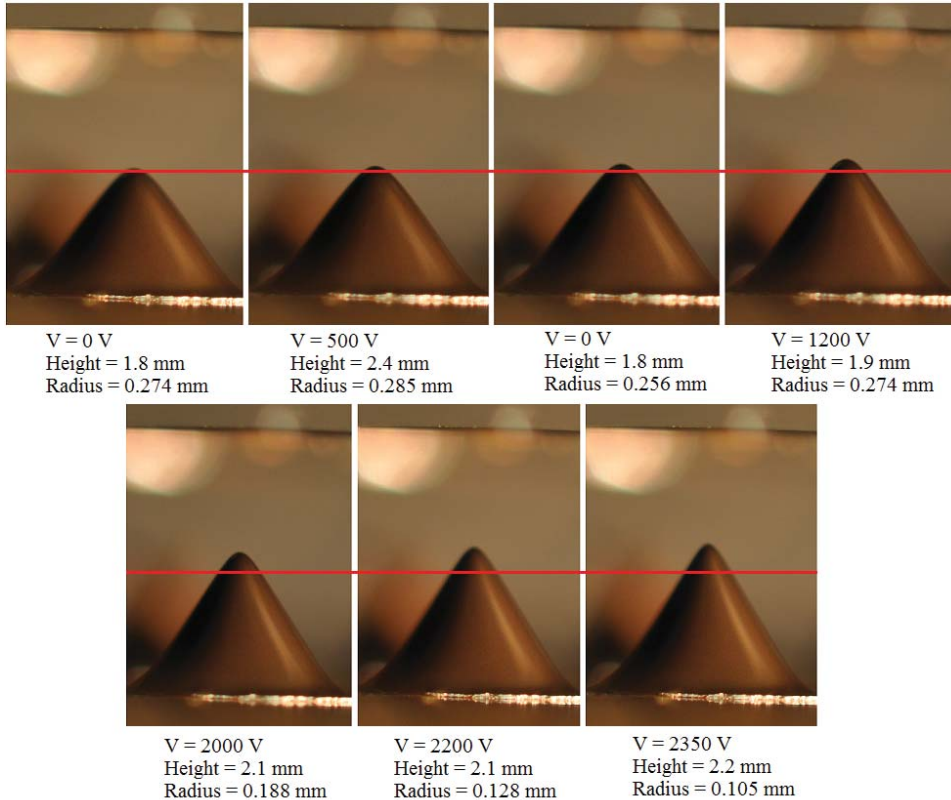


Figure 4.19: Sequence of images showing an ILFF tip with increasing applied voltages. Dashed line drawn across the images to draw attention to the change in fluid height to the reader's eye. Top Left: Rosensweig instability only, $V = 0$ V. Top Left Middle: Rosensweig instability supplemented with an electric field, $V = 500$ V. Top Right Middle: Rosensweig instability supplemented with an electric field, $V = 1000$ V. Top Right: Rosensweig instability supplemented with an electric field, $V = 1200$ V. Bottom Left: Rosensweig instability supplemented with an electric field, $V = 2000$ V. Bottom Middle: Rosensweig instability supplemented with an electric field, $V = 2200$ V. Bottom right: Rosensweig instability supplemented with an electric field, $V = 2350$ V. The peak heights grow and tip radii shrink with applied voltage.

height and tip radius of the ILFF peaks. As the electric field was increased, the pressure contribution from the gravitational and surface pressures must increase as well, meaning the interface must grow in height and/or the radius must decrease, until all four pressures

are in equilibrium.

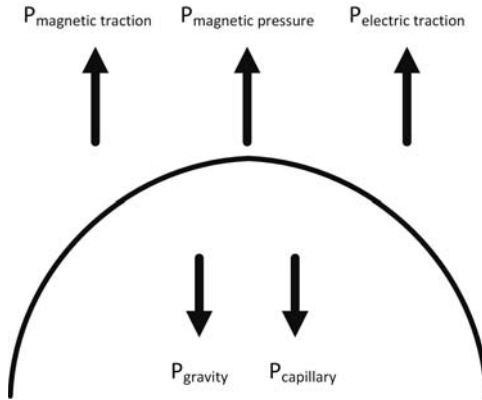


Figure 4.20: Pressure balance shown on a curved surface. The four pressures were gravity and surface tension working against electric and magnetic traction energy. The height and curvature of the interface was determined by these four energies.

The ILFF changed height and tip radius when an electric field was applied. These data were captured and used to determine the capillary pressure and pressure due to gravity at the tip of the ILFF. The data used for this analysis was collected during start-up test 5 from Section 4.4. During start-up test 5, as the voltage was increased, images of the ILFF peaks were taken at various voltages. Each of these images yielded a tip-to-electrode distance and a tip radius, and these are provided in Table 4.4, and shown in Figure 4.19 at their respective applied voltages. The measured onset voltage for start-up test 5 was 2390 V.

In Figure 4.21, the four competing pressures, gravitational, capillary, electric, and magnetic, were plotted against the applied voltage using the data from Run 5. The capillary stress was determined by measuring the radius of curvature of the tip of the ILFF. The

Table 4.4

Deformation of ILFF as voltage was applied to Run 5. The starting voltage was 2390 V.

Applied Voltage (V)	Tip-Electrode Spacing (mm)	Tip radius (mm)
0	2.44	0.274
500	2.44	0.285
1000	2.37	0.256
1200	2.28	0.218
2000	2.15	0.188
2200	2.06	0.128
2350	2.02	0.105

gravitational stress was determined by measuring the height of the ILFF. The electrical stress was found by combining the applied voltage with an electric field enhancement factor at each applied voltage. This electric field enhancement factor was determined by using Equation 2.8. The magnetic pressure was determined by using the applied magnetic field at the base of the ILFF and the relative permeability of the ILFF. As the applied voltage was increased, the magnetic pressure remained constant while the other three pressures, capillary, gravitational, and electric, increased. The gravitational pressure had a negligible increase in pressure from the 0 V applied to 2350 V applied. At 0 V, the balance of pressures was the magnetic pressure acting against the gravitational and capillary pressures. As the applied voltage was increased, the electrical stress increased, causing a growth in fluid height and a reduction in tip radius, causing the gravitational and capillary pressures to increase. This increase may be viewed easier in Figure 4.22 were each of the pressures was compared against the capillary pressure.

Figure 4.22 displays the ratio of magnetic pressure (constant) to the capillary pressure

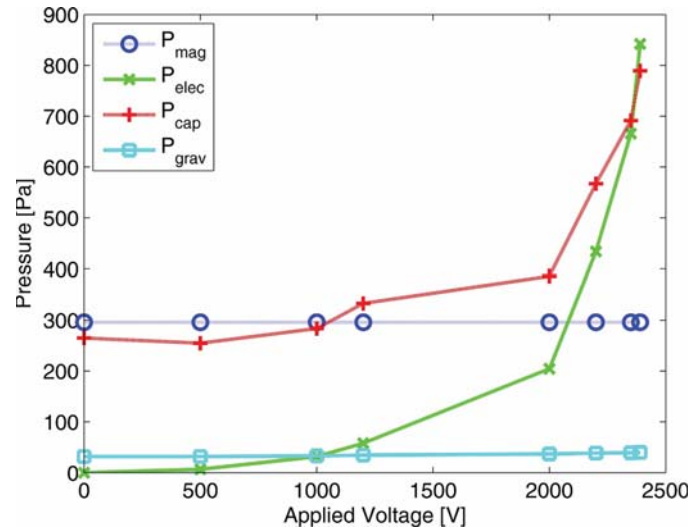


Figure 4.21: Pressure contributions from capillary, electric, magnetic and gravitational sources as the ILFF was stressed by an increasing applied voltage. Magnetic pressure, blue with open circles, was constant. Gravitational pressure, cyan with open squares, had a very small increase as the applied voltage was increased and the ILFF Rosensweig instability grew in height. Electric pressure, green with x's, increased because of the increase in applied voltage and the change in shape of the fluid. Electric field determined using Equation 2.8. The capillary pressure, red with crosses, increased as the ILFF Rosensweig instability tip radius decreased as the voltage was increased.

(changed with tip radius) and the ratio of electric pressure (using Equation 2.5) to capillary pressure during start-up test 5. If all of the pressures are known well, adding the summation of the relative magnetic and electric pressures and subtraction of the relative gravitational pressure should result in a line at 1, or where the combination of the three displayed stresses equal the capillary pressure. In Figures 4.21 and 4.22, the electric pressure at 2375 V was greater than the capillary and gravitational pressures combined. This most likely meant that there was an error in determining one (or more) of the pressure terms. The most probable cause for error was the electric field. The electric field was likely estimated to be

too high. Equation 2.8 yields good results with a high aspect ratio (long slender needles) whereas the base width and height of the ILFF peaks were the same order of magnitude. [6] To test this, an axisymmetrical model of each of the ILFF shapes was created in an electrostatic finite element analysis tool called QuickField. The details of this process can be found in Appendix E. Electric fields for each of the geometries was calculated and used in Figures 4.23 and 4.24.

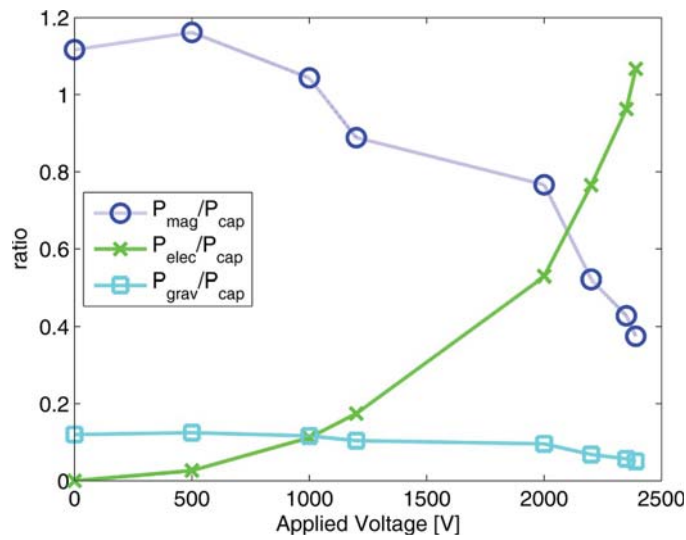


Figure 4.22: Ratio of magnetic pressure to capillary pressure and electric pressure to capillary pressure for start-up test 5 as the applied voltage was increased. Magnetic pressure to capillary pressure shown as the blue curve with open circles. Ratio of gravitational to capillary pressures is shown as, a cyan curve with open squares. The ratio of electric pressure to capillary pressure is displayed as, a green curve with x's. Electric field determined using Equation 2.8.

Figures 4.23 and 4.24 differed from Figures 4.21 and 4.22 with the method used to determine the electric field at the tip of the ILFF. In Figure 4.24, the pressures at an applied voltage between 0 and 1000 V have good agreement where the pressures balance, or the

difference between the magnetic and electric pressures versus capillary and gravitational pressures were less than 5%. Above an applied voltage of 1000 V, the difference between the two sets of pressures was as high as 33%. This discrepancy at the higher voltage was likely caused by the electric field predicted by the finite element method not matching the actual electric field. The reason for suspecting the electric field as the culprit for the source of error was the height of the ILFF only had a small change, so the gravitational pressure change was negligible compared to the other stresses. The magnetic pressure was constant at each applied voltage because the fluid properties likely did not change and the applied magnetic field was constant. The capillary pressure could contain some sources of error because the tip radius was only measured from one orientation, however, a measured error in the tip radius would effect both the capillary pressure as well as the electric pressure. For predicting the electric field, the geometry and aspect ratios of the ILFF did not fit well the assumptions typically applied to Equation 2.8, which would lead to a difference between the predicted and actual electric fields. The electric field predicted by the finite element method modelled ILFF Rosensweig instability as a axisymmetric system, which was probably not a fully accurate description of the ILFF geometry. An example of this asymmetry can be viewed above in Figure 4.17 where the side profiles of the ILFF have a tendency to ‘lean’ away from the center of the ring of ILFF fluid.

Two different electric field prediction techniques yielded two different estimates of the electric field. These electric field predictions are provided in Figure 4.25. The two techniques appear to have bounded the electric field, in this case. The advantage of using an

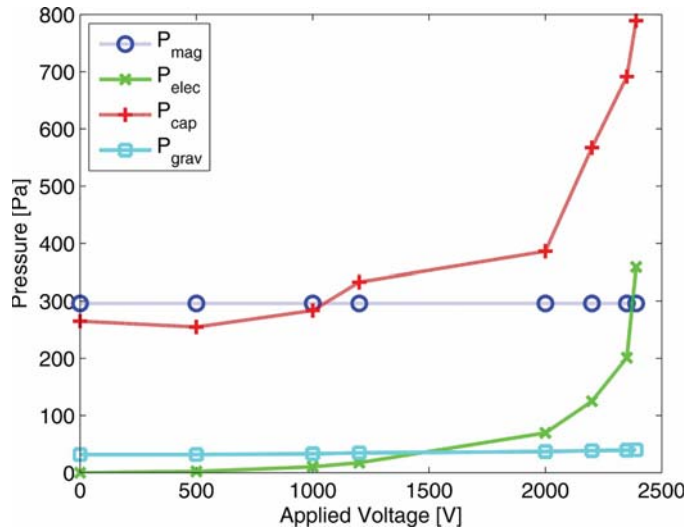


Figure 4.23: Pressure contributions from capillary, electric, magnetic and gravitational sources as the ILFF was stressed by an increasing applied voltage. Magnetic pressure, blue with open circles, was constant. Gravitational pressure, cyan with open squares, had a very small increase as the applied voltage was increased and the ILFF Rosensweig instability grew in height. Electric pressure, green with x's, increased because of the increase in applied voltage and the change in shape of the fluid. The electric field was determined by modeling the system in QuickField. The capillary pressure, red with crosses, increased as the ILFF Rosensweig instability tip radius decreased as the voltage was increased.

analytical form to estimate the electric field would be that it could be used to determine the onset of electrospray by determining where at what point the electric pressure ‘ran away’ or where it had a higher derivative than the capillary pressure. In the absence of an analytical method for predicting the electric field for the ILFF’s particular geometry, the finite element method could be used to predict the electric field at the tip, with a priori knowledge of the ILFF geometry. The downside to using this technique was that it was not predictive of how the electric field would be enhanced as the voltage was increased, thus it was not able to be used for predicting the onset of electrospray.

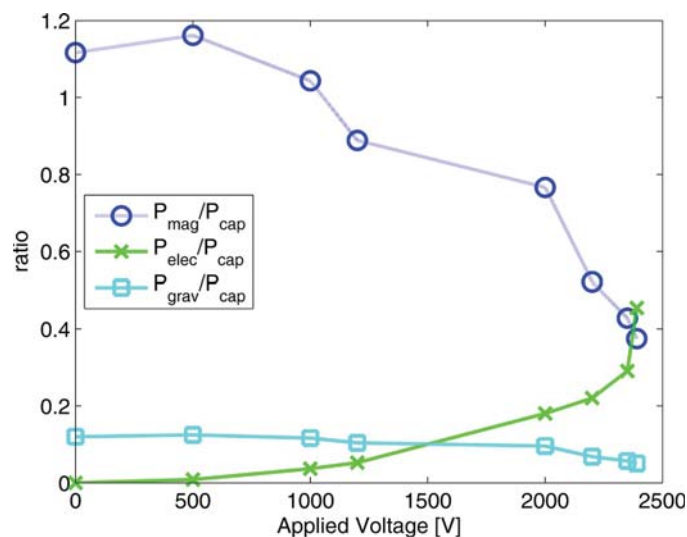


Figure 4.24: Ratio of magnetic pressure to capillary pressure and electric pressure to capillary pressure for start-up test 5 as the applied voltage was increased. Magnetic pressure to capillary pressure shown as the blue curve with open circles. Ratio of gravitational to capillary pressures is shown as, a cyan curve with open squares. The ratio of electric pressure to capillary pressure is displayed as, a green curve with x's. The electric field was determined by modeling the system in QuickField.

Comparing magnetic and capillary plus gravitational pressures near the onset of emission, the magnetic pressure was 35% of the capillary pressure. As the voltage was increased, both the capillary pressure and electric pressures increased meaning that the relative magnetic pressure contribution to the total magnetic pressure contribution decreased. This provided an upper bound on the amount the electrical pressure would need to be decreased to induce electrospray. Based on the electric field predictions, the electric field predicted by Equation 2.8 predicted an electric field stronger than was applied to the ILFF. If this electric field were to be used to predict the onset voltage, using Equations 2.8 and 2.9, it would predict a lower onset voltage than the system should have. Therefore comparing this onset

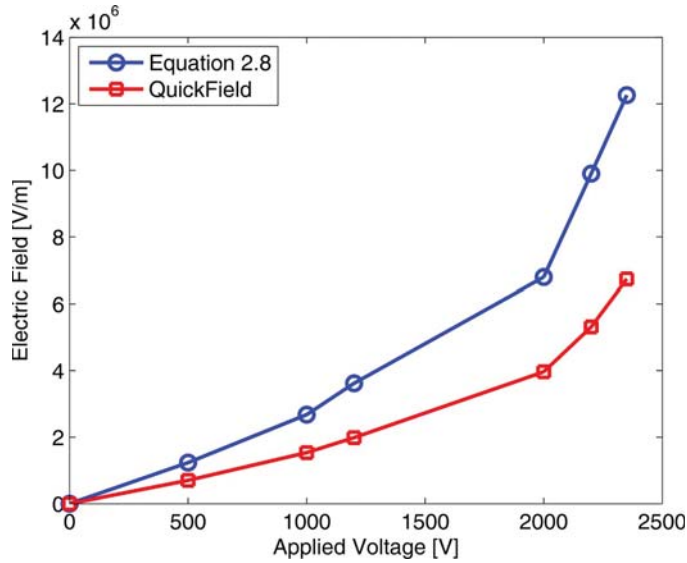


Figure 4.25: Comparison of electric field versus applied voltage for the data from Run 5. The blue curve with open circles represents the electric field calculated using Equation 2.8 and the tip radius and tip-to-electrode distance. The red curve with open squares represents the electric field calculated for the same data set using a finite element analysis tool, QuickField, and the shape of the ILFF at each respective voltage.

voltage to the actual onset voltage provided a lower bound on the magnetic contribution to the onset of electrospray. The data in Table 4.3 found the actual onset voltage was 16 to 24% lower than predicted by Equation 2.9. The reduction in onset voltage due to the magnetic contribution ranged was bounded to the range of 16% to 35%.

If an analytical model was developed that described the ILFF shape as a function of applied magnetic and electric fields, it could be used to predict the actual onset voltage using Equation 2.9. Similar types of models have been created by others for ferrofluids and ferrogels. There has been some work performed by Bohilus et al that has determined an amplitude equation for ferrofluids and ferrogels in uniform magnetic fields [51, 52].

This involved using non-linear techniques to describe the ferrohydrodynamic equations, compared to the linearized versions described in Section 2.3.2. Miller and Resler also developed a technique where they were able to describe the shape of a single Rosensweig instability in a uniform magnetic field. [25] In Section 2.4.4, the energy balance of an ILFF in a combined magnetic and electric field was presented. This energy balance could be used to describe the ILFF peak height and tip radius as a function of applied magnetic and electric fields, in a similar fashion used by Gailitis for Rosensweig instabilities [43].

4.5.3 Error Analysis of Measured Tip Radii and Tip-to-Extraction Electrode distances

There were sources of error when measuring the tip radii and tip-to-electrode distances. One of the sources of error was determining the locations in the images that corresponded to the fluid holder, the extraction electrode and the top of the peak. This error analysis determined the error in the repeatability of choosing a point in the image corresponding to a location, not the accuracy of the selected location to the actual location. The method used to determine the error was to take multiple samples of each of these locations, and then use statistical analysis to determine the error. The distance between the fluid holder and extraction electrode was known and fixed. To determine the tip-to-electrode distance, there were two back-to-back measurements taken. First, the location of the fluid holder in the focal plane was located in the image, along the edge of the annular trench. The second

location in the image was a point in the focal plane on the edge of the extraction and the annular hole in the extraction electrode directly above the ILFF. The last location marked in the image was the top of the peak in focus. The first two points marked, indicated the number of pixels in the image between the fluid holder and the extraction electrode, and was used as a scaling factor because this was a known distance. The second and third points marked indicated the pixels distance between the tip and extraction electrode.

The tip-to-electrode distance was found by multiplying the scaling factor (mm/pixel) from the first measurement, by the measured distance (in pixels) to yield a tip-to-electrode distance in millimeters. This measurement can be thought of as the multiplication of two random, dependent variables, where Z is the distance in millimeters, X is the scaling factor in mm/pixel, and Y is the measured tip-to-electrode distance in pixels, and this is given as

$$Z = XY. \tag{4.5}$$

The expected value, or mean, of the distance in millimeters, can be written as the expected value of product random variables, X and Y , or

$$E [Z] = E [XY]. \tag{4.6}$$

The variance of a random variable is the expected value of the square of the difference between the random variable and the mean of the random variable. When the random variable is the product of two dependent random variables, the resulting equation for the

variance is

$$\text{VAR}[Z] = E \left[(XY - E[XY])^2 \right]. \quad (4.7)$$

Finally, the standard deviation is the square root of the variance.

The important takeaway from Equations 4.5 - 4.7 was that the mean and standard deviation of the tip-to-electrode distance measurements (in millimeters) were to be taken on the final calculated value, and not the intermediate measured values. This same statistical process was used to determine the tip radii. The measurement error was defined to be one standard deviation. The errors for the tip-to-extraction electrode distances and tip radii were found to be in the range of 0.006 to 0.022 mm. The predicted starting voltages reported in Tables 4.4 used the mean of both the tip radii and tip-to-extraction electrode distances. Using the error of a single standard deviation, all of the predicted starting voltages were found to be within 2% of the stated values.

Chapter 5

Instability wavelengths of a ferrofluid in a non-uniform magnetic field

5.1 Introduction

The motivation of this chapter was to understand the peak-to-peak spacing of Rosensweig instabilities in a non-uniform magnetic field. This chapter reports on the results of studying the peak-to-peak spacing of Rosensweig instabilities in non-uniform magnetic fields by comparing experimental results to two different techniques proposed for the peak-to-peak spacing in non-uniform magnetic fields. This chapter is organized by first presenting the equipment used to perform these measurements, and the procedure used for data collection.

The experimental results are then compared to the body force method proposed by Rupp [53]. The experimental results are then compared to the technique used by Timonen et al [54]. This chapter was then concluded with a discussion of the results with the two analysis techniques.

In the first analysis technique, the peak-to-peak spacing was predicted using the gradient of the magnetic field. This technique substituted the magnetic moment force for the gravity force in the dispersion relation, Equation 2.21, yielding an expression for the peak-to-peak spacing, Equation 2.27. The second analysis technique presented in this work was comparing the dipole-dipole energy of numerous individual drops of ferrofluid to the magnetic moment energy. A Taylor expansion was taken on the auxiliary field in the magnetic moment energy term. Finding an expression for the minimum energy of the system yielded an expression relating the drop-to-drop spacing, or lattice constant for a given radial curvature of the magnetic field and ferrofluid magnetic moment, Equation 2.31. This second analysis technique used Equation 2.27 to define the greatest diameter than an individual ferrofluid drop could maintain. If the ferrofluid drop was larger than this value, it would split into two individual drops.

5.2 Equipment and Testing Methodologies

To achieve the goal of comparing measured Rosensweig instability peak-to-peak spacing in a non-uniform magnetic field by comparing these measurements to the two theories, there were a number of pieces of information needed. The first that was needed to be known was the fluid properties. All the experiments reported in this chapter used commercially available ferrofluid EFH-1 manufactured by FerroTec. A listing of the manufacturer's fluid properties was provided for reference in Table 5.1. The next piece of the puzzle was to provide non-uniform magnetic fields. This was accomplished by two different magnetic configurations. The first was a bar magnet and the second was a Halbach array, both described below in Sections 5.2.2 & 5.2.3, respectively. In order to know the non-uniformity and magnitude of the applied magnetic field, the field needed to be measured. To accomplish this, a GM-2 Gaussmeter was used, as described in Section 5.2.4. The locations of the Rosensweig instabilities were determined optically using the equipment and procedure outlined in Sections 5.2.5 & 5.2.6. Other methods of measuring ferrofluid surface profile were attempted such as laser profilometer, but were unsuccessful. White light interferometry was able to detect a peak or a valley, however, the white light interferometer on campus did not have enough field of view or depth of view to detect neighbouring peaks due to the distance and height differences between peaks.

5.2.1 Ferrofluid

Properties for a commercially available ferrofluid are listed in Table 5.1 for the ferrofluid EFH-1 produced by FerroTec. This ferrofluid was used for measuring the wavelengths of the Rosensweig instabilities in a non-uniform magnetic field. EFH-1 is a commercially available ferrofluid with the base fluid being a light hydrocarbon, and the magnetic nanoparticles are magnetite. All of the data collected and reported in Chapter 5 utilized EFH-1 ferrofluid from a 1000mL bottle with a lot number of M061213A.

Table 5.1
FerroTec EFH-1 Fluid Properties

Surface Tension, σ	29mN-m ⁻¹
Density, ρ	1210 kg-m ⁻³
Viscosity, $\mu_{viscosity}$	6 mPa-s
Relative Permeability, μ_r	2.6
Capillary Length, λ_c	9.8 mm
Magnetic Saturation, M_{sat}	$3.50 * 10^4$ A/m

5.2.2 Bar magnet

The bar magnet used was a stack of three bar magnets. Each magnet was a Neodymium grade N42 magnet with dimensions 152 mm by 3.18 mm by 7.84 mm (6 in by 1/8 in by 5/16 in) with the magnetization running through the 7.84 mm (5/16 in) dimension. The three stacked magnets had an overall dimension of 152 mm by 3.18 mm by 23.8 mm. A sketch of the magnet configuration is provided in Figure 5.1. The use of a long, thin magnet

was to reduce/eliminate the effects of the magnetic fields at the corners of the magnets.

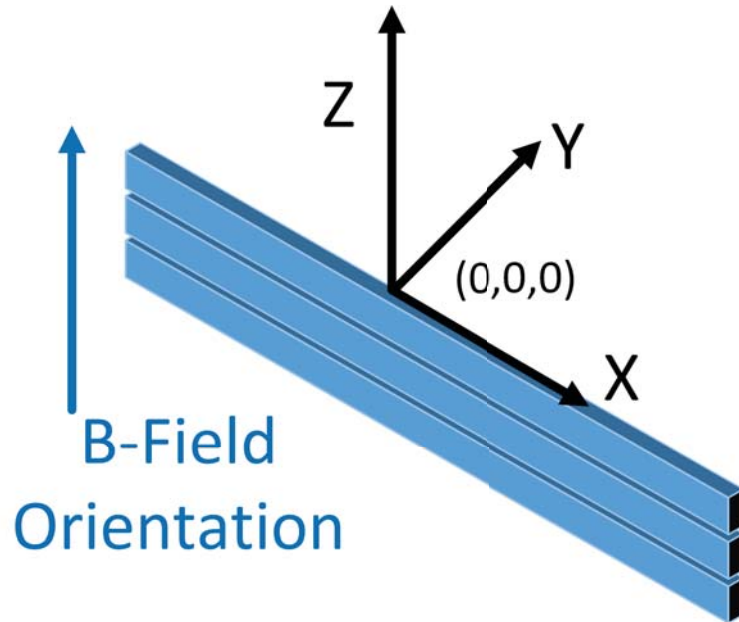


Figure 5.1: Illustration of stack of magnets, orientation of magnetization, and coordinates.

5.2.3 Halbach Array

The bar magnet described above in Section 5.2.2 proved to provide a good range of non-uniform magnetic fields. However, it was desired to provide a much ‘stronger’ (or much larger ∇B) non-uniform magnetic field. The proposed solution was to create a Halbach array with magnets of small physical dimension.

A Halbach array, as described here, is a linear array of magnets with each sequential magnet’s polarization rotated 90° . This results in a magnetic field roughly twice as strong

as a single magnet on one side of the array, and a negligible, almost non-existent magnetic field strength on the reverse side of the array. To create this array, seven Grade N42 3.18 mm by 3.18 mm by 25.4 mm (1/8 in by 1/8 in by 1 in) neodymium magnets (with their polarization through their 3.18 mm thickness) were arranged as a linear Halbach array and epoxied together in the orientation shown in Figure 5.2. The magnetic field measured on the centerline of a single of the magnets 0.52 mm above the magnet surface was 3200 Gauss. The same measurement performed on the Halbach array was found to be 6200 Gauss on the "top-side" and 800 Gauss on the "bottom-side" of the Halbach array.

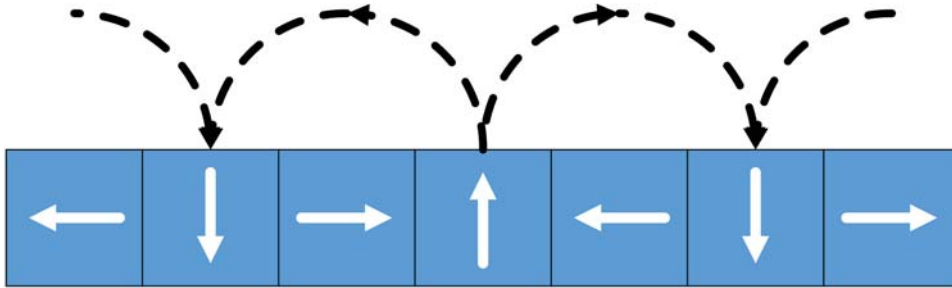


Figure 5.2: Illustration of a Halbach array.

5.2.4 Gauss Probe and the Mapping of the Magnetic Field

Magnetic fields were measured using an Alpha Labs GM-2 Gaussmeter with the ST transverse probe. The sensor on the probe was a single axis sensor with a sensing area of 0.25 mm by 0.25 mm. The probe was attached to an aluminum mount located on two orthogonal micro-positioning stages. The Gaussmeter could measure magnetic fields up to

30k Gauss with a stated accuracy within 2% of the reading.

In order to map the magnetic field of the bar magnet (Section 5.2.2) a zero point and orientation were first defined. The orientation of the grid was 'x' aligned along the 152 mm length with x_0 set to the midway point between the two ends, 'y' was aligned parallel the 3.18 mm thickness and y_0 was defined as the halfway point between the sides of the magnet, and finally 'z' was defined to run along the 23.8 mm height of the magnet stack with z_0 set as the top surface of the magnet. The orientation and origin of the axes are given in Figure 5.1. The magnetic field was found to be symmetric about x_0 and about y_0 , therefore only a single quadrant was required to be mapped. The grid for mapping the magnetic field was $x = 0$ mm to 50.8 mm in 25.4 mm steps, $y = 0$ mm to 3 mm in 0.5 mm steps, and $z = 3$ mm to 21.5 mm in 0.5 mm steps. At each grid point, both the B_y and B_z magnetic fields were measured and recorded. B_x was not recorded because the maximum B_x value measured in the grid was 10 Gauss, and was orders of magnitude smaller than either of the other values. Tables of the mapped magnetic field can be obtained in Appendix A. The magnetic field gradient $\nabla \vec{B}$ was taken as $\frac{dB}{dz}$, and was determined by numerically differentiating the measured magnetic field.

5.2.5 Camera and Lens

The camera system used for imaging the Rosensweig instability wavelengths was a Nikon D5000 camera with an AF-S Micro Nikkor 60-mm f/2.8G ED lens. This camera lens combination was placed on a tripod. Lighting was provided by a 150W Schott Ace Fiber Optic Light Source with a dual goose neck fiber optic light guide. Most ferrofluids, including the EFH-1 ferrofluid used in this experiment, are dark in color (brown to black) and highly reflective, with a specular dispersion instead of a diffuse dispersion. Indirect, diffuse lighting was found to be the most effective at imaging the ferrofluid and later determining the locations of the Rosensweig instabilities. This was accomplished by draping a white lab coat over the camera and ferrofluid and shining the fiber optic appendages of the light box onto the lab coat to provide indirect, diffuse lighting.

5.2.6 Rosensweig Instability Wavelength Setup and Measurement

An illustration of the setup and configuration of equipment used to measure the peak-to-peak spacing of the Rosensweig instabilities in a non-uniform magnetic field is given in Figure 5.3. In this illustration, the bar magnet was placed on a base plate, and it was secured in place with a thermoplastic adhesive. A vertical micro-positioning stage was also affixed to the baseplate with an aluminum sample holder. The aluminum sample

holder had markings drawn on it to provide a zero location and a scale for scaling each image taken with the camera. A 100-mm-diameter glass Petri dish containing roughly 1.6 mL (one dropper worth) of EFH-1 ferrofluid was then placed on the aluminum sample holder. The camera and lens were mounted in a vertical configuration so that they imaged the ferrofluid from directly above.

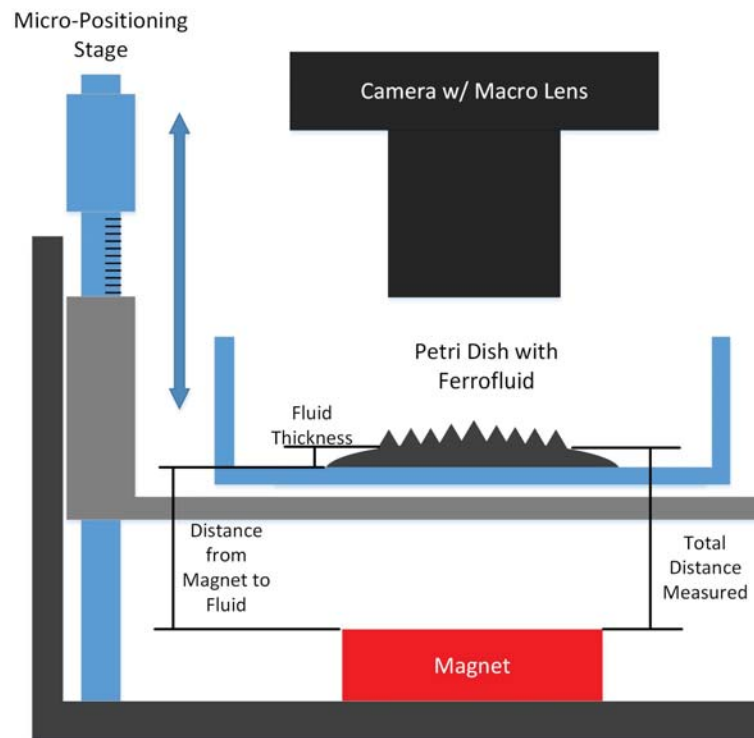


Figure 5.3: Illustration of Rosensweig instability wavelength measurement experimental setup.

The goal of using this setup was to place the ferrofluid in various, but known non-uniform magnetic fields, and then measure the peak-to-peak spacing of all of the Rosensweig instability locations. This was accomplished by changing the height of

the micro-positioning stage in 0.5 mm steps and imaging the ferrofluid. At each micro-positioning stage height step, a second image without the ferrofluid and Petri dish was taken of the calibration markings so the previous image could be scaled and orientated.

Post processing of images utilized MATLAB scripts. Each image taken of the peaks (leftmost image of Figure 5.4) would be accessed by MATLAB, where the user would locate and select in the image each of the peak locations. The resulting image with all of the peak locations marked can be viewed in the rightmost of Figure 5.4. The script would then open the corresponding calibration image where the user defined a vector which was used to position and scale the image of Rosensweig instability peaks. For comparison to the bar magnet, Figure 5.5 shows ferrofluid on the Halbach array. After all of the x- and y-positions of each peak was properly scaled and translated to that of the magnet, the script then determined the average distance between each peak and all of its nearest neighbors. For this analysis, nearest neighbor was defined as any peak within 135% of the closest peak. From the nearest neighbors, the peak-to-peak spacing for that peak was defined as the average distance to its nearest neighbors, and the error was defined as the standard deviation of that error. This analysis provided peak-to-peak spacing (and error) in (x,y,z) spatial coordinates, which were then correlated the local magnetic field properties.

The magnetization of the ferrofluid was calculated by assuming the applied magnetic field B_0 was roughly perpendicular to the bottom of the fluid. Across an interface the normal component of the B-field was constant, or $B_{0n} = B_{1n}$ where the 0 subscript denotes

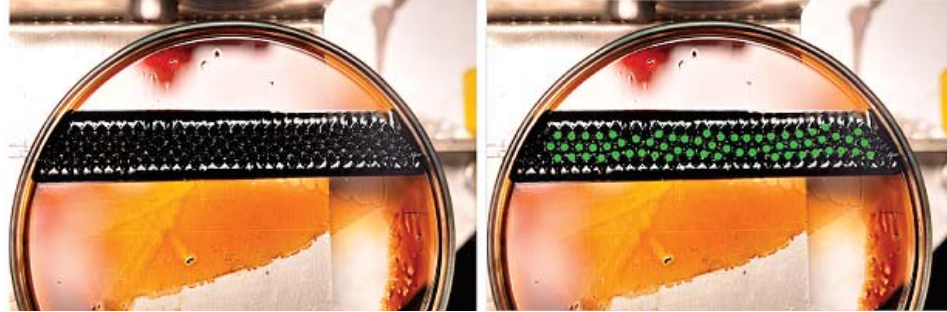


Figure 5.4: Left: Typical image of ferrofluid above bar magnet exhibiting Rosensweig instability. Right: Image from the left with peak locations selected (green dots).



Figure 5.5: Image of ferrofluid on a linear Halbach array. The length of each individual magnet was 25.4 mm.

vacuum, and 1 denotes the ferrofluid. Internal to the fluid the constitutive relations can be written as $B_1 = \mu_0 \mu_r H_1$ or $B_1 = \mu_0 (H_1 + M_1)$. Re-arranging and substituting in the two versions on the constitutive relations for H_1 and solving for the magnetization, M , yields

$$M = \frac{1 - \frac{1}{\mu_r}}{\mu_0} B_0. \quad (5.1)$$

This relates the magnetization of the fluid to the applied magnetic field. Accounting for the saturation magnetic field, the magnetization was taken to be the smaller value of Equation 5.1 and the saturation magnetization, M_{sat} , which was given in Table 5.1.

5.3 Peak-to-peak Spacing of Rosensweig Instabilities in Non-Uniform Magnetic Field

The analysis of the results of this chapter were broken into two sections. The first section evaluates the experimental peak-to-peak spacing of Rosensweig instabilities in a non-uniform magnetic field using a body force method proposed by Rupp [53], and discussed in the first part of Section 2.3.3. The second part of this analysis uses the same experimentally obtained data and analysed them using the energy method used by Timonen [54], and was discussed in the later part of Section 2.3.3.

5.3.1 A Body Force Approach to Analysing Peak-to-Peak Spacing of Rosensweig Instabilities in a Non-Uniform Magnetic Field

The first method used to analyse the peak-to-peak spacing of the Rosensweig instabilities in a non-uniform magnetic field was the technique of substituting a magnetic gradient body force into the dispersion relation (Equation 2.21). This resulted in a prediction for the peak-to-peak spacing in Equation 2.27.

The peak-to-peak predicted by Rupp [53] using Equation 2.27 was plotted as a thick black line in the log-log figure below, Figure 5.6. The thin rightmost vertical line denotes where the magnetic gradient body force was 10 times greater than the gravity force, while the leftmost vertical line denotes when they were equal. Using this analysis, only the data to the right of the rightmost vertical line should be considered when comparing the experimental data to the predicted peak-to-peak spacing because to the left of this line, it was unknown how much gravity influenced the results.

First, all the data collected and presented in Figure 5.6 were in a location of the magnetic field where the magnetic gradient force was stronger than the gravity force. Second, all the data displayed a peak-to-peak spacing smaller than the capillary length of the fluid. This result was consistent with previous observations. The Halbach array was able to produce a magnetic gradient body force an order of magnitude greater than that of the bar magnet. The

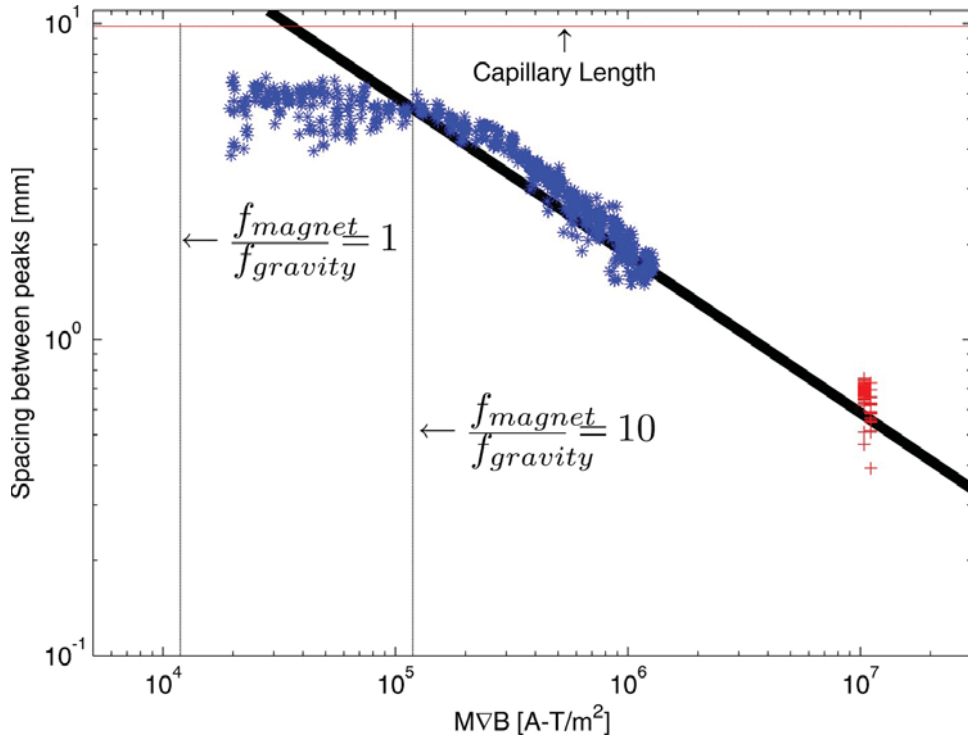


Figure 5.6: Plot of measured peak-to-peak spacing versus $M\nabla B$ of FerroTec EFH-1 ferrofluid. The thick black line denotes the peak-to-peak spacing predicted by Equation 2.27. The blue ‘*’ denotes the peak-to-peak spacings measured of the ferrofluid with the magnetic field supplied by the bar magnet described in Section 5.2.2. The red ‘+’ denotes the peak-to-peak spacings of the ferrofluid above the Halbach array described in Section 5.2.3. The rightmost thin black vertical line (at $\sim 1.2 \times 10^5 \text{ A} - \text{T}/\text{m}^2$) is where the magnetic body force is an order of magnitude stronger than the gravity body force, and the leftmost vertical line (at $\sim 1.2 \times 10^4 \text{ A} - \text{T}/\text{m}^2$) indicates where the two forces are equal.

measured peak-to-peak spacings measured using the Halbach array ranged from 0.39 mm to 0.75 mm, while the bar magnet was only able to produce peaks with peak-to-peak spacing as small as 1.4 mm. The percent difference between the measured peak-to-peak spacing and the peak-to-peak spacing predicted by Equation 2.27 is shown below in Figure 5.7. For all of the measured peak-to-peak values where the magnetic gradient force was dominant

(all data where $f_{magnet} > 10f_{gravity}$ in Figures 5.6 & 5.7), the measured value was within $\pm 50\%$ of the predicted value, which corresponds to prediction value within 1 mm of the measured value. The percent error appears to be less than $\pm 20\%$ near $1 \times 10^5 \text{ A} - \text{T}/\text{m}^2$ and $1 \times 10^6 \text{ A} - \text{T}/\text{m}^2$, while around $5 \times 10^6 \text{ A} - \text{T}/\text{m}^2$, the percent error between measured and predicted resides primarily in the 20% – 40% range.

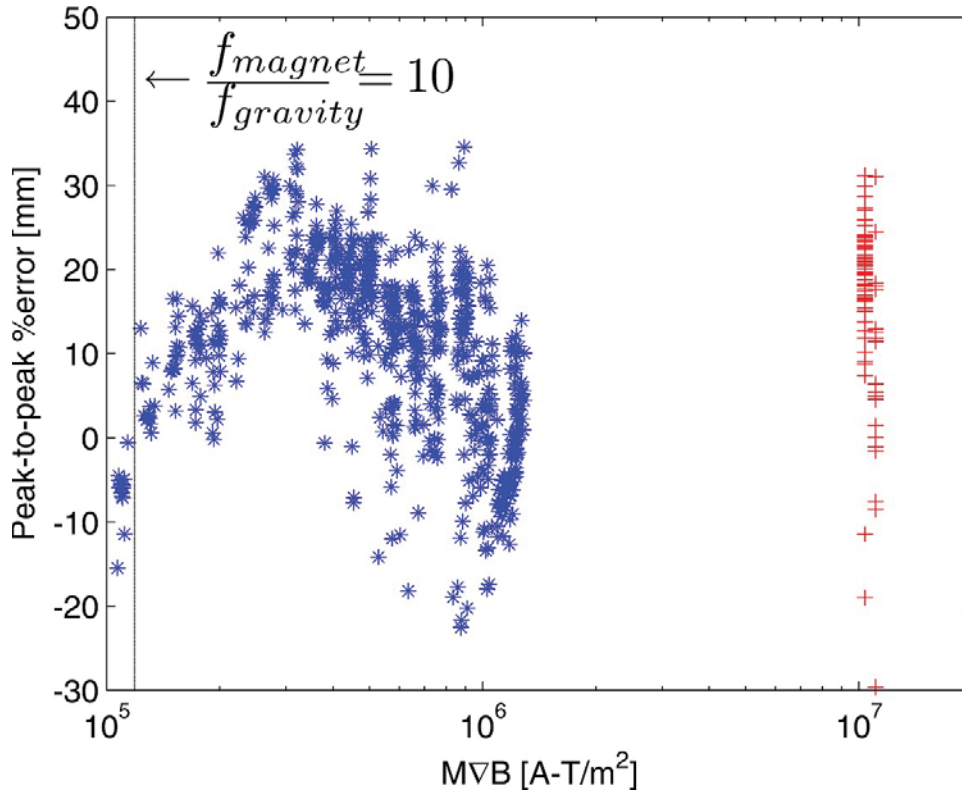


Figure 5.7: Plot of the percent difference between measured peak-to-peak values and the peak-to-peak values predicted by Equation 2.27. Similar to Figure 5.6, blue ‘*’ denotes measured values using bar magnet, and red ‘+’ denotes measured peak-to-peak spacing using Halbach array.

The changes in the percent error of the measured peak-to-peak spacing to the predicted spacing could be attributed to how this distance was defined. The wavelength of these

instabilities should be the distance between their bases, measured along the arc length of the curve between the centers of the instabilities. Because ferrofluid was highly reflective, but specularly reflective, the surface profiles of the ferrofluid were not able to be mapped by techniques such as laser profilometer or white light interferometry. Instead top-down photographs of the ferrofluid were taken with diffuse light. The only feature of the ferrofluid that was reliably detected with this method was the Rosensweig instability peaks. If all of the peaks were orientated in the same direction, the peak-to-peak distances should match the wavelength of the Rosensweig instabilities. However, in the non-uniform magnetic field of the bar magnet, the ferrofluid tends to pool up along the center-line of the y-axis, creating a shape that looks similar to a speed bump on a road, see Figure 5.8 for an illustration of this. The Rosensweig instabilities that were formed, formed normal to this fluid surface. Some of the peaks formed pointing directly up, others up to the left, and some were up and to the right.

From observations during data collection, the ferrofluid was the most curved when the ferrofluid was closest to the magnet, or when $M\nabla B$ was high, and flattest when very far from the magnet, or lower $M\nabla B$. When the ferrofluid was most curved (near that bar magnet and high $M\nabla B$), the peak-to-peak spacings were small and each of the peak heights were small. Because the peak heights were small, the error between wavelength and the peak-to-peak spacing was likely low. This would explain why there was (relatively) lower error with the bar magnet at high $M\nabla B$, such as when $M\nabla B \approx 10^6 \text{ A} - \text{T}/\text{m}^2$. As the ferrofluid was moved farther from the bar magnet, the peak height grew greater in height

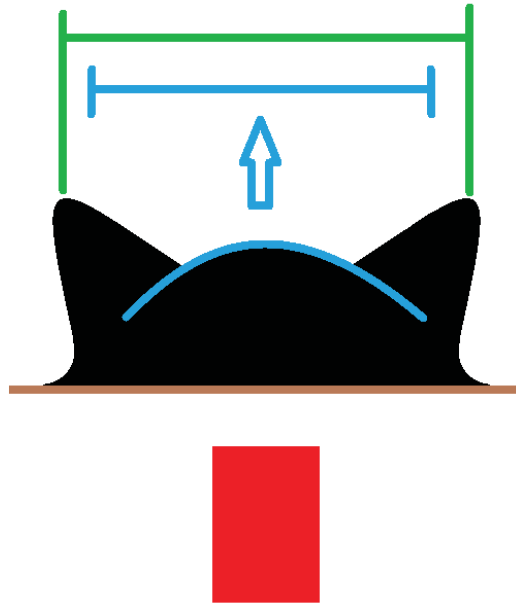


Figure 5.8: Illustration showing two methods of defining peak-to-peak spacing of a ferrofluid where the Rosensweig instabilities formed on a curved fluid surface. The curved black mass was a ferrofluid, and the thin brown line was the substrate the ferrofluid sits on, and the red rectangle represented the magnet below the ferrofluid. The blue lines represented the peak-to-peak measurement used in this dissertation. The green lines represented a peak-to-peak measurement at the base of the peaks.

and the ferrofluid curvature slowly flattened. As the Rosensweig instabilities grew in height, the difference between the wavelength and peak-to-peak spacing could have grown, with the peak-to-peak spacing measuring a larger distance than the actual wavelength. This could be a reason for the greater difference between the predicted wavelength and measured peak-to-peak spacing in the range of $2 * 10^5 \leq M \nabla B \leq 7 * 10^5 A - T/m^2$. At distances even greater from the bar magnet (low $M \nabla B$), the ferrofluid ‘speed bump’ disappeared all together, and the ferrofluid peaks all pointed directly up, and thus there should have

been no difference between the wavelength and the peak-to-peak spacing. This may explain why the error between the peak-to-peak spacing and predicted wavelength when $M\nabla B \approx 10^5 A - T/m^2$ reduced back down to the 20% range.

Another possible reason for disagreement between the measured data and the analysis technique could have been the limitations with the analysis technique. The analysis technique was based upon inserting a non-uniform magnetic field term into a dispersion relation, Equation 2.21, that was derived assuming the applied magnetic field was uniform. For an analysis technique that was formed by violating one of the assumptions in the derivation of the original equations, the analysis technique was able to predict the peak-to-peak spacing within 20 to 40% of the measured values.

For the data in Figure 5.6 where the magnetic gradient force was dominant, the measured peak-to-peak spacing match closely with the predicted peak-to-peak spacing, with an error less than 1 mm. The peak-to-peak spacing was a function of the fluid's magnetic (M) and the vertical gradient of the applied magnetic field ($\frac{dB}{dz}$). Increasing a fluid's magnetic saturation, M_{sat} would be one method that could decrease peak-to-peak spacing. Another method would be to increase the strength of the magnetic field so that the fluid reaches magnetic saturation quicker, and/or increase the gradient of the magnetic field. The magnetic gradient has two ways in which it could be increased. First, for a given geometry, a stronger magnet would have a higher gradient. The second way to increase the magnetic gradient would be to use a geometry that increased divergence of the magnetic field. One way this could be

accomplished would be using physically small magnets. For a magnet with a large surface area, the majority of the magnetic flux lines near the center of the area would be uniform so the ∇B would result primarily from the decay due to the distance from the magnet. However, with a magnet with a small surface area, such as those described in the Halbach array, the magnetic flux lines coming out of the magnet surface begin wrapping back around the magnet very quickly, and the divergence of the magnetic field was much greater.

5.3.2 An Energy Approach to Analysing Peak-to-Peak Spacing of Rosensweig Instabilities in a Non-Uniform Magnetic Field

This section serves to compare the energy-based analysis technique used by Timonen et al [54] to the collected experimental peak-to-peak spacing data. The concept of this approach was that the curvature ($\frac{d^2H}{dr^2}$) of the magnetic field was responsible for the lattice spacing of the ferrofluid drops. In the work and analysis by Timonen et al, the ferrofluid was placed on a superhydrophobic surface. Once a large number of droplets was created, each droplet acted as a self-contained unit that was unable to transfer fluid from one droplet to another. The maximum width of the droplet was set by the same critical wavelength used in the previous analysis, Equation 2.27. Once that criterion was met, the array spacing was found to be proportional to an array factor, Equation 2.31.

The peak-to-peak spacing data presented in this dissertation were collected under different

conditions than Timonen et al used. An illustration of the differences between the connected peaks presented in this work the drops that this analysis technique used can be viewed in Figure 5.9. The main difference was in all the data presented in this dissertation, all of the ferrofluid peaks were connected. This had the consequence that there were not drops with discrete magnetic moments. This allowed each of the peaks of ferrofluid to constantly change volume. The volume of each of the ferrofluid peaks was unknown because the peak height data was not measured and recorded. However, during testing, the peak height appeared to correspond with the peak diameter. The peak heights appeared to be roughly the same length as the peak based diameters. Using this approximate knowledge, and assuming each peak was roughly a cone in shape the volume of each peak was estimated. The height of each cone was assumed to be equal to the peak-to-peak distance for that peak, and the cone radius was 1/2 the measured peak-to-peak distance. Using these assumptions, the volumes of the peaks were estimated using

$$V = \frac{1}{12}\pi r^3. \quad (5.2)$$

The magnetic moment was a function of magnetization and volume, or $m = MV$.

The peak-to-peak spacing data in known magnetic fields that was analysed in the previous section, Section 5.3.1, was analysed using the energy method described above, namely Equation 2.31. The data analysed with Equation 2.31 are presented in Figure 5.10. The fit to the data in Figure 5.10 was a slope of 2.55 mm/mm with an intercept of -0.48 mm.

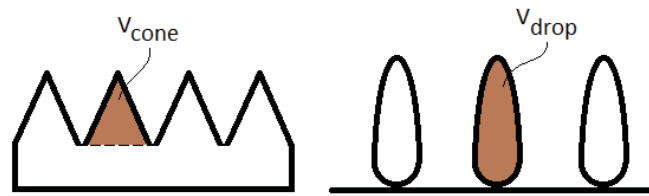


Figure 5.9: Left: Connected ferrofluid peaks created by the Rosensweig instability, as described in the work presented in this dissertation. Fluid volume estimated by assuming it was a cone shape. The shaded portion of the illustration was the what was considered a peak for the analysis. Right: Ferrofluid drop as described by Timonen et al on a superhydrophobic surface. The shaded portion of the drop (the whole drop) was used to determine the drop volume.

Based on the residuals of the fit, at least 50% of the data fell within ± 0.41 mm of the fit line.

This technique was not able to predict the peak-to-peak spacing. If this technique was able to predict the peak-to-peak spacing, the lattice constant would be equal to the peak-to-peak spacing. This was not the case. For instance, for $(m/c)^{1/5} = 2$ mm in Figure 5.10, corresponds to measured peak-to-peak spacings between 4 and 5.5 mm. For this technique to truly be predictive, the number of peaks, their relative location to each other, and the volume of each peak must be known to predict the lattice spacing. The lattice spacing in Equation 2.31 was only proportional to and not equal to because the analysis by Timonen et al ignored terms that would have been present if they would have accounted for the summations over every drop and its location in Equation 2.29. Instead these were ignored. This technique, by its nature can be used to describe an existing system with a known curvature of magnetic field, and a lattice configuration which retains a constant number

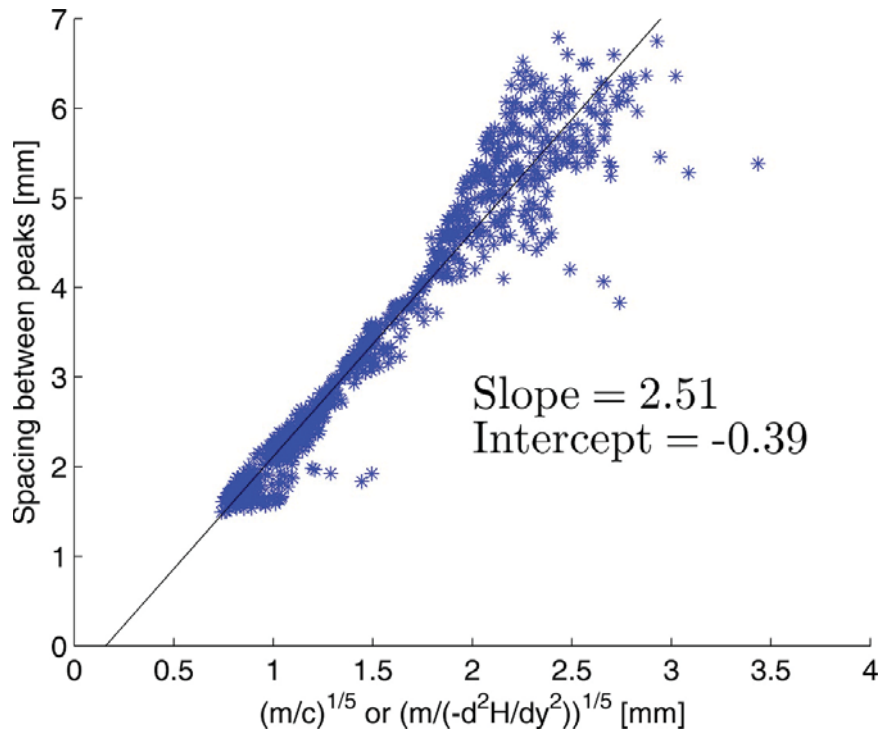


Figure 5.10: Measured peak-to-peak spacing versus the fifth root of the magnetic moment over the second derivative of the magnetic field. The blue ‘*’ denotes measured values, and the black line denotes a linear fit to the data.

of elements and each element maintains its relative position to the other elements. This technique will describe how the drop-to-drop or peak-to-peak spacing will vary with a known system. This analysis technique, however, does not lend itself well to designing a new system without first constructing the system.

5.4 Discussion of Results

The goal of this chapter was to compare experimental data on the peak-to-peak spacing of Rosensweig instabilities in non-uniform magnetic fields to two analytical methods that have either been hypothesized or used. A commercially available ferrofluid was imaged in various known, non-uniform magnetic fields and the peak-to-peaks spacings were measured. These data were compared to a prediction of wavelength proposed by Rupp [53] based on replacing the gravitational force with a magnetic gradient force in the Rosensweig instability dispersion relation. This model was found to predict the peak-to-peak spacing of the instabilities within $\pm 40\%$ of the measured value. The difference between the measured values and the predicted values could be from two sources. First, the model may not fully encompass the underlying physics. The model was created by substituting in a non-uniform magnetic field term into a dispersion relation, which was derived with the assumption that the applied magnetic field was uniform. Second, there could be error in the measurement of the peak-to-peak spacing or correlating the peak location to the local magnetic field environment. The model, however, was able to roughly predict the peak-to-peak spacing of Rosensweig instabilities with peak-to-peak spacing ranging from 0.39 mm to 5 mm .

The peak-to-peak spacing data was compared to a second model by Timonen [54] that minimized the magnetic energy of the ferrofluid and the energy of the curvature of the magnetic field to determine a lattice spacing (or wavelength). Using this energy-based

technique required knowledge, and in the case of the data from this dissertation, numerous assumptions, of the state of the Rosensweig instabilities after they were formed. The data were found to, roughly, fall onto a line which could be used to predict peak-to-peak spacing when the same configuration was to be used. One of the downfalls of this technique if it were to be used to design a device, it would require information about the configuration (number of peaks, volume of peaks, configuration of peaks) before any predictions about peak-to-peak spacing could be made. The second problem of attempting to use this technique was that it assumed each peak was an individual, isolated entity, and that the number and configuration of peaks would remain constant and only the spacing between the individual peaks would vary. In the data collected in this dissertation, neither of those assumptions were correct. Between every configuration in the data collected in this dissertation, the number of peaks and the volume of each peak could (and did) vary..

For a discontinuous fluid, i.e. individual drops, the maximum size of a droplet was set by Equation 2.27, and the drop-to-drop, or lattice, spacing must be greater than this value. However, for a continuous fluid the peak-to-peak spacing was found to be determined by Equation 2.27, as confirmed in Section 5.3.1. An illustration of the difference between these two cases is provided in Figure 5.11. In the left of the figure, the peak-to-peak spacing and the size of the peaks were both determined by Equation 2.27, or the gradient of the magnetic field. The right of Figure 5.11, depicted a discontinuous fluid. In this case, the size of the peak was limited to be no larger than the value set by Equation 2.27. If the peak, or drop, became larger than this value, it would split into two drops. The peak-to-peak, or

drop-to-drop, spacing in this case was dictated by the curvature of the magnetic field, or Equation 2.31. For a continuous ferrofluid, the peak-to-peak spacings should be predicted by Equation 2.27. And a discontinuous ferrofluid in a non-uniform magnetic field should have the drop-to-drop spacing predicted by Equation 2.31.

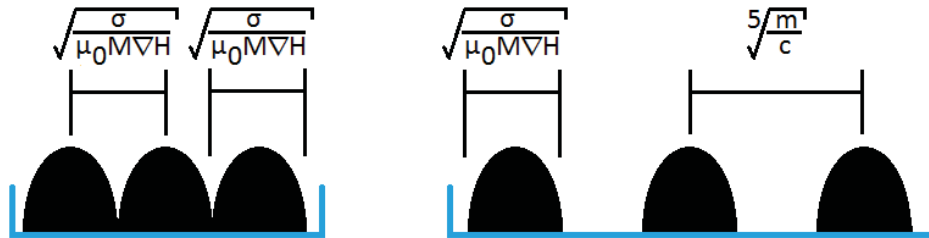


Figure 5.11: Depiction of peak-to-peak spacing for a continuous ferrofluid and discontinuous ferrofluid. Left: In a ferrofluid where all of the peaks are connected, the peak size can change, and the peak diameter and peak-to-peak distance was governed by Equation 2.27. Right: Individual ferrofluid drops in a non-uniform magnetic field. The maximum diameter of the drop was confined to be no larger than the value provided in Equation 2.27, while the peak-to-peak spacing was set by Equation 2.31

Chapter 6

Conclusion

6.1 Introduction

The goals of this work were: 1) demonstrate electro spray using an ionic liquid ferrofluid in a combined electric and magnetic fields, where the magnetic field formed the emission sites, 2) measure the I-V characteristics of the ILFF-based electro spray source, 3) measure the onset voltage which caused ion and/or droplet emission from the ILFF and compare the measured voltage to the predicted voltage from theory, 4) study how the spacing of Rosensweig instabilities was influenced by a non-uniform magnetic field and how those results compared to two predictions. This chapter summarises the results and conclusions obtained in Chapters 4 & 5. This work concludes with suggestion for improvements on this

work and ideas to expand on the work presented in this dissertation.

6.2 Summary of Experimental Results

It was shown that Rosensweig instabilities created using an ILFF and stressed by an electric field can be used to create an electrospray source. This was demonstrated with two different ILFFs, the first was based of the ionic liquid EAN (batch # NJ397007), and the second was based off the ionic liquid EMIM-NTf₂ (batch # NJ397028). Current-voltage data was collected for both batches of ILFF. The EMIM-NTf₂ based ILFF (batch # NJ397028) yielded a much higher current when emitting negative ions and/or droplets than when emitting positive ions and/or droplets, even at the same extraction voltage. Using the current collector (ITO glass) as a witness plate, it was found that the magnetic nanoparticles are being emitted along with the ionic liquid.

The ILFF electrospray source was observed to self repair. One of the major obstacles for long lifetime of electrospray sources is damage to the underlying structure supporting the liquid. The ILFF electrospray source incurred damage during emission (a large bubble formed in one of the peaks), and within minutes, the bubble burst, the tip reformed, and began to re-emit ions. This showed that the tips are effectively indestructible to many of the common failure mechanisms, such as arcing, mechanical deformation, and tip damage.

During electrospray, it was also observed that the tip of the peak could separate into multiple tips, creating multiple emission sites. The actual cause of this phenomenon was not discovered. This phenomenon was primarily discovered at higher spray currents. It could be the electric field was strong enough to cause multiple emission sites per tip to form, or the multi-tip mode was a preferable, lower energy configuration.

The onset voltage, or the voltage where emission began, for an electrospray source was studied. It was found that the ILFF based electrospray source described in Chapter 4 had an onset voltage 16% to 24% lower than predicted by Equation 2.9 when the tip radius and tip-to-electrode distance were measured with no applied electric field. Two techniques were used to predict the electric field at the tip. The two techniques bounded the electric field, with one under predicting the electric field, and the other over predicting. The magnetic contribution should provide a reduction in the required applied voltage to obtain electrospray.

The second part of this work was a study of ferrofluids and the way their peak-to-peak spacing changed in non-uniform magnetic fields, compared to uniform magnetic fields. There were two motivations to work. The first was a fundamental curiosity because peak-to-peak spacing measurements have not been taken before on a continuous ferrofluid in a non-uniform magnetic field. The second reason was to determine the packing density of electrospray sources for the application of electrospray thrusters. In the case of electrospray thrusters, there is a desire to have lots (1000's) of emitters in a small footprint (10's

of cm^2). Rosensweig instabilities created by the application of uniform magnetic fields have been studied in depth on a number of fronts, from the peak-to-peak spacing, to the lattice structure, to dynamic response of the fluid. But to date, only one other study had been performed on ferrofluid in a non-uniform magnetic field. That study was recently performed, but was done for individual ferrofluid drops on a superhydrophobic surface.

The first approach used for predicting the peak-to-peak spacing of the ferrofluid in a non-uniform magnetic field was a body force method. This method compared the body force of gravity to the body force of the magnetic gradient. Where the magnetic gradient body force was an order of magnitude or larger than the gravity body force, it was substituted into the dispersion relation in a uniform magnetic field, Equation 2.21, for the gravity body force term. Using this, an equation was derived to predict the peak-to-peak spacing for ferrofluids in a non-uniform magnetic field. This was then compared against actual measured peak-to-peak spacings in a ferrofluid with various applied non-uniform magnetic fields. Where the magnetic gradient body force was an order of magnitude or stronger than the gravity body force, it was found that there was good agreement between the predicted values and the measured values. Also, in order to minimize the peak-to-peak spacing, one would want a ferrofluid with the highest saturation magnetic field (M_{sat}), and the highest gradient of the magnetic field ($\frac{dB}{dz}$), which would tend towards magnets with small widths, or magnet configurations where the magnetic gradient is very strong, such as Halbach arrays. Using this technique to analyse the measured data, the technique was found to predict the peak-to-peak spacings with an error ranging from 20% to 40%. Some

of this error was attributed to how the peak-to-peak spacing was measured compared to how a wavelength was defined.

The second approach used for predicting the peak-to-peak spacings of Rosensweig instabilities of a ferrofluid in a non-uniform magnetic field minimized the dipole-dipole and dipole moment energies. Using this method to analyse the measured data did not yield predictive results. The best this technique was able to do was describe the measured peak-to-peak values, but not predict a new system.

The second approach, however, assumed that the droplet diameter had an upper bound set by Equation 2.27, which was the peak-to-peak spacing predicted by Rupp. It is proposed that for a continuous fluid, the peak-to-peak spacing will default to the value given by Equation 2.27 because the volume of the connected peaks was allowed to vary, unlike the case of the discontinuous peaks. The energy based analysis of the second approach is valid for a continuous ferrofluid as it does describe the measured peak-to-peak values, but the predicted peak-to-peak spacings proposed by Rupp were found to predict the measured peak-to-peak values within 20 to 40%.

6.3 Improvements and Future Work

One of the first areas of further exploration from this work is determining what gets emitted and in what ratios. From the witness plates, and quadrupole mass spectrometry (not presented in this work), it is apparent that the magnetic nanoparticles were emitted along with the ions from the ILFF. Knowing the emission characteristics is an important factor in thruster design. First and foremost, it is important to know if the mass fraction of magnetic nanoparticles in the ILFF of the bulk fluid stays constant, or increases or decreases. If the concentration of magnetic nanoparticles varies over time, then the ILFF's fluid properties may change, and affect the behavior of the fluid. Second, knowing the charge to mass and particle make-up will provide key parameters in determining thruster performance and operational characteristics such as thrust to power (T/P), specific impulse (I_{SP}), and mass flow rate, where specific impulse and thrust to power are defined in Equation 2.14 and Equation 2.12, respectively.

Another question posed by this work was whether the electrically charged magnetic particles travelling through a magnetic field will affect the beam pattern. It is possible that the external magnetic could expand or contract the beam width. The Lamor radius

$$r_L = \frac{v}{\omega_c} = \frac{Vm}{qB}, \quad (6.1)$$

of the emitted ion/charged droplet is a function of the particle velocity and cyclotron frequency

$$\omega_c = \frac{qB}{m}. \quad (6.2)$$

When first emitted from the emission site, the velocity is very low, and the magnetic field is strong, meaning the Lamor radius is small. As the particle approaches the extraction electrode, the particle increases in velocity, and the magnetic field strength decreases as well, both of these resulting in a larger Lamor radius. Another force that could modify the beam would be the magnetic moment force, or Kelvin force. A magnetic moment, such as a charged drop of ILFF is attracted to a strong gradient in the magnetic field, such as the strong gradient along the centerline of a permanent magnet. This force could help focus to beam to a narrower beam width. It is currently unknown if these effects, or others such as the grad-B drift would modify the beam pattern of the ILFF. Also, it may be that the externally applied magnetic field could help reduce droplet breakup (Rayleigh-Taylor instabilities) in the beam, similar to how they were suppressed with a rotating magnetic field by Rennacher and Engel. [100]

Finally, one of the areas for ILFF emission that needs to be addressed is the stabilization of the emission current. It was seen with the EAN-based ILFF that the emission current was fairly steady, but the EAN-based ILFF had some undesirable characteristics for in-space electrospray. The EMIM-NTf2-based ILFF had much more variance in the emitted current.

From the data in this work, it would appear that viscosity plays an important role in emission stability, but there could also be other factors, and fluid properties that are important as well.

6.4 Conclusion

Electrospray thrusters are still a maturing technology, with much research going into many facets of their design and implementation. Much of the current work is going into the manufacturing processes to create the solid substrates that support the propellant, reducing emitter-to-emitter spacing, and increasing emitter lifetime and reducing emitter susceptibility to damage. This work has demonstrated that many of the challenges with electrospray can be overcome using ionic liquid ferrofluids to generate emission sites in situ. These emission sites have shown to be able to regenerate after being damaged. The fact that the emission sites form out of the fluid means that there is no need for the delicate and timely manufacturing that current state of the art electrospray thrusters require. Furthermore, this work explored the scaling laws of ferrofluids and how the fluid properties and the magnetic field profile can reduce peak-to-peak spacing, increasing emission site density.

References

- [1] B. Gassend, Luis Fernando Velásquez-García, A.I. Akinwande, and Manuel Martínez-Sánchez. A Fully Integrated Microfabricated Externally Wetted Electro spray Thruster. In *43rd AIAA/ASME/SAE/ASEE Joint Propulsion Conference, Cincinnati, OH, July 8-11, 2007, AIAA2007-5182*.

- [2] Natalya Brikner and P. Lozano. The role of upstream distal electrodes in mitigating electrochemical degradation of ionic liquid ion sources. *Applied Physics Letters*, 101(193504), 2012.

- [3] G. Taylor. Disintegration of Water Drops in an Electric Field. *Proceedings of the Royal Society of London*, 280(1382):383–397, 1964.

- [4] J. Zeleny. The Electrical Discharge from Liquid Points, and a Hydrostatic Method of Measuring the Electric Intensity at their Surfaces. *Physical Review*, 3(2):69–91, 1914.

- [5] P.D. Prewett and G.L.R Mair. *Focused Ion Beams from Liquid Metal Ion Sources*. Research Studies Press LTD., Somerset, England, 1991.
- [6] R. Krpoun and H.R. Shea. A method to determine the onset voltage of single and arrays of electrospray emitters. *Journal of Applied Physics*, 104:064511, 2008.
- [7] H. Schaub and J.L. Junkins. *Analytical Mechanics of Space Systems*. American Institute of Aeronautics and Astronautics, Reston, VA, 2003.
- [8] M. Tajmar. Overview of Indium LMIS for the NASA-MMS Mission and its Suitability for an In-FEEP Thruster on LIS. In *32nd International Electric Propulsion Conference, Wiesbaden, Germany, September 2011, IEPC-2011-009*.
- [9] Paulo Lozano. *Studies on the Ion-Droplet Mixed Regime in Colloid Thrusters*. PhD thesis, MIT, 2003.
- [10] Y. Chiu, B.L. Austin, and R.A. Dressler. Mass Spectrometric Analysis of Colloid Thruster Ion Emission from Selected Propellants. *Journal of Propulsion and Power*, 21(3):416–423, 2005.
- [11] B.W. Ticknor, S.W. Miller, and Y. Chiu. Mass Spectrometric Analysis of the Electrospray Plume from an Externally Wetted Tungsten Ribbon Emitter. In *46th AIAA/ASME/ASEE Joint Propulsion Conference and Exhibit, 2-5 August 2009, Denver, CO*. 2009.

- [12] J. Ziemer. Performance of Electrospray Thrusters. In *31st International Electric Propulsion Conference, Ann Arbor, MI, September 2009, IEPC-2009-242*.
- [13] M. Gamero-Castaño and V. Hruby. Characterization of a Colloid Thruster Performing in the micro-Newton Thrust Range. In *27th International Electric Propulsion Conference, Pasadena, CA, October 2001, IEPC-01-282*. 2001.
- [14] C. Scharlemann, M. Tajmar, I. Vasiljevich, N. Buldrini, D. Krejci, and B. Seifert. Propulsion for Nanosatellites. In *32nd International Electric Propulsion Conference, Wiesbaden, Germany, September 2011, IEPC-2011-171*.
- [15] R.S. Legge, P. Lozano, and M. Martinez-Sanchez. Fabrication and Characterization of Porous Metal Emitters for Electrospray Thrusters. In *30th International Electric Propulsion Conference, Florence, Italy, September 2007, IEPC-2007-145*.
- [16] R.S. Legge and P. Lozano. Maximizing One-Dimensional Porous Emitter Packing Density for Electrospray Applications.
- [17] D.G. Courtney, H.Q. Li, and P. Lozano. Electrochemical Micromachining on Porous Nickel for Arrays of Electrospray Ion Emitters. *Journal of Microelectromechanical Systems*, 22(2):471–182, 2013.
- [18] H.Q. Li, D.G. Courtney, P. Diaz Gomez Maqueo, and P. Lozano. Fabrication and Testing of an Ionic Electrospray Propulsion System with a Porous Metal Tip Array. In *Solid-State Sensors, Actuators and Microsystems Conference (TRANSDUCERS), Beijing, China, June 2001*.

- [19] R. Krpoun and H.R. Shea. Microfabricated out-of-plane arrays of integrated capillary nano-electrospray emitters. In *31st International Electric Propulsion Conference, Ann Arbor, MI, September 2009, IEPC-2009-188*. 2009.
- [20] M. Piechotka, K. Huhn, T. Henning, D. Feili, and P. Klar. Microfabrication of Colloid Emitters based on the Photo Resist SU-8 and Electro Plating. In *32nd International Electric Propulsion Conference, Wiesbaden, Germany, September 2011, IEPC-2011-276*.
- [21] I. Vasiljevich, N. Buldrini, F. Plesescu, M. Tajmar, M. Betto, and J. Gonzale del Amo. Porous Tungsten Crown Multiemitter Testing Programme Using Three Different Grain Sizes and Sintering Procedures. In *32nd International Electric Propulsion Conference, Wiesbaden, Germany, September 2011, IEPC-2011-065*.
- [22] I. Vasiljevich, N. Buldrini, F. Plesescu, and E. Schamiloglu. Performance of Porous Tungsten Needle LIMS for Use as Indium FEEP Emitters. In *32nd International Electric Propulsion Conference, Wiesbaden, Germany, September 2011, IEPC-2011-268*.
- [23] R.E Rosensweig. *Ferrohydrodynamics*. Cambridge University Press 1985.
- [24] M.D. Cowley and R.E Rosensweig. The interfacial stability of a ferromagnetic fluid. *J. Fluid Mech.*, 30(4):671–688, 1967.
- [25] C.W. Miller and E.L. Resler. Magnetic forces and the surface instability in ferromagnetic fluids. *Physics of Fluids*, 18:1112–1118, 1975.

- [26] A.G. Boudouvis, J.L. Puchalla, L.E. Scriven, and R.E. Rosensweig. Normal Field Instability and Patterns in pools of ferrofluid. *Journal of Magnetism and Magnetic Materials*, 65:307–310, 1987.
- [27] T. Mahr and I. Rehberg. Nonlinear dynamics of a single ferrofluid-peak in an oscillating magnetic field. *Physica D*, 111:335–346, 1998.
- [28] H.W. Müller. Parametrically driven surface waves on viscous ferrofluids. *Physical Review E*, 58(5):6199–6205, 1998.
- [29] B. Abou, J.-E. Wesfreid, and S. Roux. The normal field instability in ferrofluids: hexagon-square transition mechanism and wavenumber selection. *J. Fluid Mech.*, 416:217–237, 2000.
- [30] R. Friedrichs and A. Engel. Statics and dynamics of a single ferrofluid-peak. *European Physics Journal B*, 18:329–335, 2000.
- [31] A. Lange, B. Reimann, and R. Richter. Wave number of maximal growth in viscous magnetic fluids of arbitrary depth. *Physical Review E*, 61(5):5528–5539, 2000.
- [32] A. Lange. Scaling behaviour of the maximal growth rate in Rosensweig instability. *Europhysics Letters*, 55(3):327–333, 2001.
- [33] A. Lange, B. Reimann, and R. Richter. Wave number of maximal growth in viscous ferrofluids. *Magnetohydrodynamics*, 37(3):261–267, 2001.

- [34] H.E. Potts and D.A. Diver. Large-amplitude ferrofluid surface waves and jets. *New Journal of Physics*, 3:7.1–7.14, 2001.
- [35] B. Reimann, R. Richter, I. Rehberg, and A. Lange. Oscillatory decay at the Resensweig instability: Experiment and theory. *Physical Review E*, 68(3):1–8, 2003.
- [36] E.G. Megalios, N. Kapsalis, J. Paschalidis, A.G. Papathanasiou, and A.G. Boudouvis. A simple optical device for measuring free surface deformations of nontransparent liquids. *Journal of Colloid and Interface Science*, 288:508–512, 2005.
- [37] C. Gollwitzer, I. Rehberg, and R. Richter. Via hexagons to squares in ferrofluids: experiments on hysteretic surface transformations under variation of the normal magnetic field. *J. Phys. Condens. Matter*, 18:S2643–S2656, 2006.
- [38] C. Gollwitzer, G. Matthies, R. Richter, I. Rehberg, and L. Tobiska. The surface topography of a magnetic fluid: a quantitative comparison between experiment and numerical simulation. *J. Fluid Mech.*, 571:455–474, 2007.
- [39] C. Gollwitzer, A.N. Spyropoulos, A.G. Papathanasiou, A.G. Boudouvis, and R. Richter. The normal field instability under side-wall effects: comparison of experiments and computations. *New Journal of Physics*, 11, 2009.
- [40] R. Richter and A. Lange. Surface Instabilities of Ferrofluids. *Lect. Notes Phys.*, 763:157–247, 2009.

- [41] A. Gailitis. Form of surface instability of a ferromagnetic fluid. *Magnitnaya Gidrodinamika*, 5(1):68–70, 1969.
- [42] I.E. Tarapov. Surface waves and stability of free surface of a magnetizable liquid. *Journal of applied mechanics and technical physics*, 15(4):465–469, 1974.
- [43] A. Gailitis. Formation of the hexagonal pattern on the surface of a ferromagnetic fluid in an applied magnetic field. *J. Fluid Mech.*, 82(3):401–443, 1977.
- [44] R.E Rosensweig. Magnetic Fluids. *Ann. Rev. Fluid Mech.*, 19:437–463, 1987.
- [45] D. Salin. Wave Vector Selection in the Instability of an Interface in a Magnetic or Electric Field. *Europhysics Letters*, 21(6):667–670, 1993.
- [46] B. Abou, G. Néron de Surgy, and J.-E. Wesfreid. Dispersion relation in a Ferrofluid Layer of Any Thickness and Viscosity in a Normal Magnetic Field; Asymptotic Regimes. *J. Phys. II France*, 7:1159–1171, 1997.
- [47] R. Friedrichs and A. Engel. Pattern and wave number selection in magnetic fluids. *Physical review E*, 64(2):1–10, 2001.
- [48] R.E Rosensweig. Basic Equations for Magnetic Fluids with Internal Rotations. *Stefan Odenbach (Ed.): LNP 594*, pages 61–84, 2002.
- [49] M.I. Shliomis. Ferrohydrodynamics: Retrospective and issues. *Ferrofluids. Springer Berlin Heidelberg*, pages 85–111, 2002.

- [50] R. Friedrichs and A. Engel. Non-linear analysis of Rosensweig instability. *Europhysics Letters*, 63(6):826–832, 2003.
- [51] S. Bohlius, H. Brand, and H. Pleiner. Amplitude Equation of the Rosensweig Instability. *Prog. Theor. Phys. Suppl.*, 175:27–36, 2008.
- [52] S. Bohlius, H. Pleiner, and H. Brand. The Amplitude Equation for the Rosensweig Instability in Magnetic Fluids and Gels. *Progress of Theoretical Physics*, 125(1):1–46, 2011.
- [53] P Rupp. *Spatio-temporal Phenomena in a Ring of Ferrofluid Spikes*. PhD thesis, University of Bayreuth, 2003.
- [54] Jaakko Timonen, Mika Latikka, Leibler Ludwik, Robin Ras, and Olli Ikkala. Switchable Static and Dynamic Self-Assembly of Magnetic Droplets on Superhydrophobic Surfaces. *Science*, 341:253–257, 2013.
- [55] V.I. Arkhipenko, Yu. D. Barkov, and V.G. Bashtovoi. Shape of a drop of magnetized fluid in a homogeneous magnetic field. *Magnetohydrodynamics*, 14(3):373–375, 1978.
- [56] V.I. Arkhipenko, Yu. D. Barkov, and V.G. Bashtovoi. Behavior of a drop of a magnetizable liquid in magnetic fluids. *Magnetohydrodynamics*, 16(3):221–228, 1980.

- [57] J.C. Bacri and D. Salin. Instability of ferrofluid magnetic drops under magnetic field. *J. Physique - Letters*, 43:L-649 – L-654, 1982.
- [58] V.G. Bashtovoy, B.M. Berkovsky, and A.N. Vislovich. *Introduction to thermomechanics of magnetic fluids*. Hemisphere Publishing Corp., Washington, D.C., 1988.
- [59] S. Chikazumi. *Physics of Magnetism*. John Wiley & Sons, Inc., New York, NY, 1964.
- [60] A. Aharoni. *Introduction to the Theory of Ferromagnetism*. Oxford University Press, New York, 1996.
- [61] J.W. Swan. Stress and other Effects Produced in Resin and in a Viscid Compound of Resin and Oil by Electrification. *Royal Society Publishing*, 62:38–46, 1897-1898.
- [62] J.R. Melcher. Electrohydrodynamic and Magnetohydrodynamic Surface Waves and Instabilities. *The Physics of Fluids*, 4(11):1348–1354, 1961.
- [63] E.B. Devitt and J.R. Melcher. Surface electrohydrodynamics with high-frequency fields. *Phys. Fluids*, 8:1193–1195, 1965.
- [64] J.R. Melcher and C.V. Smith Jr. Electrohydrodynamic Charge Relaxation and Interfacial Perpendicular-Field Instability. *The Physics of Fluids*, 12(4):778–790, 1969.

- [65] N.M. Miskosky, M. Chung, P.H. Cutler, T.E Feuchtwange, and E. Kazes. An electrohydrodynamic formalism for ion and droplet formation in stressed conducting fluids. *J. Vac. Sci. Technol. A*, 6(5):2992–2997, 1988.
- [66] N.M. Miskosky, J. He, P.H. Cutler, and E. Chung. A Hydrodynamical Study of the Instability of a Planar Liquid Metal Ion Source (Summary). *Colloque De Physique C8*, 50(11):175–177, 1989.
- [67] A.L. Pregonzer and J.R. Woodworth. Measurements of temporal and spatial characteristics of electrohydrodynamic instabilities. *J. Appl. Phys.*, 65(5):1823–1828, 1989.
- [68] A. Pregonzer. Electrohydrodynamically driven, large-area liquid metal ion source for inertial confinement fusion. *Rev. Sci. Instrum*, 61(1):571–573, 1990.
- [69] N.M. Miskosky, J. He, P.H. Cutler, and M. Chung. Electrohydrodynamical study of the instability of a thin liquid metal film: Application to planar liquid metal ion sources. *J. Appl. Phys.*, 69(4):1656–1961, 1990.
- [70] G. Néron de Surgy, J.-P. Chabrierie, O. Denoux, and J.-E. Wesfreid. Linear growth of instabilities on a liquid metal under normal electric field. *J. Phys. II France*, 3:1201–1225, 1993.
- [71] H. González, G. Néron de Surgy, and J.P. Chabrierie. Influence of bounded geometry on electrocapillary instability. *Physical Review B*, 50(40):2520–2528, 1994.

- [72] C.S. Mayberry, E. Schamiloglu, and G.W. Donohoe. Measurements of the electrohydrodynamic instability in planar geometry using gallium. *J. Appl. Phys.*, 78(9):5270–5276, 1995.
- [73] J. Mitterauer. Microstructured liquid metal ion and electron sources (MILMIS/MILMES). *Applied Surface Science*, 87/88:79–90, 1995.
- [74] G. Néron de Surgy, J.-P. Chabrerie, and J.-E. Wesfreid. Emission of Liquid Metal in Vacuum. *IEEE Transactions on Dielectrics and Electrical Insulation*, 2(2):184–189, 1995.
- [75] H. González, G. Néron de Surgy, and J.P. Chabrerie. Electrocapillary instability in annular geometry. *Phys. Fluids*, 9(9):2542–2549, 1997.
- [76] J. He, N.M. Miskosky, P.H. Cutler, and M. Chung. Effects of viscosity on capillary wave instabilities of a planar liquid-metal surface in an electric field. *J. Appl. Phys.*, 68(4):1475–1482, 1990.
- [77] A. Pregoner. Electrohydrodynamically driven large-area liquid-metal ion sources. *J. Appl. Phys.*, 58(12):4509–4511, 1985.
- [78] G. Néron de Surgy, H. González, and J.-P. Chabrerie. Influence of bounded geometry on the initial growth of electrocapillary instability for a liquid metal under electric field. *Applied Surface Science*, 87/88:91–98, 1995.

- [79] A.R.F Elhefnawy. Nonlinear electrohydrodynamic instability of two liquid layers. *International Journal of Engineering Science*, 40:319–332, 2002.
- [80] D.F. Belonozhko and A.I. Grigor'ev. Nonlinear Electrocapillary Waves on a Charged Surface of the Ideal Liquid. *Technical Physics Letters*, 29(9):768–770, 2003.
- [81] A.L. Pregenzer and B.M. Marder. Liquid lithium ion source: Nonlinear behavior of liquid surface in electric field. *J. Appl. Phys.*, 60(11):3821–3824, 1986.
- [82] J. Mitterauer. The surface dependence of different emission modes on mercury arc film cathodes. *J. Phys. D: Appl. Phys.*, 6:L91–L93, 1973.
- [83] J. Mitterauer. Field Emission Electric Propulsion: Emission Site Distribution of Slit Emitters. *IEEE Transactions on Plasma Science*, PS-15(5):593–598, 1987.
- [84] J. Mitterauer. Field Emission from thin liquid metal films. *Applied Surface Science*, 94/95:161–170, 1996.
- [85] L.W. Swanson. Electron and Ion Emission From Liquid Metal Surfaces. *IEEE Transactions on Plasma Science*, 19(5):746–748, 1991.
- [86] I.I. Beilis, M. Keidar, R.L. Boxman, and S. Goldsmith. Theoretical study of plasma expansion in a magnetic field in a disk anode vacuum arc. *J. Appl. Phys.*, 83(2):709–717, 1998.

- [87] N. Jain, Y. Wang, S.K. Jones, B.S. Hawkett, and G.G. Warr. Optimized Steric Stabilization of Aqueous Ferrofluids and Magnetic Nanoparticles. *Langmuir*, 26(6):4465–4472, 2010.
- [88] N. Jain, X. Zhang, B.S. Hawkett, and G.G. Warr. Stable and Water-Tolerant Ionic Liquid Ferrofluid. *Applied Materials and Interfaces*, (3):662–667, 2011.
- [89] J.A. Widegren, E.M. Saurer, K.N. Marsh, and J.W. Magee. Electrolytic conductivity of four imidazolium-based room-temperature ionic liquids and the effects of water impurity. *Journal of Chemical Thermodynamics*, 37(6):569–575, 2005.
- [90] C. Schreiner, S. Zugmann, R. Hartl, and H. Gores. Fractional Walden Rule for Ionic Liquids: Examples from Recent Measurements and a Critique of the So-Called Ideal KCI Line for the Walden Plot. *J. Chem. Eng. Data*, 55(5):1784–1788, 2010.
- [91] Paulo Lozano and Manuel Martínez-Sánchez. Ionic liquid ion sources: characterization of externally wetted emitters. *Journal of Colloid and Interface Science*, pages 415–421, 2004.
- [92] P. Lozano and Manuel Martínez-Sánchez. Ionic liquid ion sources: suppression of electrochemical reactions using voltage alternation. *Journal of Colloid and Interface Science*, 280:149–154, 2004.
- [93] D.G. Courtney, H.Q. Li, and P. Lozano. Emission measurements from planar arrays of porous ionic liquid ion sources. *Journal of Physics D: Applied Physics*, 45, 2012.

- [94] P. Lozano and Manuel Martínez-Sánchez. On the dynamic response of externally wetted ionic liquid ion sources. *J. Phys. D: Appl. Phys*, 38:2371–2377, 2005.
- [95] W. Driesel, Ch. Dietzsch, and R. Mühle. Tip-shape investigation of Au-Si alloy liquid metal ion source using a high voltage transmission electron microscope. *Journal of Physics D: Applied Physics*, 28(4):787–793, 1994.
- [96] M.D. Paine. Transient electrospray behaviour following high voltage switching. *Microfluid Nanofluid*, 6:775–783, 2009.
- [97] D.P.H Smith. The Electrohydrodynamic Atomization of Liquids. *IEEE Transactions on Industry Applications*, 1A-22(3):527–535, 1986.
- [98] J.D. Regele, M.J. Papac, M.J.A. Rickard, and D. Dunn-Rankin. Effects of capillary spacing on EHD spraying from an array of cone jets. *Journal of Aerosol Science*, 33(11):1471–1479, 2002.
- [99] B.Q.T. Si, D. Byun, and S. Lee. Experimental and theoretical study of a cone-jet for an electrospray microthruster considering the interference effect in an array of nozzles. *Journal of Aerosol Science*, 38(9):924–934, 2007.
- [100] D. Rannacher and A. Engel. Suppressing the Rayleigh-Taylor instability with a rotating magnetic field. *Physical Review E*, 75(1):016311, 2007.

Appendix A

Magnetic Field Mapping

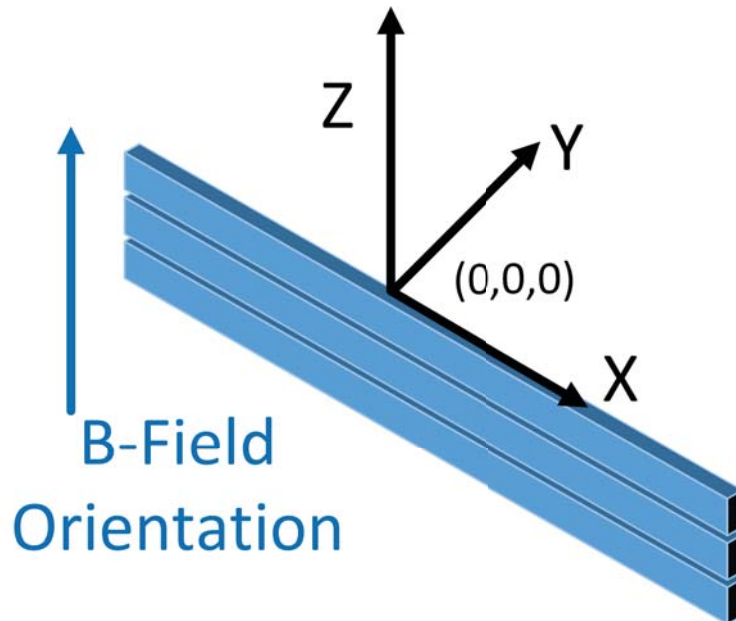


Figure A.1: Illustration of stack of magnets, orientation of magnetization, and coordinates. (Same as Figure 5.1, shown here for convenience.)

Table A.1
Magnetic field (Gauss) in the B_z at coordinate $x = 0.0$ mm

z mm	y						
	0.0 mm	0.5 mm	1.0 mm	1.5 mm	2.0 mm	2.5 mm	3.0 mm
1.6	3004	2884	2565	2072	1560	1144	822
2.1	2443	2358	2152	1834	1484	1163	898
2.6	2042	1980	1840	1627	1381	1136	923
3.1	1729	1692	1595	1447	1268	1084	912
3.6	1497	1466	1400	1294	1159	1020	881
4.1	1310	1288	1239	1162	1060	952	841
4.6	1159	1143	1108	1049	973	887	796
5.1	1036	1023	997	953	893	825	752
5.6	933	926	905	870	823	768	707
6.1	846	842	825	798	760	715	667
6.6	774	770	757	735	704	667	626
7.1	711	780	698	680	654	623	589
7.6	657	653	645	630	610	584	555
8.1	609	606	600	587	570	548	524
8.6	566	564	559	548	534	515	494
9.1	529	257	522	513	501	486	468
9.6	495	494	490	483	472	459	443
10.1	465	464	461	454	445	434	420
10.6	438	437	434	429	421	411	399
11.1	413	412	410	404	399	390	380
11.6	391	390	388	384	378	370	361
12.1	370	370	368	364	359	352	344
12.6	352	351	350	346	342	336	328
13.1	334	334	333	330	326	320	314
13.6	319	318	317	315	311	306	300
14.1	304	304	303	300	297	293	287
14.6	290	290	289	287	284	281	276
15.1	278	278	277	275	272	269	264
15.6	266	266	265	264	261	258	254
16.1	255	255	254	253	251	248	244
16.6	245	245	244	243	241	238	235
17.1	235	235	235	234	232	229	226
17.6	226	226	226	225	223	221	218
18.1	218	218	217	217	215	213	210
18.6	210	210	209	209	207	205	203
19.1	202	202	202	201	200	198	196
19.6	195	195	195	194	193	191	190
20.1	189	189	188	188	187	185	183

Table A.2
Magnetic field (Gauss) in the B_z at coordinate $x = 25.4 \text{ mm}$

z mm	y						
	0.0 mm	0.5 mm	1.0 mm	1.5 mm	2.0 mm	2.5 mm	3.0 mm
1.6	2926	2963	2732	2284	1772	1291	914
2.1	2430	2427	2260	1973	1626	1278	986
2.6	2028	2018	1909	1719	1475	1221	991
3.1	1724	1716	1643	1506	1333	1143	964
3.6	1488	1483	1431	1334	1207	1063	920
4.1	1303	1302	1260	1188	1095	984	872
4.6	1156	1154	1123	1069	996	909	820
5.1	1037	1035	1008	967	911	842	770
5.6	934	933	914	881	835	781	721
6.1	848	846	832	805	770	726	676
6.6	776	775	762	742	712	675	634
7.1	713	712	702	685	660	630	596
7.6	659	658	562	552	537	519	497
8.1	610	610	603	591	574	552	527
8.6	568	568	562	552	537	519	497
9.1	531	530	525	516	504	488	470
9.6	497	497	492	485	474	460	447
10.1	467	466	463	456	447	435	421
10.6	440	439	436	430	422	412	400
11.1	415	415	412	407	400	391	380
11.6	393	392	390	385	379	371	362
12.1	372	372	369	366	360	353	344
12.6	354	353	351	347	343	336	329
13.1	336	336	334	331	326	321	314
13.6	320	320	318	315	312	306	301
14.1	305	305	303	301	298	293	288
14.6	292	292	290	288	285	281	276
15.1	279	279	278	275	273	269	265
15.6	267	267	266	264	261	258	254
16.1	256	256	255	253	251	248	244
16.6	246	246	245	243	241	238	235
17.1	236	236	235	234	232	229	226
17.6	227	227	226	225	223	220	218
18.1	219	218	218	217	215	212	210
18.6	211	210	210	208	207	205	203
19.1	203	203	202	201	200	198	196
19.6	196	196	195	194	193	191	189
20.1	189	189	188	187	186	185	183

Table A.3
Magnetic field (Gauss) in the B_z at coordinate $x = 50.8 \text{ mm}$

z mm	y						
	0.0 mm	0.5 mm	1.0 mm	1.5 mm	2.0 mm	2.5 mm	3.0 mm
1.6	2727	2674	2486	2121	1698	1304	987
2.1	2249	2212	2078	1833	1547	1260	1012
2.6	1889	1868	1779	1609	1409	1195	1000
3.1	1622	1606	1543	1425	1282	1116	965
3.6	1412	1400	1354	1270	1162	1039	917
4.1	1244	1234	1202	1138	1057	962	865
4.6	1108	1104	1077	1030	967	891	814
5.1	996	991	973	936	887	826	736
5.6	901	898	882	855	815	766	715
6.1	822	819	807	784	752	712	671
6.6	753	751	741	723	697	664	630
7.1	693	692	684	669	648	621	591
7.6	642	640	634	621	604	581	555
8.1	595	594	589	579	563	544	523
8.6	555	553	550	540	528	512	493
9.1	518	517	514	506	495	482	466
9.6	486	485	483	476	466	454	441
10.1	456	455	453	448	440	430	418
10.6	430	430	417	422	416	406	396
11.1	406	405	403	399	393	385	375
11.6	384	383	382	378	373	366	357
12.1	363	363	362	358	354	347	340
12.6	344	344	343	340	336	330	324
13.1	327	326	326	324	320	315	309
13.6	312	311	310	308	305	301	295
14.1	296	296	296	294	291	287	282
14.6	283	283	282	281	278	274	270
15.1	270	270	269	268	265	262	258
15.6	258	258	258	256	254	251	248
16.1	247	247	246	245	243	241	238
16.6	237	236	236	235	234	231	228
17.1	227	227	227	226	224	222	219
17.6	218	217	217	216	215	213	211
18.1	209	209	209	208	207	205	203
18.6	201	201	201	200	199	197	195
19.1	193	193	193	193	191	190	188
19.6	186	186	186	185	184	183	181
20.1	179	179	179	179	178	176	175

Table A.4
Magnetic field (Gauss) in the B_y at coordinate $x = 0.0$ mm

z mm	y						
	0.0 mm	0.5 mm	1.0 mm	1.5 mm	2.0 mm	2.5 mm	3.0 mm
3.1	117	367	588	776	927	1024	1075
3.6	120	349	545	711	850	942	991
4.1	119	303	460	599	711	799	852
4.6	116	266	396	511	608	685	737
5.1	111	238	346	441	424	593	642
5.6	107	215	305	385	459	518	565
6.1	102	195	272	341	405	458	501
6.6	97	179	245	304	360	408	447
7.1	93	164	225	274	322	365	401
7.6	89	152	203	249	291	330	362
8.1	85	141	186	226	264	300	329
8.6	81	132	171	207	242	273	300
9.1	78	123	159	191	221	250	275
9.6	75	116	148	177	204	230	253
10.1	72	109	138	164	189	213	234
10.6	69	103	130	153	176	197	217
11.1	66	98	122	143	164	184	202
11.6	64	93	115	134	153	171	188
12.1	61	89	109	126	144	161	176
12.6	59	85	103	119	135	151	165
13.1	57	81	98	113	128	142	155
13.6	55	78	93	107	121	134	146
14.1	54	75	89	101	114	127	138
14.6	52	72	85	96	108	120	131
15.1	50	69	81	92	103	114	124
15.6	49	66	78	88	98	108	117
16.1	47	64	75	84	94	103	112
16.6	46	62	72	81	90	98	107
17.1	45	60	69	78	86	94	102
17.6	44	58	67	74	82	90	97
18.1	42	56	64	72	79	86	93
18.6	41	55	62	69	76	83	89
19.1	40	53	60	66	73	79	86
19.6	39	51	58	64	70	77	82
20.1	38	50	56	62	68	74	79
20.6	37	48	55	60	65	71	76
21.1	37	47	53	58	63	68	73

Table A.5
Magnetic field (Gauss) in the B_y at coordinate $x = 25.4 \text{ mm}$

z mm	y						
	0.0 mm	0.5 mm	1.0 mm	1.5 mm	2.0 mm	2.5 mm	3.0 mm
3.1	0	336	670	892	1030	1107	1131
3.6	66	351	591	783	914	994	1022
4.1	68	289	482	637	751	832	875
4.6	63	243	496	528	628	703	750
5.1	60	207	332	445	532	602	648
5.6	58	178	284	379	456	519	564
6.1	55	156	245	328	396	451	494
6.6	52	138	214	285	345	395	436
7.1	49	123	189	251	304	349	387
7.6	46	109	168	222	270	311	345
8.1	44	99	150	199	241	278	310
8.6	41	89	135	179	216	250	279
9.1	39	81	112	161	195	225	253
9.6	37	75	110	146	177	205	229
10.1	35	68	101	133	161	187	209
10.6	33	64	92	122	147	171	192
11.1	31	59	85	111	135	156	176
11.6	30	55	78	103	124	143	162
12.1	28	51	72	95	114	132	149
12.6	27	47	67	88	105	112	138
13.1	25	44	63	81	98	113	128
13.6	24	41	58	76	91	105	119
14.1	23	39	55	71	85	98	111
14.6	22	37	51	66	79	91	103
15.1	21	35	48	62	74	85	96
15.6	20	33	45	58	69	80	90
16.1	19	31	42	55	65	75	85
16.6	18	30	40	51	61	70	80
17.1	18	28	38	48	57	66	75
17.6	17	26	36	46	54	62	71
18.1	16	25	34	43	51	59	67
18.6	16	24	32	41	49	56	63
19.1	15	23	31	39	46	52	59
19.6	14	22	29	37	43	50	56
20.1	14	21	28	35	41	47	53
20.6	14	20	26	33	39	45	51
21.1	13	19	25	31	37	42	48
21.6	13	18	24	30	35	40	46

Table A.6
Magnetic field (Gauss) in the B_y at coordinate $x = 50.8 \text{ mm}$

z mm	y						
	0.0 mm	0.5 mm	1.0 mm	1.5 mm	2.0 mm	2.5 mm	3.0 mm
3.1	40	237	443	625	797	908	974
3.6	26	200	372	547	687	797	859
4.1	22	161	301	441	563	658	722
4.6	22	134	245	362	465	550	611
5.1	21	113	206	302	389	464	522
5.6	20	96	174	257	330	397	450
6.1	19	83	149	219	283	342	391
6.6	18	74	129	190	246	298	342
7.1	18	65	113	167	215	261	301
7.6	17	58	100	145	189	230	266
8.1	16	52	89	129	168	204	237
8.6	15	47	79	115	149	182	212
9.1	14	43	72	103	134	164	191
9.6	14	39	65	93	121	148	173
10.1	14	36	59	84	109	134	157
10.6	13	33	53	77	99	121	142
11.1	13	31	49	70	91	111	130
11.6	12	29	45	64	83	102	119
12.1	12	27	42	59	76	94	110
12.6	11	25	39	55	70	86	101
13.1	11	23	36	51	65	80	93
13.6	10	22	66	47	60	74	86
14.1	10	21	31	44	56	68	80
14.6	10	19	29	41	52	64	75
15.1	9	18	28	38	49	59	70
15.6	9	18	26	36	46	55	65
16.1	9	16	25	34	43	52	61
16.6	9	16	23	32	40	49	57
17.1	8	15	22	30	38	46	54
17.6	8	15	21	28	36	43	50
18.1	8	14	20	27	34	41	48
18.6	8	13	19	25	32	38	45
19.1	7	12	18	24	30	36	42
19.6	7	12	17	23	29	34	40
20.1	7	12	16	22	27	33	38
20.6	7	11	16	21	26	31	36
21.1	7	11	15	20	25	30	34
21.6	7	10	15	19	24	28	33

Appendix B

Helmholtz Coil Magnetic Field

Measurements

Table B.1

Axial magnetic field on center-line of the Helmholtz coil described in Section 3.5 at various driven currents.

Current (A)	Voltage (V)	Magnetic Field (Gauss)
0.0	0.0	0.1
0.5	3.0	21.0
1.0	5.3	42.9
1.5	7.0	63.7
2.0	9.0	84.7
2.5	11.0	106.2
3.0	13.0	126.9
3.5	15.0	148.0
4.0	17.0	169.1
4.5	19.1	191.2
5.0	20.4	212.0
5.5	22.5	233.0
6.0	24.0	24.7
6.5	26.7	257.6
7.0	28.9	297.1
7.5	31.0	318.6
8.0	33.3	339.9
8.5	35.6	360.6
9.0	38.0	382.1
9.5	40.4	402.5
10.0	43.0	424.9

Appendix C

Progression of ILFF in uniform magnetic field, increasing Electric field

This appendix contains images of the ILFF Ethylammonium Nitrate (EAN) with Sirtex magnetic nanoparticles in the Helmholtz coil described in Section 3.5, and an extraction electrode placed well above the ILFF pool. The author was not able to find a record of the spacing between the extraction electrode and the ILFF pool, but it was on the order of a centimeter or greater. The initial image is with no magnetic or electric fields applied. The following images had 7 A applied to the Helmholtz coil (providing a uniform magnetic field of 297.1 Gauss). Each subsequent image was taken with a strong voltage applied between the ILFF pool and counter electrode. The goal of this was not to obtain ion emission, but to demonstrate a Rosensweig instability in an ILFF could be distorted by an electric field.

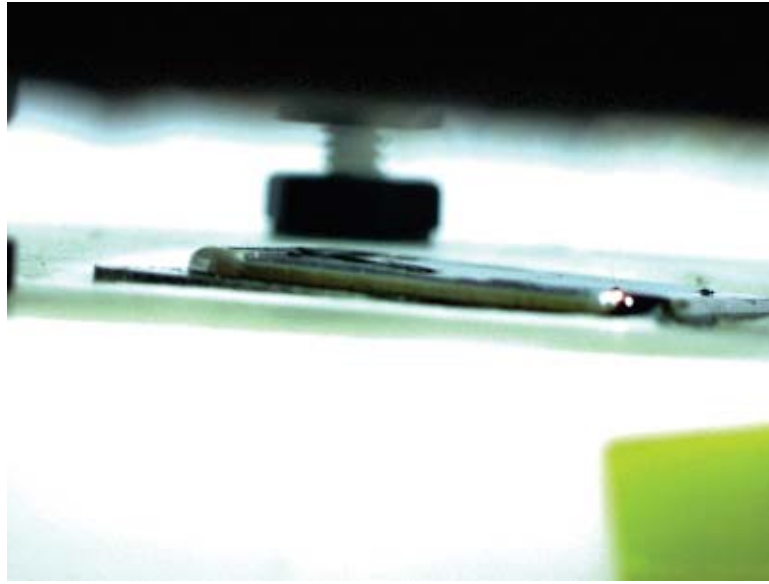


Figure C.1: ILFF (EAN with Sirtex magnetic nanoparticles) with a magnetic field of 0 Gauss and applied voltage of 0 V.)

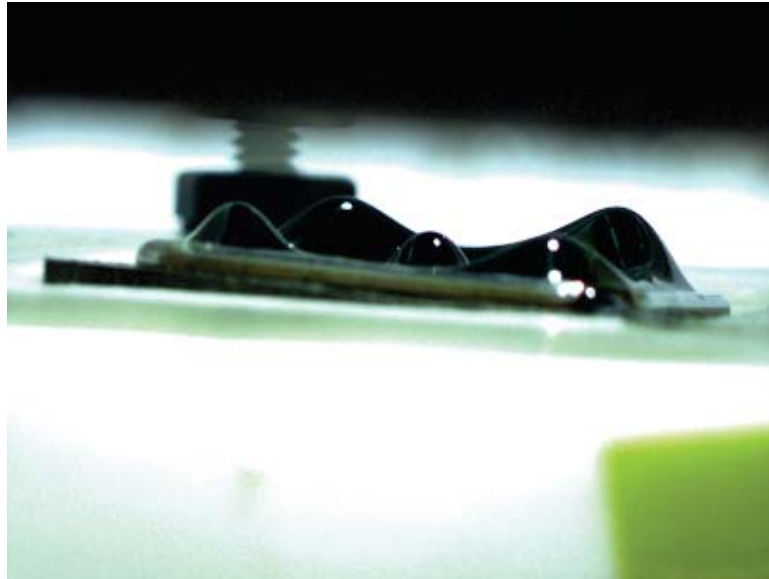


Figure C.2: ILFF (EAN with Sirtex magnetic nanoparticles) with a magnetic field of 297.1 Gauss and applied voltage of 0 V.)

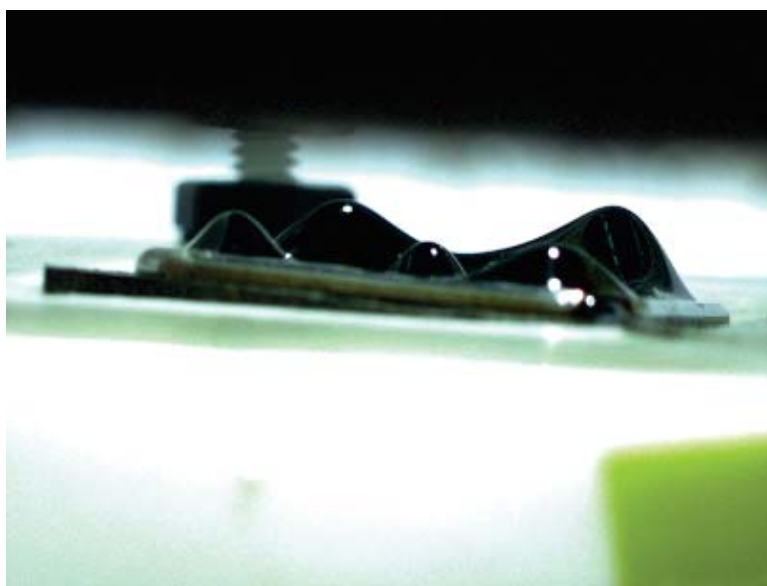


Figure C.3: ILFF (EAN with Sirtex magnetic nanoparticles) with a magnetic field of 297.1 Gauss and applied voltage of -1000 V.)

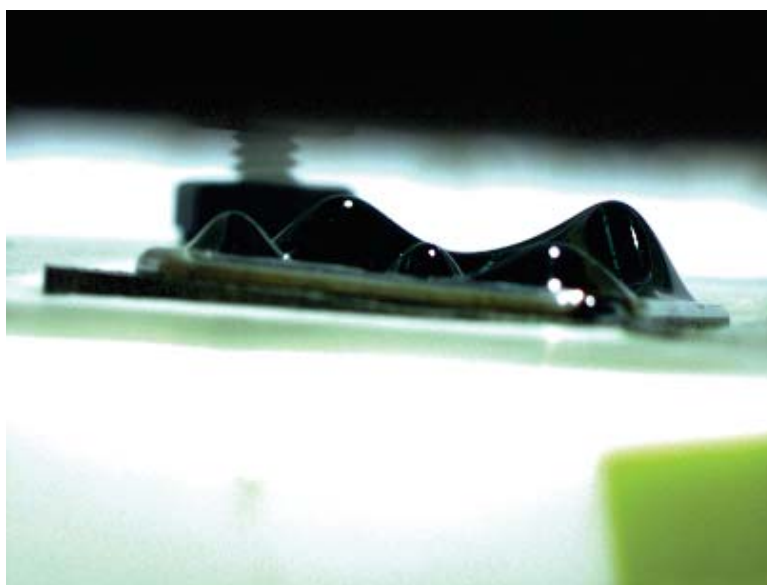


Figure C.4: ILFF (EAN with Sirtex magnetic nanoparticles) with a magnetic field of 297.1 Gauss and applied voltage of -2000 V.)

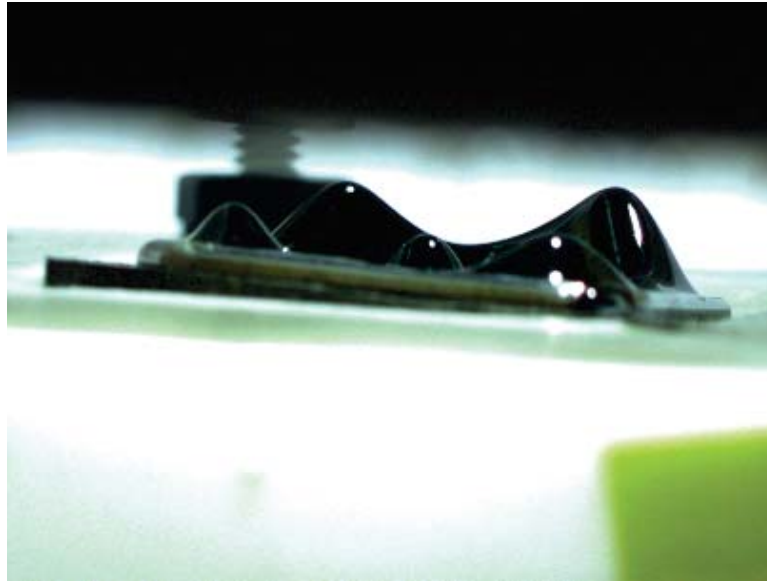


Figure C.5: ILFF (EAN with Sirtex magnetic nanoparticles) with a magnetic field of 297.1 Gauss and applied voltage of -3000 V.)

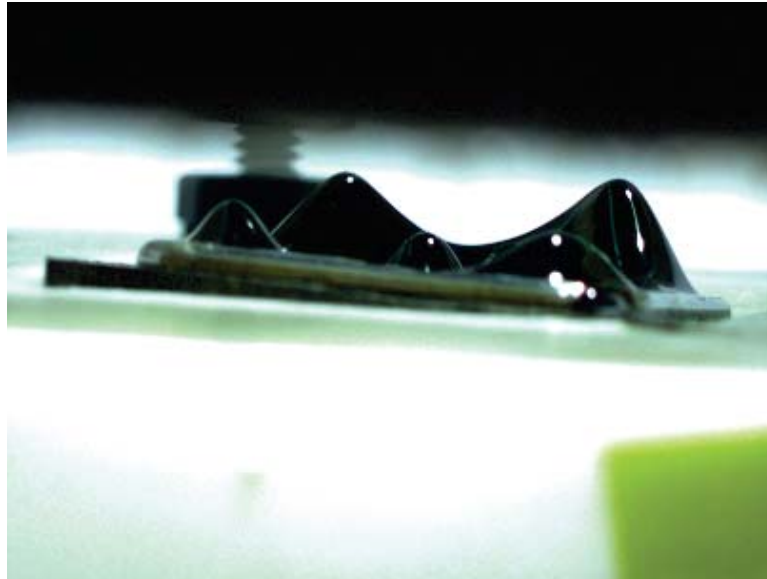


Figure C.6: ILFF (EAN with Sirtex magnetic nanoparticles) with a magnetic field of 297.1 Gauss and applied voltage of -4000 V.)



Figure C.7: ILFF (EAN with Sirtex magnetic nanoparticles) with a magnetic field of 297.1 Gauss and applied voltage of -4500 V.)

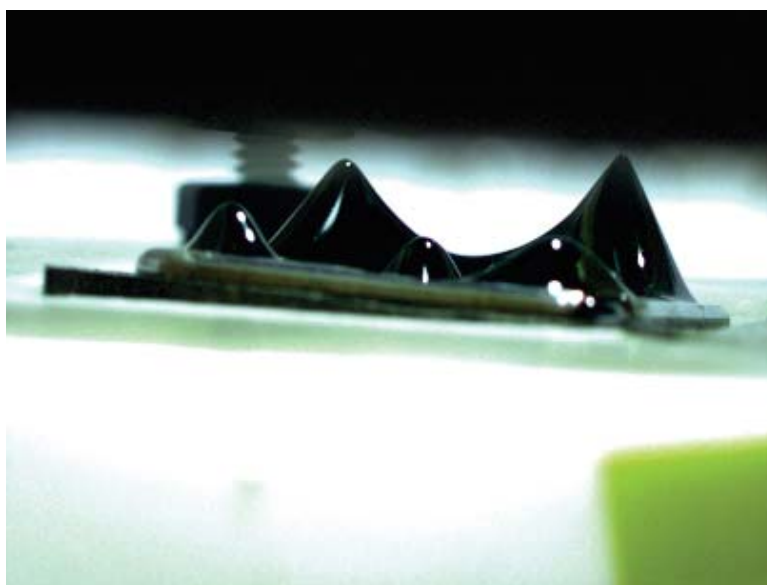


Figure C.8: ILFF (EAN with Sirtex magnetic nanoparticles) with a magnetic field of 297.1 Gauss and applied voltage of -5000 V.)

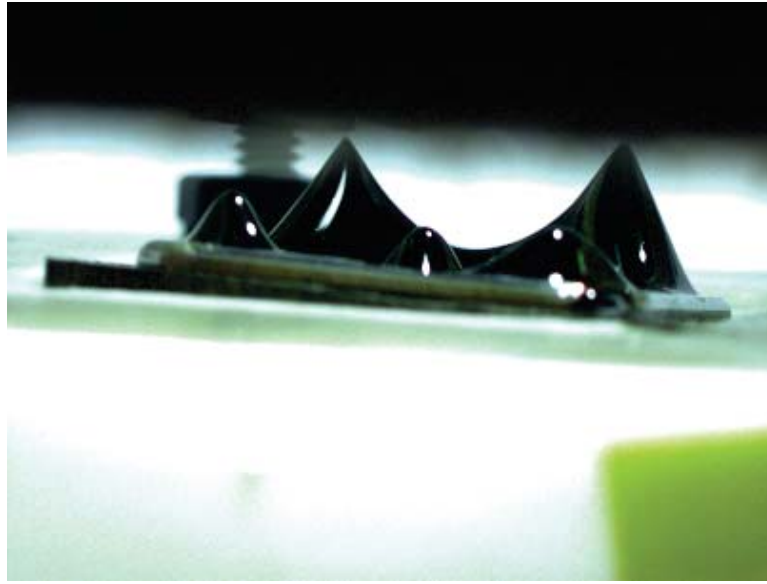


Figure C.9: ILFF (EAN with Sirtex magnetic nanoparticles) with a magnetic field of 297.1 Gauss and applied voltage of -5500 V.)

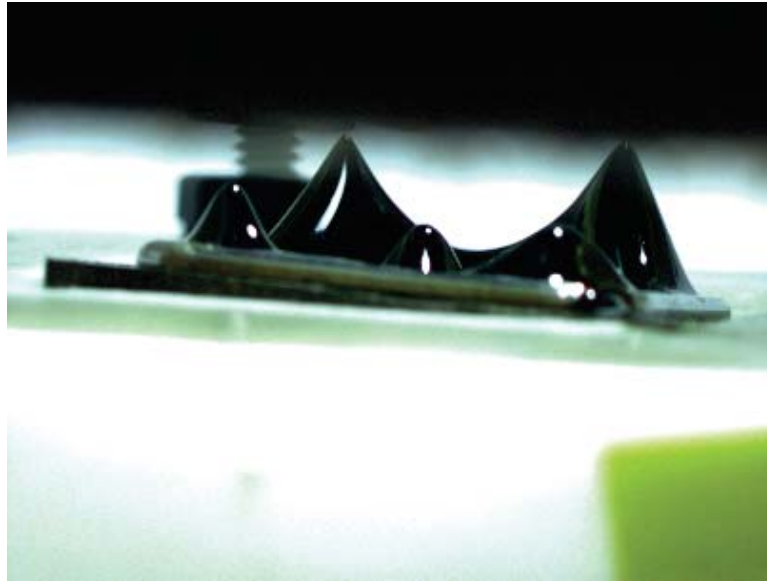


Figure C.10: ILFF (EAN with Sirtex magnetic nanoparticles) with a magnetic field of 297.1 Gauss and applied voltage of -600 V.)

Appendix D

ILFF peak damage and repair sequence

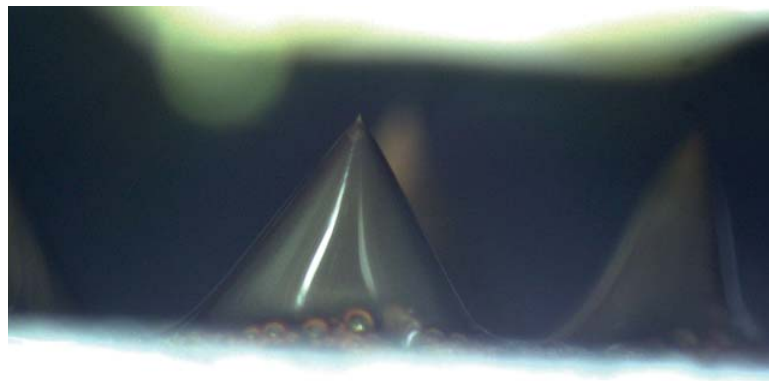


Figure D.1: EAN based ILFF emitting ions at -3700 V of extraction voltage. Image was taken roughly 3 minutes before large bubble formed.



Figure D.2: Large bubble forming in EAN based ILFF. Emission from this peak ceased. Voltage decreased to -3200 V by the user because they didn't want to break anything.

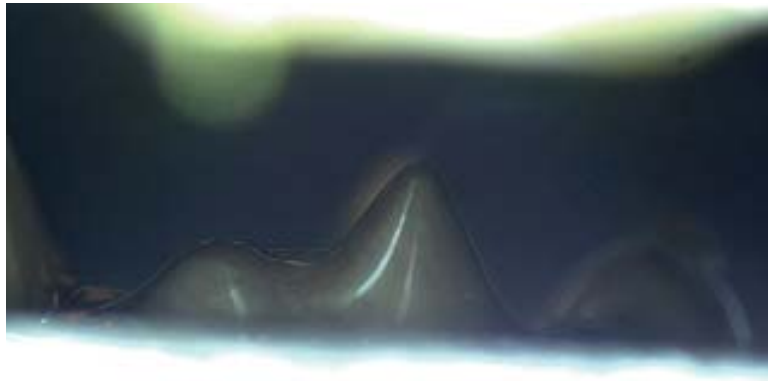


Figure D.3: Image after the bubble popped in the ILFF popped. Two smaller peaks formed from the previously one larger peak. Voltage was -3200 V. This image was less than a minute after the bubble popped.



Figure D.4: ILFF peaks continue to grow and separate. Voltage was increased to -3450 V. Image taken roughly one minute after bubble burst.



Figure D.5: The two new ILFF peaks separate even further and grow in height. Voltage was increased to -3500 V. Image taken roughly 2 minutes after bubble burst.



Figure D.6: The right peak continues to grow in height, and the tip of the peak appears to be getting much sharper. There also seems to be a bit of asymmetry to the peak. The applied voltage was maintained at -3500 V. This image was taken roughly 2 minutes after the bubble burst.



Figure D.7: The tip of the ILFF split into 3 emission sites spaced out symmetrically around the tip. The voltage remained constant at -3500 V and this was roughly 3 minutes after the bubble burst.



Figure D.8: A zoomed-in image of Figure D.7, with an additional insert focusing on the three emission sites at the tip.

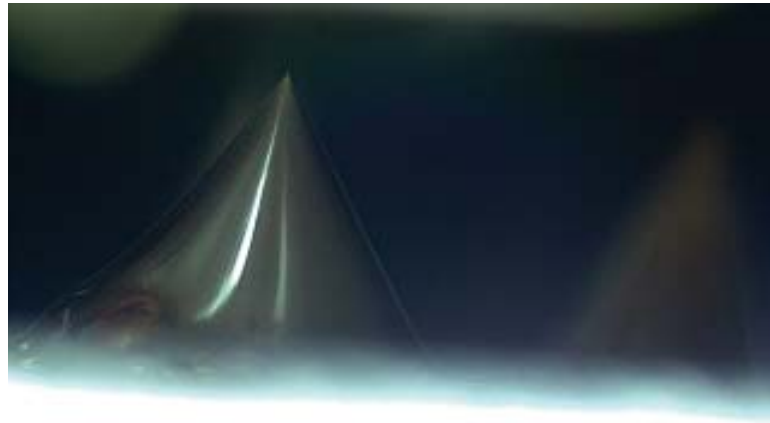


Figure D.9: Roughly fifteen minutes after the bubble burst in the ILFF, the peak under observation transitions from the multiple emission site mode to a single emission site mode. The applied voltage was increased to -3600 V.

Appendix E

Analysis using QuickField

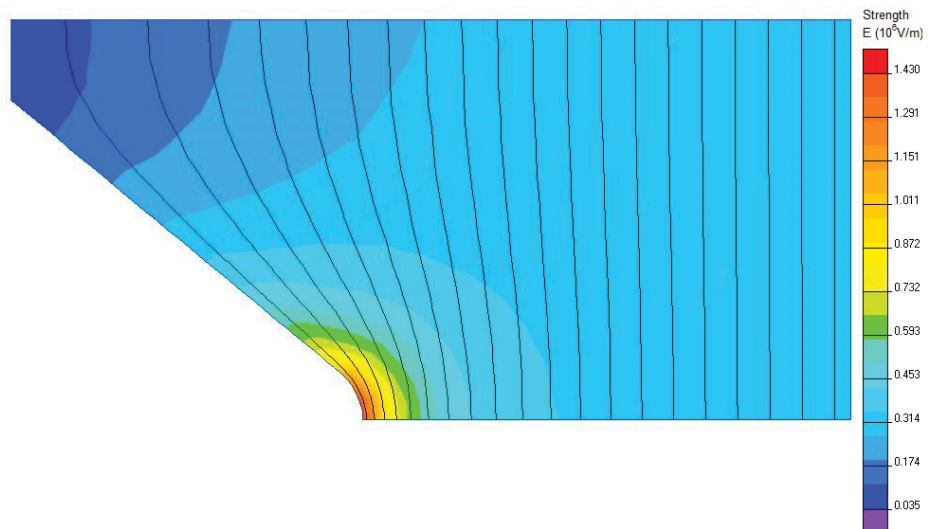


Figure E.1: Electric field results from QuickField with an applied voltage of 1000 V applied between ILFF (lower left geometry) and extraction electrode (right boundary). Geometry from Run 5 at 0 V.

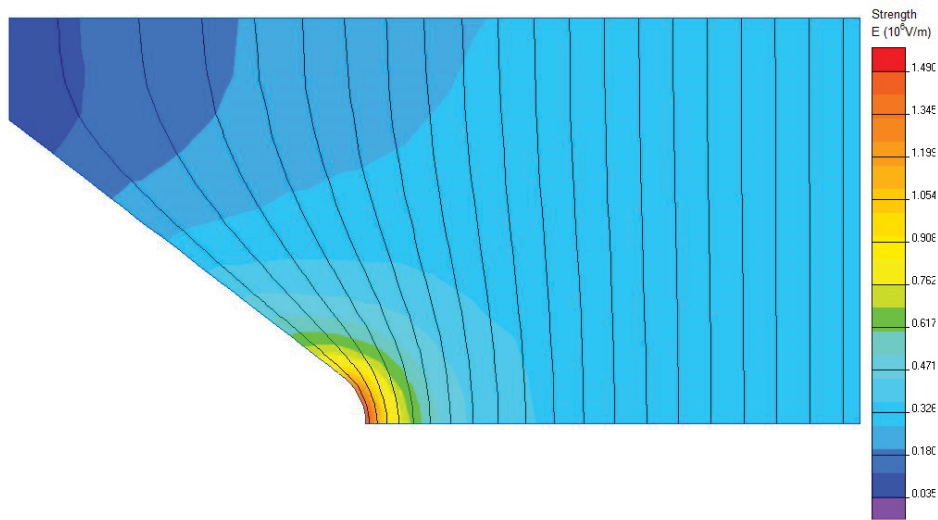


Figure E.2: Electric field results from QuickField with an applied voltage of 1000 V applied between ILFF (lower left geometry) and extraction electrode (right boundary). Geometry from Run 5 at 500 V.

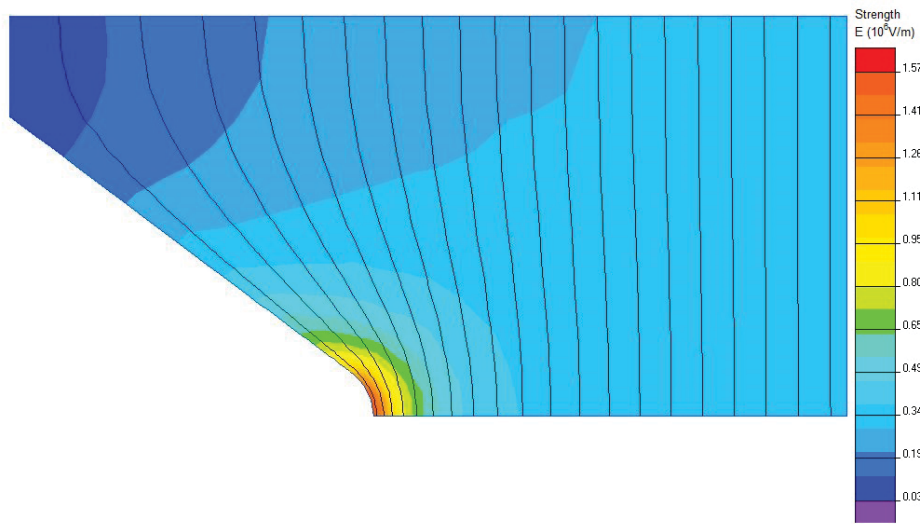


Figure E.3: Electric field results from QuickField with an applied voltage of 1000 V applied between ILFF (lower left geometry) and extraction electrode (right boundary). Geometry from Run 5 at 1000 V.

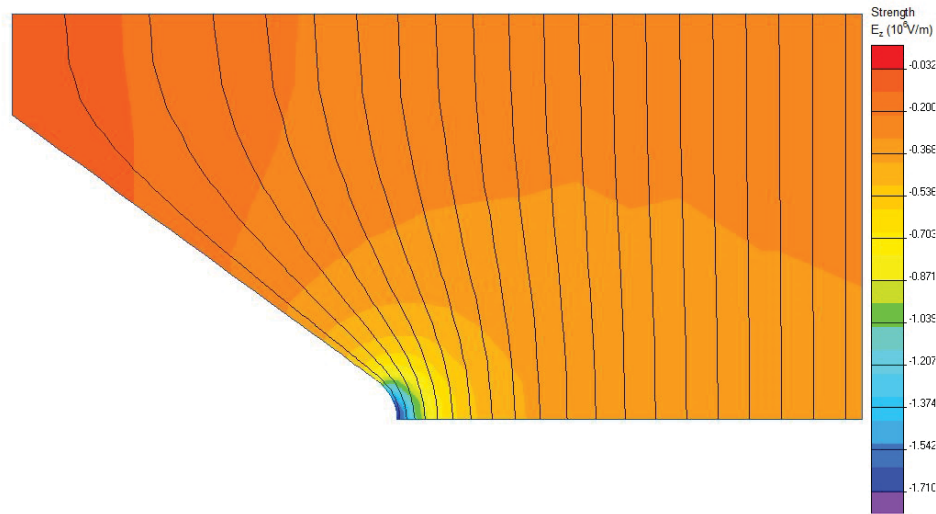


Figure E.4: Electric field results from QuickField with an applied voltage of 1000 V applied between ILFF (lower left geometry) and extraction electrode (right boundary). Geometry from Run 5 at 1200 V.

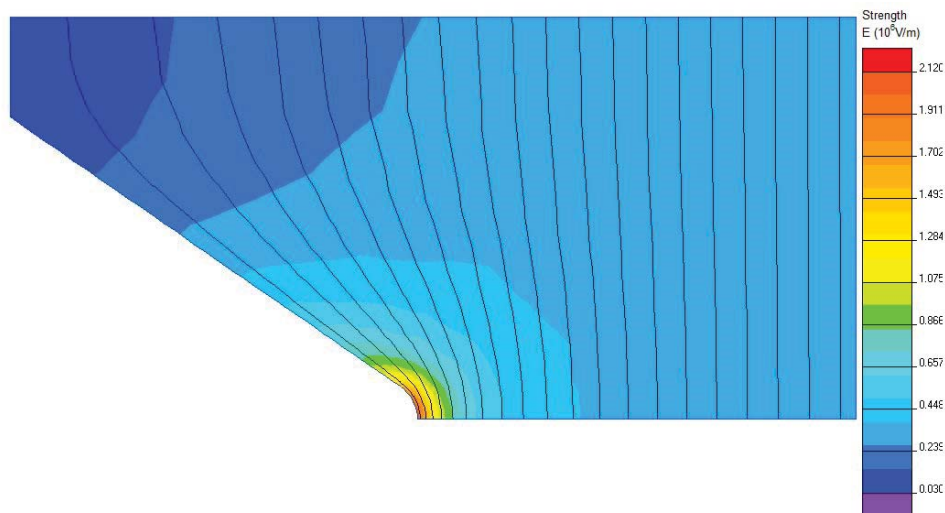


Figure E.5: Electric field results from QuickField with an applied voltage of 1000 V applied between ILFF (lower left geometry) and extraction electrode (right boundary). Geometry from Run 5 at 2000 V.

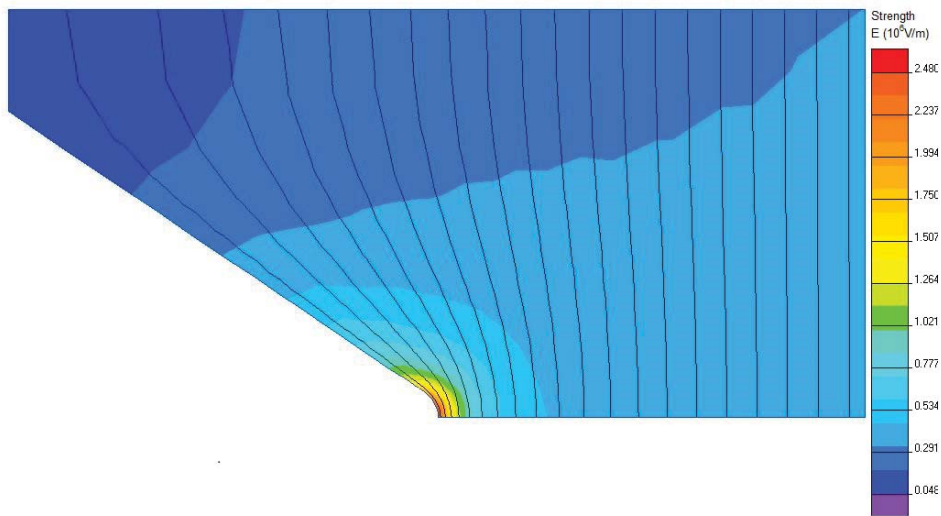


Figure E.6: Electric field results from QuickField with an applied voltage of 1000 V applied between ILFF (lower left geometry) and extraction electrode (right boundary). Geometry from Run 5 at 2200 V.

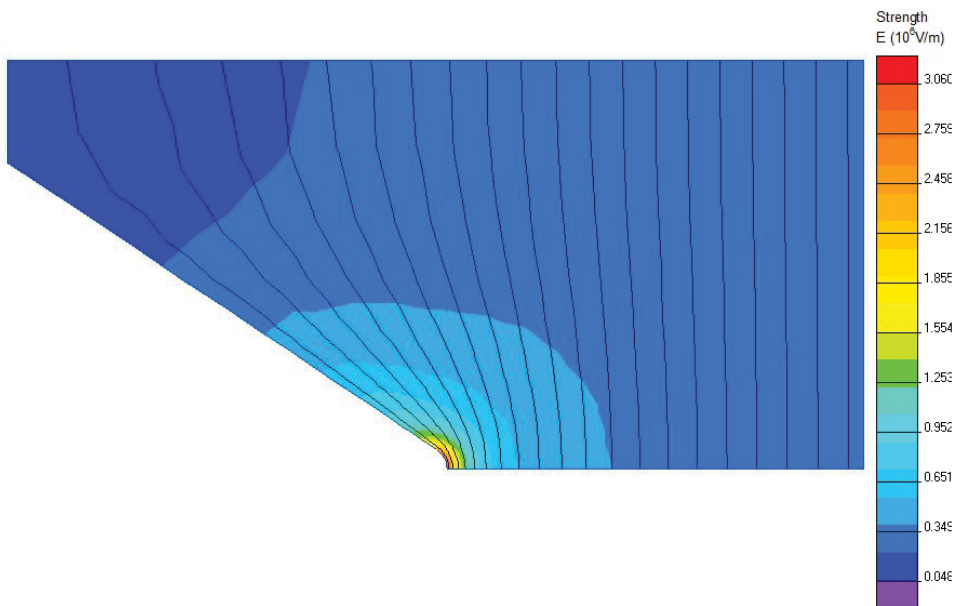


Figure E.7: Electric field results from QuickField with an applied voltage of 1000 V applied between ILFF (lower left geometry) and extraction electrode (right boundary). Geometry from Run 5 at 2350 V.

Appendix F

Letters of Permission

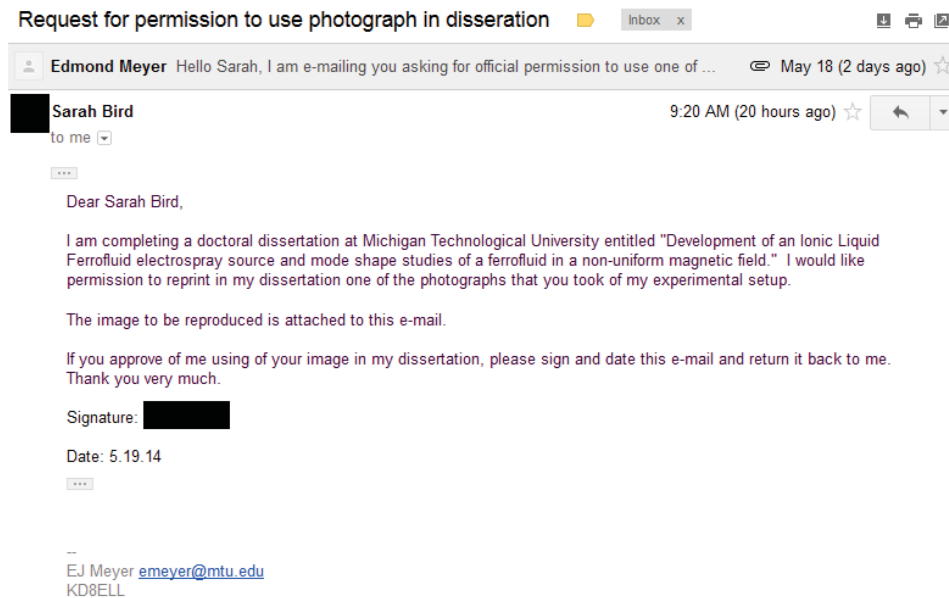


Figure F.1: Letter of permission to use Figure 4.3 in this dissertation. Signature redacted.